



THE UNIVERSITY OF ARIZONA

University Libraries

UA CAMPUS
REPOSITORY

Folded Fisheye Lens Design for Compact 360-Degree Virtual Reality Camera

Item Type	text; Electronic Thesis
Authors	Felli, Alex
Publisher	The University of Arizona.
Rights	Copyright © is held by the author. Digital access to this material is made possible by the University Libraries, University of Arizona. Further transmission, reproduction or presentation (such as public display or performance) of protected items is prohibited except with permission of the author.
Download date	28/12/2021 15:45:53
Link to Item	http://hdl.handle.net/10150/628154

**FOLDED FISHEYE LENS DESIGN FOR COMPACT 360-DEGREE VIRTUAL
REALITY CAMERA**

by

Alexander Felli

Copyright © Alexander Felli 2018

A Thesis Submitted to the Faculty of the

COLLEGE OF OPTICAL SCIENCES

In Partial Fulfillment of the Requirements

For the Degree of

MASTER OF SCIENCE

In the Graduate College

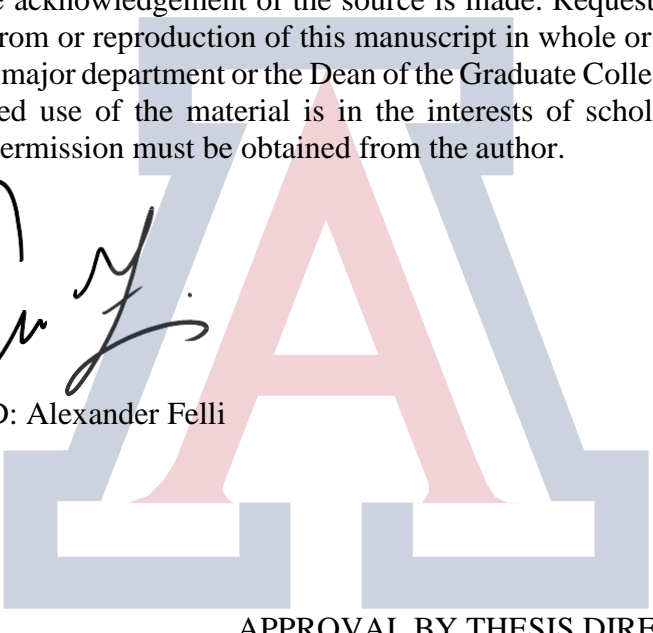
THE UNIVERSITY OF ARIZONA

2018

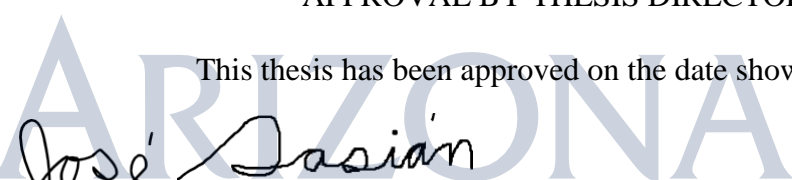
STATEMENT BY AUTHOR

The thesis titled Folded Fisheye Lens Design for Compact 360-Degree Virtual Reality Camera prepared by Alexander Felli has been submitted in partial fulfillment of requirements for a master's degree at the University of Arizona and is deposited in the University Library to be made available to borrowers under rules of the Library.

Brief quotations from this thesis are allowable without special permission, provided that an accurate acknowledgement of the source is made. Requests for permission for extended quotation from or reproduction of this manuscript in whole or in part may be granted by the head of the major department or the Dean of the Graduate College when in his or her judgment the proposed use of the material is in the interests of scholarship. In all other instances, however, permission must be obtained from the author.

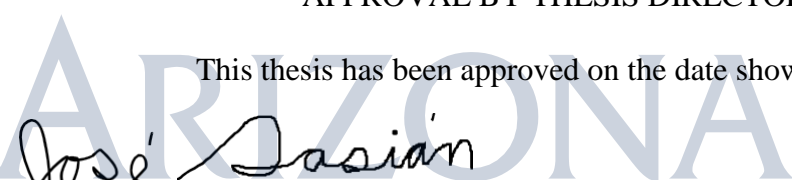


SIGNED: Alexander Felli



APPROVAL BY THESIS DIRECTOR

This thesis has been approved on the date shown below:



Jose M. Sasian
Professor of Optical Sciences

05/07/2018
Date

ACKNOWLEDGEMENTS

I would like to first thank my family for their support, encouragement, and guidance throughout my life. I am incredibly grateful to my adviser, Dr. Jose Sasian, for his support, mentorship, and willingness to share throughout my time at the College of Optical Sciences. In addition, I would like to acknowledge the members of my committee, Dr. Tom Milster and Dr. John Koshel, for taking the time to review my thesis while providing incredibly valuable suggestions.

Finally, I would like to thank Zemax and Photon Engineering for giving me the opportunity to pursue my passion of lens design by giving me permission to utilize their software for the design and evaluation of optical systems in this project.

DEDICATION

To my grandmother, Barbara, who introduced me to the wonders of science at a young age.

TABLE OF CONTENTS

LIST OF FIGURES	7
LIST OF TABLES	15
ABSTRACT.....	16
1 INTRODUCTION.....	17
1.1 Fisheye Lens History	18
1.1.2 Photographic Fisheye Lenses.....	23
1.1.3 Fisheye Lenses in Modern Consumer Electronics.....	25
1.2 Virtual Reality Camera Background.....	26
1.3 Thesis Content	31
2 FISHEYE LENS PROPERTIES	33
2.1 Reverse Telephoto Properties	33
2.2 Fisheye Lens Structure.....	34
2.3 Distortion Properties	36
2.4 Entrance Pupil Properties.....	40
2.5 Relative Illumination	44
2.6 Depth of Field and Hyperfocal Distance	45
2.7 Diagonal versus Circular Fisheye Lenses	47
3 OPTICAL DESIGN REQUIREMENTS	50
3.1 Package Dimensions and First-Order Requirements	51
3.2 ON-Semiconductor AR0237 CMOS Image Sensor Considerations	52
3.2.1. Sensor Package Dimensions and Back Focal Length Requirements.....	53
3.2.2 Image Circle Diameter.....	55
3.2.3 Chief Ray Angle	56
3.4 MTF Requirement.....	57
3.5 Lateral Color Aberration Requirement	60
3.6 Relative Illumination	62
3.7 Wavelength Weighting Definition.....	63
3.8 Manufacturability and Cost.....	67
3.9 Optical Design Requirement Summary	68
4 COMPACT FOLDED FISHEYE LENS DESIGN.....	69
4.1 Prior Art and Starting Point Design	69
4.2 Prism Considerations	72
4.3 Glass Material Choices	74
4.4 Optical Design	77
4.4.1 Optical Prescription Data.....	80

4.5 Design Evaluation.....	81
4.5.1 Tolerance Analysis.....	90
4.5.2 Total Internal Reflection Evaluation.....	96
4.5.3 Entrance Pupil Position versus Image Height.....	97
4.5.4 Optical Performance versus Requirements Summary	99
4.5 Multi-Camera Configuration and Stitch Location	101
5 STRAY LIGHT ANALYSIS OF FOLDED FISHEYE LENS	103
5.1 Stray Light in Cameras	104
5.2 Reflectance and Coating Assumptions	108
5.3 Ghost Analysis Process in FRED	113
5.3.1 Coating and Raytrace Control Settings.....	115
5.3.2 Optical Source Configuration	117
5.3.3 Ghost Image and Ray Path History Analysis Process	123
5.4 Initial Ghost Analysis (Color Image Plots).....	129
5.4.1 Color image plots from 0 degrees to 100 degrees.....	130
5.4.2 Prominent ray path ghost analysis	131
5.5 Selecting UV/IR-cut Surface	139
5.5.1 Contributing surfaces	140
5.5.2 Ghost comparison between UV/IR-cut located on surfaces L7R2, L4R1, and L6R2	141
5.5 Final Ghost Performance of Folded Fisheye Lens.....	144
6 CONCLUSION	148
REFERENCES.....	150

LIST OF FIGURES

Figure 1.1. R.W. Wood's Fisheye Lens Schematic, showing light entering a glass plate which is attached to a tank of water, where the rays end at a photographic plate. [1]	18
Figure 1.2. A photograph taken by R.W. Wood's fisheye camera to simulate what a fish would see inside of an aquarium [1]	19
Figure 1.3. Fisheye Camera designed by W. N. Bond [3]	19
Figure 1.4. Photograph of the sky captured with W. N. Bond's fisheye camera [3]	20
Figure 1.5. Hill Sky Lens [2]	21
Figure 1.6. Four different kinds of cloud formations captured with the Hill Sky Lens [2]	21
Figure 1.7. Comparison between AEG Fisheye lens and Nikkor Fisheye Lens [4]	22
Figure 1.8. Lens schematic of Miyamoto's Nikkor 8mm F/8 fisheye lens design [10]	23
Figure 1.9. Lens schematic of Nikkor 6mm F/2.8 fisheye lens design [11]	24
Figure 1.10. Lens schematic of Canon 8-15mm F/4 fisheye zoom lens [12]	24
Figure 1.11. Modern consumer devices which use fisheye or wide-angle lenses. (a) GoPro action camera [13], (b) Automotive backup camera [14], (c) Ring doorbell camera [15], (d) Garmin Virb 360-degree VR Camera [16].....	25
Figure 1.12. (a) GoPro Fusion 360-degree camera, (b) photosphere image with two perspective view regions highlighted, (c) 2D punchout perspective view #1 (d) 2D punchout perspective view #2 [5]	26
Figure 1.13. Google Maps street car with multi-camera 360-degree camera	27
Figure 1.14. (a) Facebook Surround 360 16-camera system, 24-camera system, and 6-camera systems [18], (b) Internal components of the 16-camera Facebook Surround 360 system, (c) GoPro Oydssey 16-camera system [6], (d) GoPro Omni 6-camera system [19]	28
Figure 1.15. (a) GoPro Fusion camera [5], (b) Samsung Gear 360 [20], (c) Garmin Virb [16], (d) Nikon KeyMission 360 [21], (e) Ricoh Theta V [22].....	29
Figure 1.16. (a) GoPro Fusion schematic showing side-by-side lens placement [5], (b) Ricoh Theta lens schematic showing folded optical path via two glass prisms [22]	29
Figure 2.1. Lens structure differences between (a) Telephoto Lens and (b) Reverse Telephoto Lens with Equal Effective Focal Lengths	34
Figure 2.2. Nikkor 6mm F/2.8 220-degree fisheye lens structure showing 3 negative meniscus lenses in front of the assembly [11]	35

Figure 2.3. Demonstrating image compression at edge of field for (a) Orthogonal Distortion and (b) Equisolid Distortion	38
Figure 2.4. Different distortion profile images for the same object, demonstrating (a) stereographic distortion, (b) equidistant distortion, (c) equisolid distortion, and (d) orthographic distortion.	39
Figure 2.5. Image height versus field of view plots for each of the fisheye distortion profiles ...	40
Figure 2.6. Entrance pupil walk in the Nikkor 8mm F/8 fisheye lens [8]	41
Figure 2.7. Off-axis coma aberration seen in the entrance pupil of a fisheye lens.....	42
Figure 2.8. Off-axis entrance pupil aberration seen in a compact fisheye lens from 0° to 90°	42
Figure 2.9. (a) Fisheye lens before ray aiming is turned on. (b) Fisheye lens with ray aiming turned on [4].....	43
Figure 2.10. A 210-degree field of view fisheye lens exhibiting the Slyusarev effect, where the illumination is greater at the edge of the field of view than in the center field [30].....	45
Figure 2.11. Depth of Field and Hyperfocal Distance schematic [32]	46
Figure 2.12. Diagonal Fisheye Lens versus Circular Fisheye Lens.....	48
Figure 2.13. (a) Circular fisheye image versus (b) diagonal fisheye image	49
Figure 3.1. Package requirements for the folded fisheye lens, with thickness-to-thickness requirement illustrated in red, and package width requirement illustrated in blue.....	51
Figure 3.2. ON-Semiconductor AR0237 Key Parameters and RGGB Bayer format [23]	53
Figure 3.3. ON-Semiconductor AR0237 CMOS Sensor package dimensions.....	54
Figure 3.4. Image circle diameter set to be 3.164mm for the folded fisheye lens [23]	55
Figure 3.5. Pixel structure for common CMOS sensors [4]	56
Figure 3.6. Modulation Transfer Function (MTF) [35]	57
Figure 3.7. Modulation Transfer Function example [34]	58
Figure 3.8. Demonstrating the contrast and image quality reduction from MTF between (a) a lens with high MTF and (b) a lens with lower MTF [36]	58
Figure 3.9. MTF plot and photo representation of phase reversal [34][35]	59
Figure 3.10 Illustration of lateral chromatic aberration of the Chief Ray for F (486nm), d (587nm), and C (565nm) wavelengths.....	60
Figure 3.11. Lateral Color shift must be greater than two pixels to be detectable in the RGGB Bayer array format used in the AR0237 CMOS sensor.....	61

Figure 3.12. Quantum Efficiency of the ON-Semiconductor AR0237 CMOS image sensor	63
Figure 3.13. Transmission versus wavelength plots for (a) UV-Cut Filter and (b) IR-Cut Filter [28]	64
Figure 3.14. Optical spectra which the folded fisheye lens must operate with, including the quantum efficiency of the AR0237 sensor, Photopic eye test spectrum, and UV/IR filter	65
Figure 3.15. (a) All optical spectra that the lens will be used with, along with a weighted average and the wavelength weighting used in Zemax, (b) Wavelength weighting values and (c) plot of wavelength weighting values used in the design of the folded fisheye lens.....	66
Figure 3.16. Mounting flanges on various lens element shapes to aid in assembly [25]	67
Figure 4.1. Schematic of two U.S. patents for compact folded zoom lenses. The systems are shown ‘unfolded’ with the prism represented as a thick plane parallel element [39].....	70
Figure 4.2. Lens schematic and performance of patent US 7,023,628 [40]	70
Figure 4.3. Optical prescription of patent US 7,023,628 [40]	71
Figure 4.4. Ohara low softening temperature optical glass types intended for PGM [42]	74
Figure 4.5. 2D Layout of Compact Folded Fisheye Lens Design	77
Figure 4.6. 3D Layout of Compact Two-Lens System Using Folded Fisheye Lens Design.....	77
Figure 4.7. (a) Illustration of element size affecting mounting process and procedure [25], (b) Element size chosen for easy loading procedure in manufacturing the folded fisheye lens....	79
Figure 4.8. OPD for field heights ranging from 0 degrees to 95 degree half field of views, showing a maximum scale of +/- 2 waves	81
Figure 4.9. RMS Wavefront Error versus Field. Maximum RMS wavefront error is 0.18 waves at 450nm.....	82
Figure 4.10. Field Curvature, Astigmatism, and fθ Distortion of Folded Fisheye Lens	82
Figure 4.11. Wavefront coefficient aberration summary, showing lots of field curvature, astigmatism, and distortion left in the final image.....	83
Figure 4.12. Half Field of View versus Image Height plot demonstrating the distortion profile in the folded fisheye lens compared to traditional fisheye distortion profiles with a focal length of 1.3mm	83
Figure 4.13 Chromatic Focal Shift versus Wavelength shows that the folded fisheye lens is apochromatic with zero chromatic focal shift between 408nm, 450nm and 588nm, with a maximum shift range of 3.011 um	84

Figure 4.14 Lateral Chromatic Aberration Wavelength showing maximum lateral color shift of 1.496um.....	85
Figure 4.15 Spot Diagram for half fields of view of (a) 0 degrees, (b) 30 degrees, (c) 60 degrees, (d) 90 degrees, and (e) 92.5 degrees	85
Figure 4.16 Polychromatic Point Spread Functions for half fields of view of (a) 0 degrees, (b) 30 degrees, (c) 60 degrees, (d) 90 degrees (e) 92.5 degrees and (f) 95 degrees	86
Figure 4.17. Polychromatic MTF versus spatial frequency up to 167lp/mm for field heights ranging from 0 degrees to 95 degrees. Minimum design MTF is 48%.....	87
Figure 4.18. Polychromatic MTF versus spatial frequency up to 600lp/mm for all field heights, demonstrating greater than 30% MTF up until 240lp/mm.....	87
Figure 4.19 Relative Illumination plot, showing minimum R.I. equal to 83.3%.....	88
Figure 4.20 Chief ray angle versus image height, with a maximum CRA of 11.44 degrees.....	89
Figure 4.21. Standard Manufacturing Tolerances [30].....	90
Figure 4.22. Monte Carlo Tolerance analysis settings used in Zemax	92
Figure 4.23. Monte Carlo Tolerance Analysis results from 1000 trials.....	93
Figure 4.24. Minimum MTF Distribution at 167lp/mm, showing a 94% yield with the tolerances listed in Table 4.6.....	93
Figure 4.25. Worst offenders list from the Monte Carlo sensitivity analysis with 1000 trials....	94
Figure 4.26. 2D Layout of folded fisheye lens highlighting the three most sensitive surfaces to tolerance perturbations in the optical design.....	94
Figure 4.27. MTF distribution over 20 Monte Carlo trails, showing an estimated 90% yield	95
Figure 4.28. Incident angle versus half field of view on the prism's reflecting interface, demonstrating 100% TIR for all field angles in the folded fisheye lens design	96
Figure 4.29 Entrance pupil shift visualized for the folded fisheye lens design at 30-degree, 60-degree, and 95-degree field heights.	97
Figure 4.30. Measured entrance pupil position versus field of view in the folded fisheye lens... ..	98
Figure 4.31. 3D Layout of the compact folded fisheye lens design.	100
Figure 4.32. (a) Two folded fisheye lenses shown each capturing hyper-hemispherical images when separated. (b) Two folded fisheye lenses capturing a full 360-degree photosphere when both systems are placed back-to-back at the prism's reflecting interface.....	101

Figure 4.33. 2D Schematic of the folded fisheye lens showing the 95-degree field crossing the optical axis at a distance of 135mm from the vertex of the first lens.	102
Figure 4.34. 3D Schematic of the folded fisheye lens showing the two-lens system's ability to stitch/reconstruct any objects outside of a 270mm diameter sphere.	102
Figure 5.1. Ghost image locations formed by a thick lens [24]	104
Figure 5.2 Ghost ray paths in a doublet lens [24]	104
Figure 5.3. Contrast reduction due to stray light in an imaging system. (left) Photo with stray light. (right) Photo without stray light [24].....	105
Figure 5.4. Ghost images and pedal flares seen in a digital GoPro camera. Taken in a dark room with a bright flashlight directed at the camera.	106
Figure 5.5. (a) Person using a VR Camera in a canyon while paragliding, (b) Demonstrating the photosphere image capture on the GoPro Fusion VR Camera, (c) Stray light effects observed when the sun is only in the field of view of one lenses [5]	107
Figure 5.6. Reflectance of s-polarized $Rs(\theta 1)$, p-polarized $Rp(\theta 1)$, and randomly polarized $R(\theta 1)$ light as a function of incident angle on an optical surface.....	109
Figure 5.7. Standard antireflection coatings for the visible wavelength region which are offered by Edmund Optics [26]	110
Figure 5.8. Reflectance versus Wavelength for the Vis0° antireflection coating [26]	111
Figure 5.9. Demonstration of ultraviolet long-pass filter and infrared short-pass filter being combined into one band-pass filter [28].....	112
Figure 5.10. Transmission vs wavelength plots for (a) UV-Cut Filter and (b) IR-cut Filter.....	112
Figure 5.11. Ray splitting at an optical surface	113
Figure 5.12. Defining the aperture stop in FRED to have an outer diameter of 10mm.....	114
Figure 5.13. Simple Coating definition in FRED for the antireflection coating which has 0.4% reflection and 99.6% transmission	116
Figure 5.14. Simple blackbody solar spectrum definition in FRED.....	117
Figure 5.15. Optical Source Settings example for 60 degree field	118
Figure 5.16. Entrance Pupil Position vs Image Height (a) plot and (b) visualization	120
Figure 5.17. Manual ray aiming via the location/orientation tab in optical source settings	120
Figure 5.18. Color Image Plot of 30-degree field as a function of the numbers of rays traced. (a) 500,000 rays traced (b) 5,000,000 rays traced	121

Figure 5.19. Analysis surface sampling frequency differences. (a) 51 x 51 sampling (b) 201 x 201 sampling	122
Figure 5.20. Analysis Surface Settings showing a sampling division of 201 x 201	123
Figure 5.21. Stray light simulation for a 30-degree field in a folded fisheye lens.....	124
Figure 5.22. Color image plot simulation for 30-degree field in the folded fisheye lens	124
Figure 5.23. Irradiance Spread Analysis for 30-degree field in the folded fisheye lens. (a) Irradiance plot before log scale is applied (b) Settings used to scale the plot (c) Irradiance plot after log scale is applied with a floor set to -9	125
Figure 5.24. Stray Light Report showing only ghosts present on the image plane, sorted by total power contained in each ray path.....	126
Figure 5.25. Analysis Surface defined to only include rays on path 505	127
Figure 5.26. (a) Full color image plot for all rays, (b) Color image plot which only includes ray path 505, (c) Irradiance plot which only includes ray path 505	127
Figure 5.27. 3D view of ray path 505. This shows that the football shaped ghost comes from reflections off of the sensor cover glass and the prism.	128
Figure 5.28. Ghost image color image plots for the folded fisheye lens before the highly reflective UV/IR-cut filter location is introduced to the optical assembly	130
Figure 5.29. Ghost Images #1 through #10 in (a) 30-degree field and (b) 80-degree field.....	131
Figure 5.30. Ghost #1. (left) 3D Layout of ghost path, which originates from reflections off the sensor cover glass, (middle) color image plot, (right) irradiance spread	132
Figure 5.31. Ghost #2. (left) 3D Layout of ghost path, which originates from reflections off the sensor cover glass and L8R2, (middle) color image plot, (right) irradiance spread	132
Figure 5.32. Ghost #3. (left) 3D Layout of ghost path, which originates from reflections off L3R2 and Prism R2, (middle) color image plot, (right) irradiance spread	133
Figure 5.33. Ghost #4. (left) 3D Layout of ghost path, which originates from reflections off the sensor cover glass and Prism R2, (middle) color image plot, (right) irradiance spread	134
Figure 5.34. Ghost #5. (left) 3D Layout of ghost path, which originates from reflections off the sensor cover glass and L3R2, (middle) color image plot, (right) irradiance spread	134
Figure 5.35. Ghost #6. (left) 3D Layout of ghost path, which originates from reflections off the sensor cover glass and L5R2, (middle) color image plot, (right) irradiance spread	134

Figure 5.36. Ghost #1 (80-degree field). (left) 3D Layout of ghost path, which originates from reflections off the sensor cover glass, (middle) color image, (right) irradiance	135
Figure 5.37. Ghost #2 (80-degree field). (left) 3D Layout of ghost path, which originates from the sensor cover glass and L8R2, (middle) color image, (right) irradiance	135
Figure 5.38. Ghost #7. (left) 3D Layout of ghost path, which originates from reflections off L6R1 and L5R2, (middle) color image plot, (right) irradiance spread	136
Figure 5.39. Ghost #8. (left) 3D Layout of ghost path, which originates from reflections off Prism R2 and Prism R1, (middle) color image plot, (right) irradiance spread	136
Figure 5.40. Ghost #9. (left) 3D Layout of ghost path, which originates from reflections off L2R1 and Prism R2, (middle) color image plot, (right) irradiance spread	136
Figure 5.41. Ghost #10. (left) 3D Layout of ghost path, which originates from reflections off Prism R1 and L1R2, (middle) color image plot, (right) irradiance spread	137
Figure 5.42. 2D Layout of the Folded Fisheye Lens design with notes on which surfaces contribute to the ghosts with highest irradiance.....	137
Figure 5.43. Example of a broadband-pass filter's transmission range shifting towards shorter wavelengths as the incident angle on the multilayer filter increases [27].....	139
Figure 5.44. 2D Layout of the Folded Fisheye Lens design with notes on which surfaces contribute to the ghosts with highest irradiance.....	140
Figure 5.45. Ghost Images with no UV/IR-cut placed in the imaging system for (a) 30 degrees field, (b) 60 degrees field, and (c) 95 degrees field.	142
Figure 5.46. Ghost Images for UV/IR-cut placed on L7R2 for (a) 30 degrees field, (b) 60 degrees field, and (c) 95 degrees field.....	142
Figure 5.47. Ghost Images for UV/IR-cut placed on L4R1 for (a) 30 degrees field, (b) 60 degrees field, and (c) 95 degrees field.....	142
Figure 5.48. Ghost Images for UV/IR-cut placed on L6R2 for (a) 30 degrees field, (b) 60 degrees field, and (c) 95 degrees field.....	142
Figure 5.49. Ghost UV/IR #1. (left) 3D Layout of ghost path, which originates from the sensor cover glass and L6R2, (middle) color image plot, (right) irradiance spread	143
Figure 5.50. Ghost UV/IR #2. (left) 3D Layout of ghost path, which originates from L6R2 and Prism R2, (middle) color image plot, (right) irradiance spread	143
Figure 5.51. Demonstrating UV/IR-cut location on L6R2 in 3D view of folded fisheye lens ...	144

Figure 5.52. Ghost image color image plots for the folded fisheye lens with the highly reflective UV/IR-cut filter placed on lens 6 surface 2	145
Figure 5.53. Ghost image color plots for (a) 30-degree field and (b) 80-degree field.....	146
Figure 5.54. Ghost image plots superimposed on a real circular fisheye image. (a) 0-degree field (b) 30-degree field, (c) 60-degree field, (d) 90-degree field	147

LIST OF TABLES

Table 1.1 Center thickness, height, and width dimensions of common virtual reality cameras...	30
Table 3.1. First-Order Specifications for Folded Fisheye Lens.....	68
Table 3.2. Optical Performance Requirements for Folded Fisheye Lens	68
Table 4.1. Critical Angle versus Prism Index	73
Table 4.2. Ohara L-LAH86 glass properties [41]	74
Table 4.3. Glass types used in the folded fisheye lens design	76
Table 4.4. Optical Prescription for 1.3mm F/2.8 Compact Folded Fisheye Lens	80
Table 4.5 Center thickness, height, and width dimensions of common virtual reality cameras.	
The Folded Fisheye lens' package size is just slightly larger than the Ricoh Theta.....	89
Table 4.6. Tolerances used in the Monte Carlo analysis of the folded fisheye lens design	91
Table 4.7. Optical Performance Requirements for Folded Fisheye Lens	99
Table 5.1 Entrance pupil location as a function of image height for the folded fisheye lens....	119
Table 5.2. Optical coating property assumptions used in generating the color image ghost analysis plots shown in Fig. 5.28	129
Table 5.3. Summary of Ghost irradiance and contributing surfaces for the top 10 brightest ghosts in the folded fisheye lens before the UV/IR-cut filter is placed in the system	138
Table 5.4. Summary of ghost irradiance and contributing surfaces for the top 12 brightest ghosts when the UV/IR-cut filter is placed on L6R2 in the folded fisheye lens	146

ABSTRACT

The consumer electronic industry has continued to drive modern camera design to be as small and compact as possible, as is seen with the rise of very thin smartphone cameras, compact action cameras, and wearable technologies. As sensor technology continues to develop, and consumers prefer more minimal form factors, modern imaging modules are continuously being pushed to be short in length, while maintaining sharp image quality at a low cost. With this, consumers have begun to develop interests in immersive digital content, which has given rise to the popularity of action cameras and virtual reality capture devices, generating high-demand for high performance compact fisheye lens modules. Many virtual reality cameras which are being developed today utilize two fisheye lens imaging modules to create two hemispherical images, which are stitched together to create a full 360-degree photosphere. The end-user can pan around and view any location in this photosphere, creating a unique scenario where the optical performance at the edge of the field-of-view is just as important in the center of the image.

This thesis explores the unique requirements and properties of fisheye lenses used in these systems, and a new folded fisheye lens is designed with the intent to be used in a compact virtual reality 360-degree camera. The optical system designed is an f/2.8 fisheye lens meant to be used with a 1/2.7" CMOS image sensor, which has a focal length of 1.297mm and a full-field of view of 190 degrees. This lens design utilizes a powered prism to fold the optical path after the first lens element to maintain a compact form-factor and minimize the center thickness of the imaging system when the two fisheye lens modules are placed back-to-back. The optical quality, stray-light and ghost performance, and manufacturability of the compact folded fisheye lens design are analyzed and discussed in detail.

1 INTRODUCTION

Fisheye lens designs have been utilized for more than a century, with the first designs being used for scientific meteorological purposes. In 1906, R. W. Wood created the first fisheye lens [1] by placing photosensitive film in a tank of water which had been turned into a pinhole camera; shortly after in 1924, the Hill Sky lens was designed as an all-glass solution to capturing a hemispherical field of view in an image [2]. While the first fisheye lenses were primarily used for the surveying of cloud formations, the unique distortion appearance had quickly piqued the interest of lens designers and photographers, and the first Nikkor fisheye lens for use in a 35mm camera was designed in 1964 [4]. Photographic fisheye lenses have continued being developed since then, and modern fisheye lenses are very compact while capable of capturing very sharp polychromatic images at F-numbers as low as F/2.8.

An interesting area of current fisheye lens development is virtual reality camera design, which uses two fisheye lenses to capture a full 360-degree image commonly referred to as a photosphere. Previously, the multi-camera systems used to capture these images were made up of as many as 16 cameras [6], where the field of view of each camera is designed to overlap such that the images obtained can be stitched together into one photosphere.

As these devices have continued to develop and become more compact, consumer virtual reality cameras now use only two circular fisheye lenses, faced opposite of each other, where each lens has a field of view greater than 180 degrees. Each lens is paired with an image sensor, and the two hemispherical images are stitched into one final photosphere. As this technology progresses, consumers continue to prefer more compact camera designs. This push for high-performing fisheye lenses with a preference for compact form factors has motivated the author to design a folded fisheye lens for use in a compact virtual reality 360-degree camera.

1.1 Fisheye Lens History

Fisheye lenses have a history going back more than 100 years, starting with the first fisheye pinhole camera developed by R.W. Wood in 1906 in a paper titled “Fish-Eye Views, and Vision Under Water.” [1]. R.W. Wood’s fisheye camera works via Snell’s Law, where a photographic film plate is submerged in a glass tank full of water with an aperture stop placed at the glass-water interface. The glass which makes up the water tank provides the initial refraction, and the water inside of the tank prevents the light from experiencing total internal reflection in the glass. A 96-degree viewing angle from the film plane will emerge in air as a full hemisphere due to Snell’s Law [1], which allows for a full 180-degree image to be captured on the film [Fig 1.1]. He recorded images with this camera to simulate what visitors at an aquarium might look like to a fish inside of a tank of water [Fig 1.2], and to capture other hemispherical images.

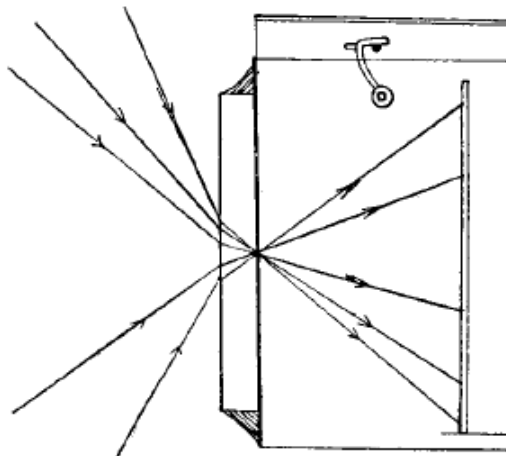


Figure 1.1. R.W. Wood’s Fisheye Lens Schematic, showing light entering a glass plate which is attached to a tank of water, where the rays end at a photographic plate. [1]



Figure 1.2. A photograph taken by R.W. Wood's fisheye camera to simulate what a fish would see inside of an aquarium [1]

In 1922, an all-glass solution was designed by W.N. Bond for the use of meteorological cloud recording. This design utilized a glass hemisphere placed behind a plane parallel plate, with the aperture stop located at the center of curvature of the hemispherical lens [3]. While this design is less cumbersome to transport and utilize compared to R. Wood's water tank, W. N. Bond's fisheye lens created a spherical image plane which required very large F-numbers to ensure focus was maintained on the photographic plate. This made the system very slow, with a maximum F-number of F/50 [Fig 1.3]. In addition, the system suffered from large amounts of chromatic aberration and thus required the use of monochromatic filters in this lens.

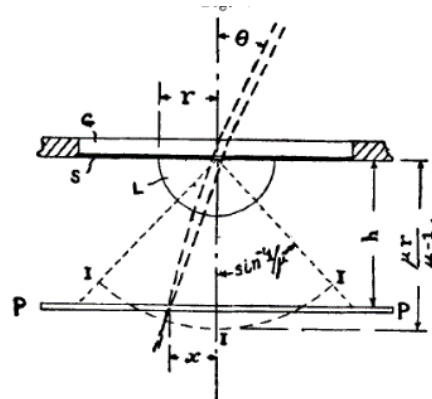


Figure 1.3. Fisheye Camera designed by W. N. Bond [3]

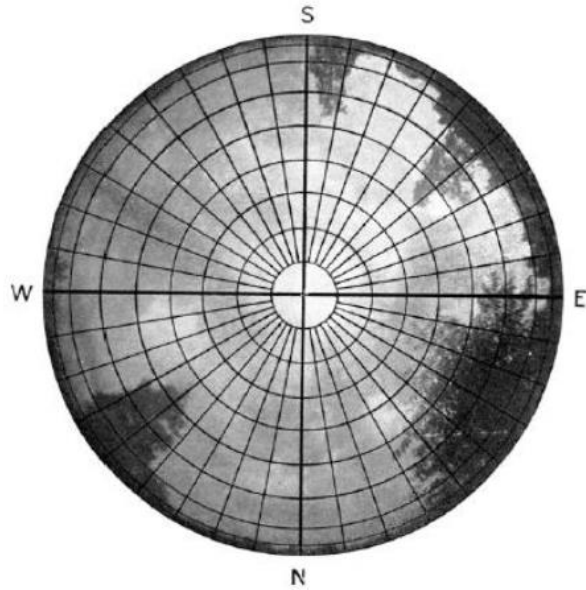


Figure 1.4. Photograph of the sky captured with W. N. Bond's fisheye camera [3]

Shortly after W. N. Bond's all-glass solution, the fisheye lens design was improved upon in 1924 by Robin Hill whom had increased the relative illumination and was able to lower the F-number down to F/22. Hill accomplished this by utilizing a negative meniscus lens instead of a plane parallel plate, while also changing the aperture stop location [2]. In addition, the plano-convex lens behind the stop is split into two lenses for aberration control to minimize coma, astigmatism, and field curvature. The F-number of the lens is constrained by the spherical aberration left in the system. The Hill Sky Lens [Fig 1.5] was the first commercially sold fisheye lens, manufactured by Beck of London [7] and was primarily used to produce detailed images for cloud photography and sky surveying applications [Fig 1.6]. Most fisheye lenses today have similar constructions to the Hill Sky Lens with a negative meniscus front group before the aperture stop and a positive group behind the stop, while utilizing many more lens elements to control aberrations and increase the speed of the imaging system [8].

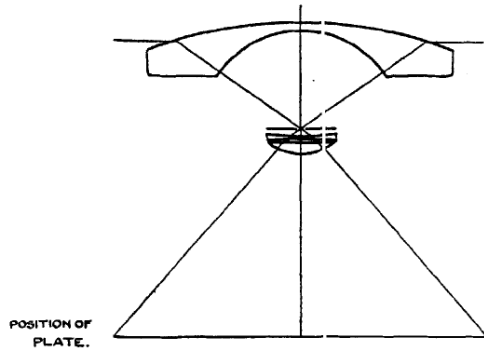


Figure 1.5. Hill Sky Lens [2]

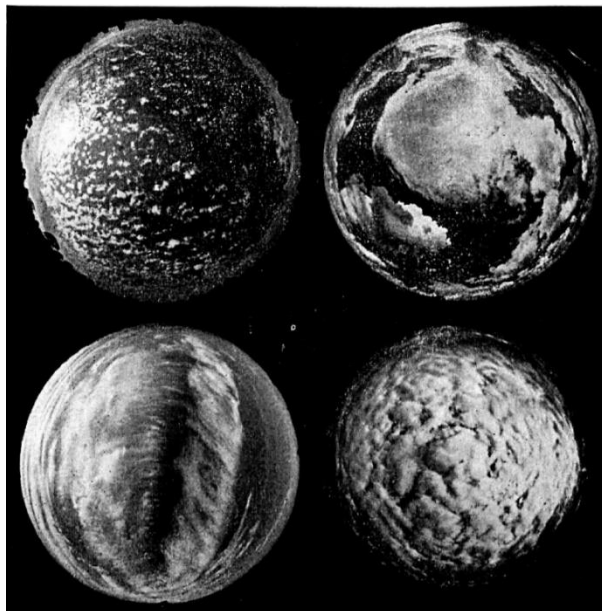


Figure 1.6. Four different kinds of cloud formations captured with the Hill Sky Lens [2]

While the Hill Sky lens significantly improved the optical performance of the fisheye lens from W. N. Bond's design, it still suffered from significant amounts of spherical aberration and chromatic aberration. Because of this, the F-number had to be very large, and only monochromatic images could be taken. In 1932, the Allgemeine Elektricitäts-Gesellschaft (AEG) Company in Berlin filed patents for a new fisheye lens which significantly improved upon the optical performance compared to the Hill Sky Lens [9]. This system utilizes two negative meniscus lenses in the front of the stop, compared to Hill's single meniscus lens, and places a doublet lens behind

the stop to improve the chromatic aberration. By utilizing five lens elements in four groups, the 17mm focal length AEG fisheye lens could achieve a full field of view of 210 degrees while maintaining good image quality at F-numbers as low as F/6.3. The increased speed allowed for much shorter exposure times than previous fisheye lens designs, opening the possibility for more practical fisheye photography.

Not long after the AEG lens was patented, Nikon patented its first fisheye lens in 1938 to be used for meteorological observation which resembles a very similar structure to the AEG fisheye lens [4]; the Nikkor 16mm F/8 fisheye lens also uses two negative meniscus lenses in front of the stop, and a cemented doublet for chromatic aberration control after the aperture [Fig 1.7].

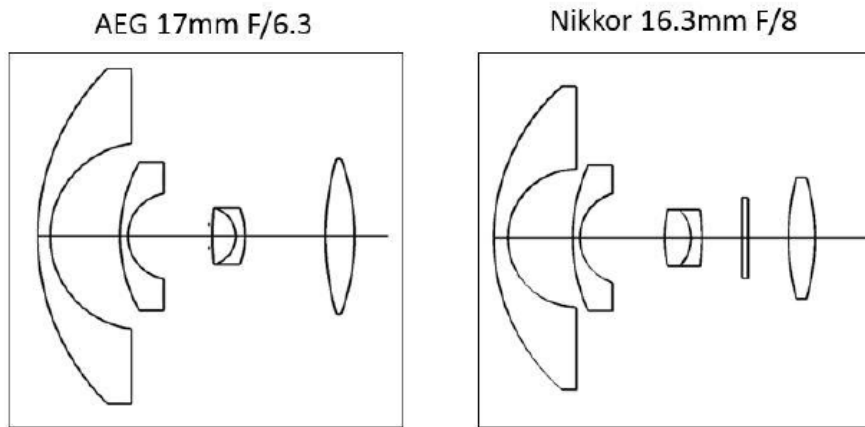


Figure 1.7. Comparison between AEG Fisheye lens and Nikkor Fisheye Lens [4]

Up until this point, fisheye lenses were primarily used for scientific applications, such as surveying clouds and the sky. However, fisheye lenses eventually became very popular in photography for the unique images and perspectives that they could capture and are still used in photography today.

1.1.2 Photographic Fisheye Lenses

In 1964 the first fisheye lens designed for 35mm film SLR cameras was designed by Kenro Miyamoto from Nagoya University while working for Nikkor [10]. The 8mm focal length fisheye lens had a maximum aperture of F/8, and was the first fisheye lens to correct the lateral color aberration by placing a negative achromatic doublet in front of the stop [Fig 1.8]. This fisheye lens pioneered the use of fisheye lenses for photography outside of scientific use.

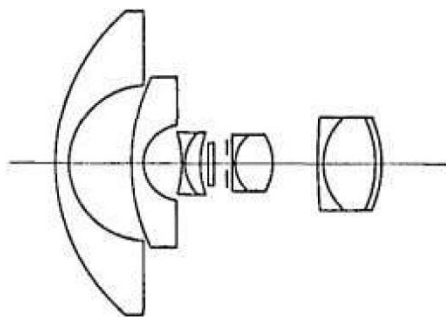


Figure 1.8. Lens schematic of Miyamoto's Nikkor 8mm F/8 fisheye lens design [10]

Nikon continued improving fisheye lens design for many years, and in 1972 had introduced an ultra-wide fisheye lens with a field of view of 220 degrees which could operate at a maximum aperture of F/2.8 [11]. This lens utilizes a similar structure to Miyamoto's design where the lateral color is controlled with a negative achromatic doublet before the stop with positive achromatic doublets after the stop. To increase the field of view to 220 degrees, a third negative meniscus lens is placed at the front of the lens assembly. This lens exemplifies how wide of an angle fisheye lenses can capture while still operating at fast apertures, which enabled photographers to capture images with these lenses on 35mm film with short exposure times.

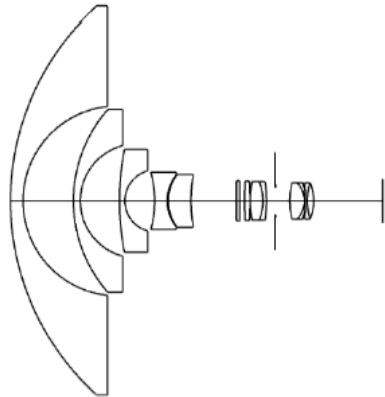


Figure 1.9. Lens schematic of Nikkor 6mm F/2.8 fisheye lens design [11]

Nikkor was a real pioneer in the development of photographic fisheye lenses from the 1960's until the popularity had decreased in the 1990's, and their last 35mm fisheye lens was developed in 1994. Other camera companies like Canon and Olympus have also developed fisheye lens designs including fisheye zoom lenses. One of Canon's more recent fisheye lens designs is a fisheye zoom lens from 2010 [12] with a focal length range from 8mm to 15mm, which operates at a maximum aperture of F/4. This zoom fisheye lens allows a photographer to capture a circular fisheye image at the 8mm focal length extreme and a wide-angle image at the 15mm focal length extreme which fills the diagonal of the sensor.

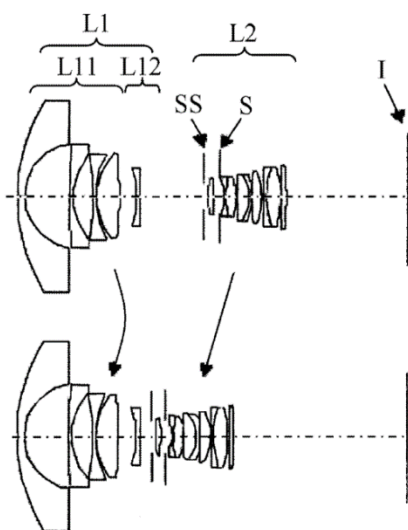


Figure 1.10. Lens schematic of Canon 8-15mm F/4 fisheye zoom lens [12]

1.1.3 Fisheye Lenses in Modern Consumer Electronics

More recently, there has been an increased popularity with action cameras that utilize wide-angle fisheye lenses in very compact camera form factors. The fisheye lenses used in these cameras commonly have very short total track lengths and use much smaller CMOS sensors on the order of 1/2-inch to 1/3-inch image formats. The immersive first-person video content which can be captured on compact action cameras like the GoPro has recently created a lot of excitement of fisheye lenses in consumers and photographers, and the camera industry has seen an increased demand for compact wide-angle imaging modules.

These compact fisheye lenses are also commonly used in surveillance cameras, automotive cameras, projection lenses in dome theatres, action cameras, virtual reality cameras, and even some cell phone cameras. Dash cameras and back up cameras are used in automotive vehicles to allow the driver to view different perspectives while being inside of the car, and surveillance cameras use fisheye lenses to capture the entire hemispherical field of view from the location which they are placed. The ability to capture hemispherical images in these compact form factors has recently led to the development of virtual reality cameras which utilize multiple fisheye lenses to capture a full 360-degree photosphere.

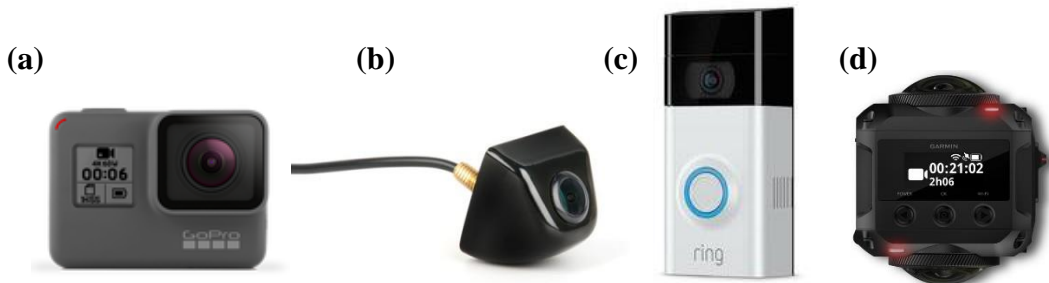


Figure 1.11. Modern consumer devices which use fisheye or wide-angle lenses. (a) GoPro action camera [13], (b) Automotive backup camera [14], (c) Ring doorbell camera [15], (d)

Garmin Virb 360-degree VR Camera [16]

1.2 Virtual Reality Camera Background

The development of high quality compact action cameras along with the development of virtual reality headsets like the Oculus Rift has led to the creation of compact virtual reality cameras which stitch together multiple images from many camera modules to reconstruct a full 360-degree photosphere. These spherical images and video are most commonly viewed with either virtual reality headsets where the user can move their head to look around and view any portion of the photosphere, or they will be viewed in a more traditional format on the computer or a cell phone where the user views a 2D punchout of the photosphere which can be panned around. Figure 1.12 demonstrates two different perspectives which could be viewed from the same photosphere using this punchout view method on the GoPro Fusion VR camera [5]. This unique method of viewing content creates a challenge for the lens designer of these systems, because the image quality at the edge of the field of view of each lens is equally important as in the center of the lens.

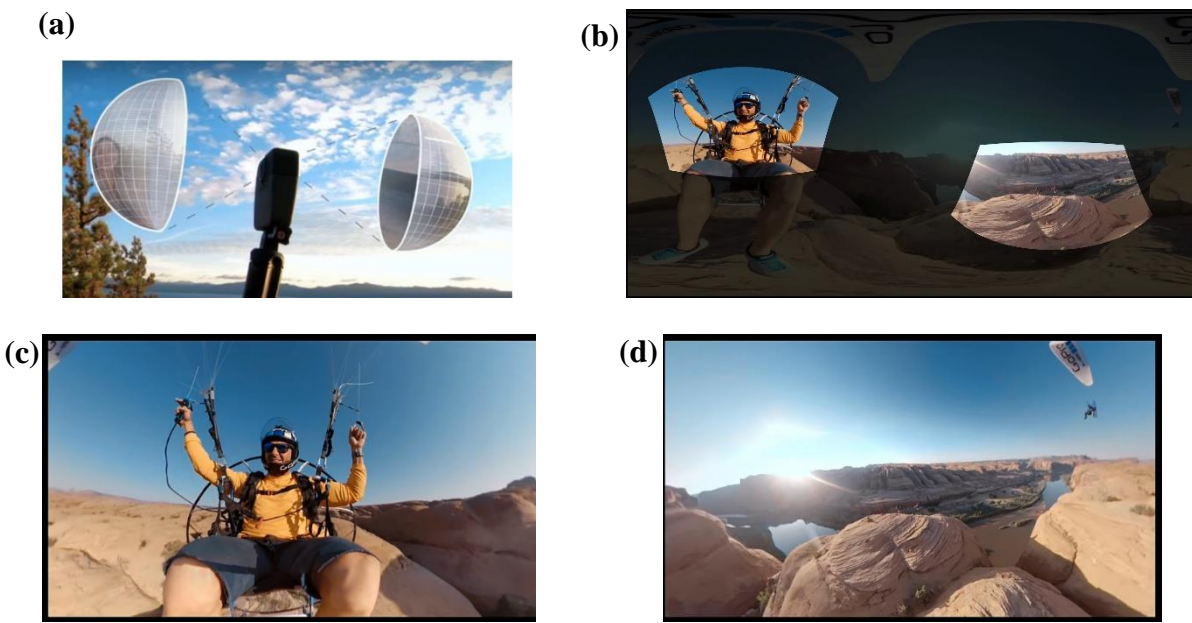


Figure 1.12. (a) GoPro Fusion 360-degree camera, (b) photosphere image with two perspective view regions highlighted, (c) 2D punchout perspective view #1 (d) 2D punchout perspective view #2 [5]

One of the more common applications where these multi-camera systems are used is the camera that Google Maps uses to capture street-view images [Fig 1.13]. The google maps camera uses 15 separate cameras to capture a full 360-degree field of view; to avoid gaps in the final photosphere adjacent cameras take slightly overlapping pictures, and then they stitch the photos together into a single 360-degree image [17]. In this scenario where there are many cameras being used, the field of view of each lens can be much smaller than the field of view of a fisheye lens, and other lens types may be used as long as the field of view of each camera overlaps to cover a full sphere.



Figure 1.13. Google Maps street car with multi-camera 360-degree camera [17]

Many of the first virtual reality camera systems that were introduced to the consumer market utilize many smaller camera modules similar to the Google Maps camera. Some of the more commonly used examples of these multi-camera virtual reality solutions include the GoPro Odyssey, GoPro Omni, and Facebook Surround 360 [Fig 1.14]. Facebook has three products in the Facebook Surround 360 series which can capture 360-degree images, including a 16-camera version, 24-camera version, and 6-camera version [18]. GoPro's first spherical cameras included two options, with the first being a 16-camera system targeted towards professionals and a 6-camera version which was targeted more towards consumers [19].

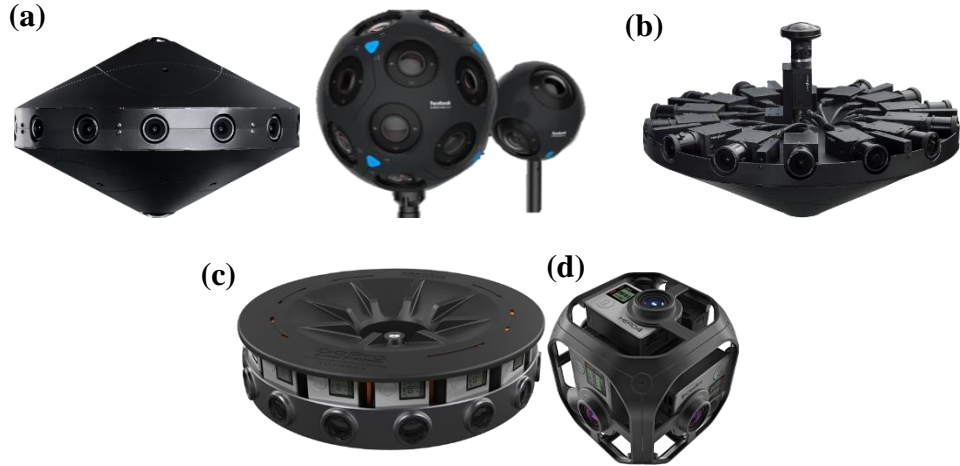


Figure 1.14. (a) Facebook Surround 360 16-camera system, 24-camera system, and 6-camera systems [18], (b) Internal components of the 16-camera Facebook Surround 360 system, (c) GoPro Odyssey 16-camera system [6], (d) GoPro Omni 6-camera system [19]

Because these systems utilize so many camera modules, they are able to capture incredibly high resolution; for example, the GoPro Odyssey can produce 8K stereoscopic spherical video at 30 frames per second. These products are great for professional film makers but are still far too large for general consumer use. This drove innovation towards creating much smaller virtual reality cameras, where most of these cameras can produce very high quality 360-degree photos and videos while being small enough to fit inside of a pocket. Almost all of these consumer-focused virtual reality cameras have begun to utilize only two compact circular fisheye lenses with greater than 180-degree fields of view which are paired with high resolution CMOS sensors; Similar to how the cameras in Fig 1.14 stitch together the images from many camera modules, these compact virtual reality cameras stitch together the images captured from the two lens and sensor modules to recreate high quality 360-degree photo and video. Five of the most common varieties of these consumer-focused virtual reality cameras are show in Fig 1.15. It should be noted that each of these cameras use only two fisheye lenses to capture full 360-degree photospheres.



Figure 1.15. (a) GoPro Fusion camera [5], (b) Samsung Gear 360 [20], (c) Garmin Virb [16], (d) Nikon KeyMission 360 [21], (e) Ricoh Theta V [22]

As these cameras continue to develop and consumers continue to prefer more compact cameras, there has been a push to make the form factor of these cameras as small as possible. Most of the current cameras on the market place the two fisheye lens modules back-to-back, which makes the cameras relatively thick; in general, the thickness of a virtual reality camera is limited by the vertex-to-vertex distance between the front elements of the two fisheye lenses. To make the camera thinner, GoPro has designed the Fusion camera such that the two lens modules are placed side-by-side [Fig. 1.16] [5]; this minimizes the camera's thickness, but creates a parallax issue for objects which are close. The Ricoh Theta took a different approach and uses glass prisms to fold each fisheye lens to minimize the vertex-to-vertex thickness dimension of the camera [22].

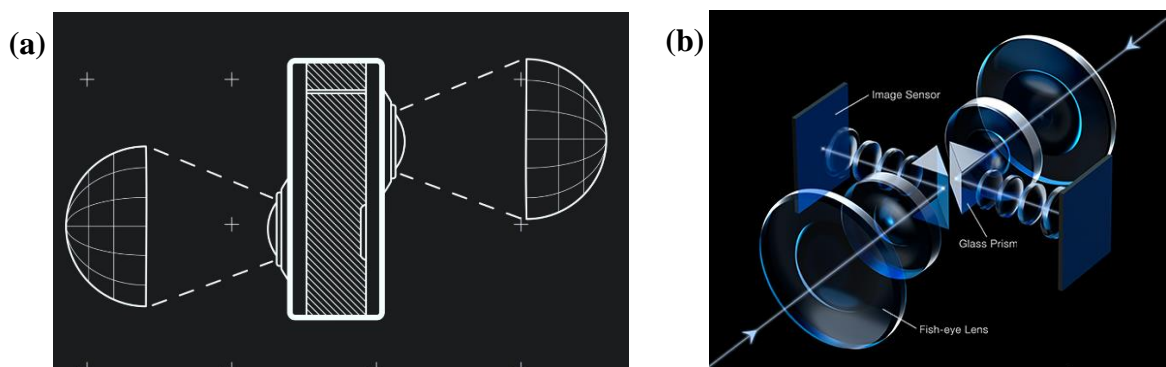


Figure 1.16. (a) GoPro Fusion schematic showing side-by-side lens placement [5], (b) Ricoh Theta lens schematic showing folded optical path via two glass prisms [22]

Folded optical systems in consumer electronic devices are uncommon. However, as the consumer electronics market continues to move towards smaller and slimmer devices, the author expects that these folded imaging systems may become more frequent. The Ricoh Theta uses prisms to fold each optical system to make the camera as thin as possible and is still able to obtain very high-quality images. As is shown in Fig 1.16, Ricoh has designed the lens such that the two negative meniscus lenses are placed on one side of the optical path, with the rest of the positive lenses are placed after the prism. While the consumer devices industry is pushing technology be as thin and minimal as possible, having this reduction in camera size can be very advantageous. Other cameras of this type are significantly thicker, because they do not utilize folded optical systems.

A comparison of the dimensions of all of the consumer-focused virtual reality cameras discussed so far are listed in Table 1.1; as shown, the Ricoh Theta is almost half as thick as the next closest option by folding the optical system. The next thinnest camera is the GoPro fusion which suffers from parallax issues at short object distances, and third is the Samsung Gear 360.

VR Camera Name	Vertex-to-Vertex Thickness	Height	Width
Ricoh Theta V	23mm	130mm	45mm
GoPro Fusion	39mm	73mm	75mm
Samsung Gear 360	45mm	101mm	46mm
Nikon Keymission 360	61mm	61mm	66mm
Garmin Virb 360	70mm	59mm	39mm

Table 1.1 Center thickness, height, and width dimensions of common virtual reality cameras

1.3 Thesis Content

In this master's thesis report, the author designs a 1.3mm F/2.8 folded fisheye lens which is intended to be used in a compact virtual reality camera for consumers where the primary goal was to minimize the vertex-to-vertex thickness of the imaging module when two lens systems are placed back-to-back while maintaining strict image quality requirements. The author utilizes a powered prism to fold the optical path of each fisheye lens. The powered surfaces on the prism allow the author to remove the 2nd negative meniscus lens which is required at the front of a fisheye lens design, which brings the first lens element and the prism closer together to minimize the final package dimensions. The vertex-to-vertex thickness of the two-lens system described in this report is 25mm, which would allow the form factor of a future virtual reality camera to be much more compact than most current products on the market.

Lenses which are used in consumer devices must be cost efficient and manufacturable while maintaining great image quality; because the molded glass prism used in this design is expected to be relatively expensive, the rest of the optical design uses only 8 spherical glass elements to reduce the cost of the final lens assembly. Nevertheless, the system maintains less than 2 μ m of lateral chromatic aberration over the full 190-degree field with greater than 50% MTF at all fields up to the Nyquist frequency of the sensor which the lens is designed to be used with.

The unique way that consumers view the footage captured from these virtual reality cameras makes it such that stray light and ghosts can be much more distracting compared to traditional image formats. The stray light of the folded fisheye lens is thoroughly evaluated in the non-sequential optical design software, FRED. While assuming standard antireflection coatings on all of the lens elements, the optimal location of the highly reflective ultraviolet and infrared cut

off filters are chosen through an extensive ghost analysis of the folded fisheye lens across it's entire field of view.

Chapter 2 describes many of the unique properties of fisheye lenses including their design construction and distortion profiles, pupil aberrations, entrance pupil shift, and relative illumination characteristics. The folded fisheye lens is designed to be used with a 1/2.7" ON-Semiconductor AR0237 CMOS image sensor which has a RGGB Bayer color array with 3 μ m pixels and enables synchronization controls for multi-camera support [23]; this sensor will allow the two image sensors to be synchronized during video recording while capturing high resolution content in a compact form factor. Many of the optical requirements of the folded fisheye lens are dependent on the characteristics of the AR0237 sensor, such as MTF, lateral color, chief ray angle, and image circle size. All requirements for this lens are derived and outlined in Chapter 3.

The 1.3mm F/2.8 folded fisheye lens is designed and thoroughly evaluated in Chapter 4. The glass material choices, optimization process, tolerance analysis, and manufacturability yield analysis are all described in detail; in addition, the entrance pupil shift of the folded fisheye lens is measured, and an analysis of the total internal reflection interface of the prism is performed to ensure that 100% of the rays in the system will reflect in the glass prism. The size and details of how the two fisheye lens modules will be assembled is discussed, and the approximate stitch location for the final camera configuration is estimated. Chapter 5 provides a thorough stray light and ghost analysis of the folded fisheye lens, and coating properties for each surface are chosen to optimize the stray light performance of the final camera system.

This thesis report concludes with an overview of the folded fisheye lens system, expectations for how a potential camera would perform using these lenses, and suggestions for future work are provided by the author.

2 FISHEYE LENS PROPERTIES

Fisheye lenses are a unique type of imaging lens; To capture fields of view which are greater than 180-degrees, these lenses must have very small focal lengths and large amounts of distortion. Having small focal lengths leads to all fisheye lenses taking the structure of a reverse telephoto lens to enable back focal lengths long enough to fit inside of a camera enclosure; in addition, the distortion introduces significant amounts of pupil aberration which allow fisheye lenses to have very high relative illumination compared to ordinary photographic lenses. This Chapter discusses the various properties of photographic fisheye lenses.

2.1 Reverse Telephoto Properties

Fisheye lenses take the form of a reverse telephoto lens, which consists of a negative group of elements in the front of the lens assembly, followed by a stronger group of positive elements behind them. Reverse telephoto lenses by design have back focal distances larger than the effective focal length of the systems. Fisheye lenses require very small effective focal lengths, making this property advantageous; This reverse telephoto structure ensures that a fisheye lens can capture a very wide field of view while still having long enough back focal lengths to fit into a camera assembly.

A telephoto lens and reverse telephoto lens are shown in Fig. 2.4, where both lenses are shown to have the same effective focal length. In the telephoto lens, where a positive lens element comes before a negative lens element, the back focal length is shorter than the effective focal length. For the reverse telephoto lens, where a negative lens comes before a positive lens, the back focal length is longer than the effective focal length. While the longer back focal distance can be advantageous for camera applications, reverse telephoto lenses do require longer total track lengths

compared to telephoto lenses with the same focal length which can be a disadvantage in applications where a compact form factor is preferred.

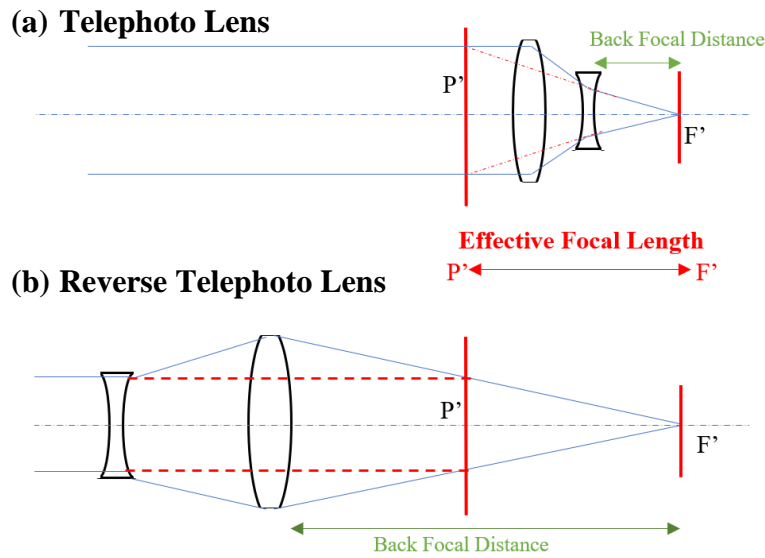


Figure 2.1. Lens structure differences between (a) Telephoto Lens and (b) Reverse Telephoto Lens with Equal Effective Focal Lengths

Having a large field of view requires a very small focal length; in order for a fisheye lens to have a back focal length long to allow room for a fold mirror in a DSLR camera, for example, they must take the form of a reverse telephoto lens.

2.2 Fisheye Lens Structure

Historically, fisheye lenses are constructed with strong negative meniscus lenses in the front group of elements and positive elements on the other side of the aperture stop. This meniscus shape is required to capture more than a 180-degree full field of view; because the aperture stop is on-axis, rays with field angles greater than 90 degrees would otherwise be impossible to enter the stop. The shape of the negative meniscus lenses are not only used to diverge the rays entering the rest of the system to allow the chief ray to enter the aperture stop, but the shape of this lens also

decreases the incident angle on the first lens element surface of the higher field heights which reduces Fresnel reflections and increases relative illumination.

Most modern fisheye lens designs utilize two or more meniscus lenses at the front of the optical assembly to further reduce the high field angles entering the rest of the lens. In general, the greater the field of view is, the more meniscus lenses will be required. For example, the Nikkor 6mm F/2.8 fisheye which has a 220-degree full field of view requires three negative meniscus lenses at the front of the lens [Fig. 2.2] [11].

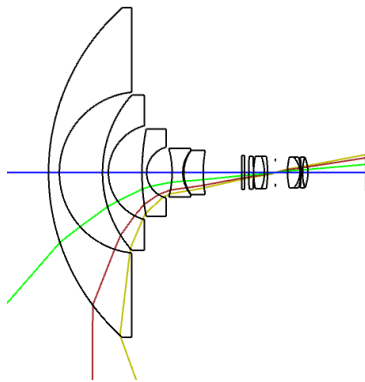


Figure 2.2. Nikkor 6mm F/2.8 220-degree fisheye lens structure showing 3 negative meniscus lenses in front of the assembly [11]

Since the Hill Sky Lens, almost all fisheye lenses have a positive achromatic doublet placed behind the aperture stop to correct for lateral color aberration. By optimizing the shape of the buried surface, the chromatic aberration across the field of view can be corrected so that sharp polychromatic images may be obtained. When further correction is needed, it is common to see a negative achromatic doublet placed before the aperture stop in addition to the positive achromat behind the stop; this can be seen in the Nikkor 6mm F/2.8 fisheye lens [Fig. 2.2]. As fisheye lenses become more compact and require higher performance, it is common to see more lens elements placed in throughout the assembly to control aberrations. In a few cases, aspheric surfaces are used for the first lens element to control the distortion profile across the image.

2.3 Distortion Properties

For ordinary imaging lenses with little to no distortion, the image height is proportional to the effective focal length and the tangent of the half field of view, and the magnification is constant across the field of view. This is commonly referred to as a ‘rectilinear’ lens, or an $f \cdot \tan\theta$ distortion profile. However, as the half field of view of a lens increases towards 90° , $\tan\theta$ grows to infinity, meaning that this relationship between image height and field of view cannot adequately describe fisheye lenses which have full fields of view greater than 180-degrees [8].

R. Hill’s paper, he describes three different distortion or mapping functions to project a hemispherical image onto a planar surface which are stereographic projection, equidistant projection, and orthogonal projection [2]. In addition to these, equisolid projection is commonly used for photographic fisheye lenses [4]. These projection methods can more accurately describe the differences between distortion profiles of fisheye lenses than the standard rectilinear profile.

Equidistant projections follows the equation

$$y = f \theta \quad (2.1)$$

where y denotes the half image height, f is the effective focal length of the lens, and θ is the half field of view in object space. The Hill Sky Lens follows the equidistant distortion profile [2], as well as many other fisheye and wide angle lenses. Because the image height is directly proportional to the field angle without any additional compression at the higher fields, this profile is common for fisheye lenses used in scientific applications.

Orthogonal projection is proportional to the sine of the half field angle, and can be represented as

$$y = f \sin(\theta). \quad (2.2)$$

The orthogonal distortion profile results in the highest barrel distortion at the edge of the field of view out of all of the fisheye distortion profiles. As the field increases towards 90 degrees, $\sin\theta$ becomes 1, and the sagittal magnification decreases to 0 while the tangential magnification is constant; in the case of a circular object, the image of that circle will appear circular in the center of the field, elliptical in the middle, and become compressed into a line at the 90-degree field height [4]. In addition, because $\sin\theta$ has a peak of 1 at 90 degrees, the image height decreases past that field of view limiting the full field of view of orthographic fisheye lenses to 180 degrees. Because of this loss in information at the edge of the field, fisheye lenses with orthogonal distortion are typically not used for scientific use; however, these lenses do create very unique images and thus are often used in photographic fisheye lenses.

Stereographic projection has the least amount of barrel distortion out of all of the distortion profiles. Stereographic projection is similar to rectilinear projection in that it is also proportional to the tangent of the half field of view, and is represented as

$$y = 2f \tan(\theta/2). \quad (2.3)$$

The tangential and sagittal magnification for all points in the image plane are always equal for stereographic projection which ensures that the image of an object is always proportionally the same, contrary to how the other fisheye distortion profiles compress the image along one axis. For the same circular image example used previously, a circle will appear circular for all field heights in a fisheye lens with stereographic distortion, but the size of the circle increases until it is two times the size of the on-axis circle at the 90-degree field [4].

Equisolid projection is represented as

$$y = 2f \sin(\theta/2); \quad (2.4)$$

This distortion exhibits more barrel distortion than equidistant projection but less than orthogonal projection, and is the most commonly used distortion profile in fisheye lenses used for photography. When using this projection method, the area of the object in image space corresponds to the solid angle in object space, and this ratio is a constant for all field heights, leading to its name “equi-solid-angle” projection [4]. The sagittal magnification decreases as the field increases, while the tangential magnification increases; this causes a circular image to become more elliptical as the image is traced off-axis. A comparison of how a circular object would appear across the field of view for orthogonal and equisolid distortion is shown [Fig. 2.3].



Figure 2.3. Demonstrating image compression at edge of field for (a) Orthogonal Distortion and (b) Equisolid Distortion

Each distortion profile creates a different looking image in the end; to help visualize the differences, Y. Yan's paper from 2016 shows four different distortion profiles of the same scene [Fig. 2.4] [4]. As expected, Stereographic projection exhibits the least amount of barrel distortion, whereas orthogonal projection fully compresses the image at the edge of the field. Equidistant and equisolid projection both show less barrel distortion than orthogonal projection but more than stereographic projection; equisolid projection demonstrates slightly more barrel distortion at the edge of the field of view, but the object appears slightly larger in the center of the field creating more of a ‘bubble’ appearance.

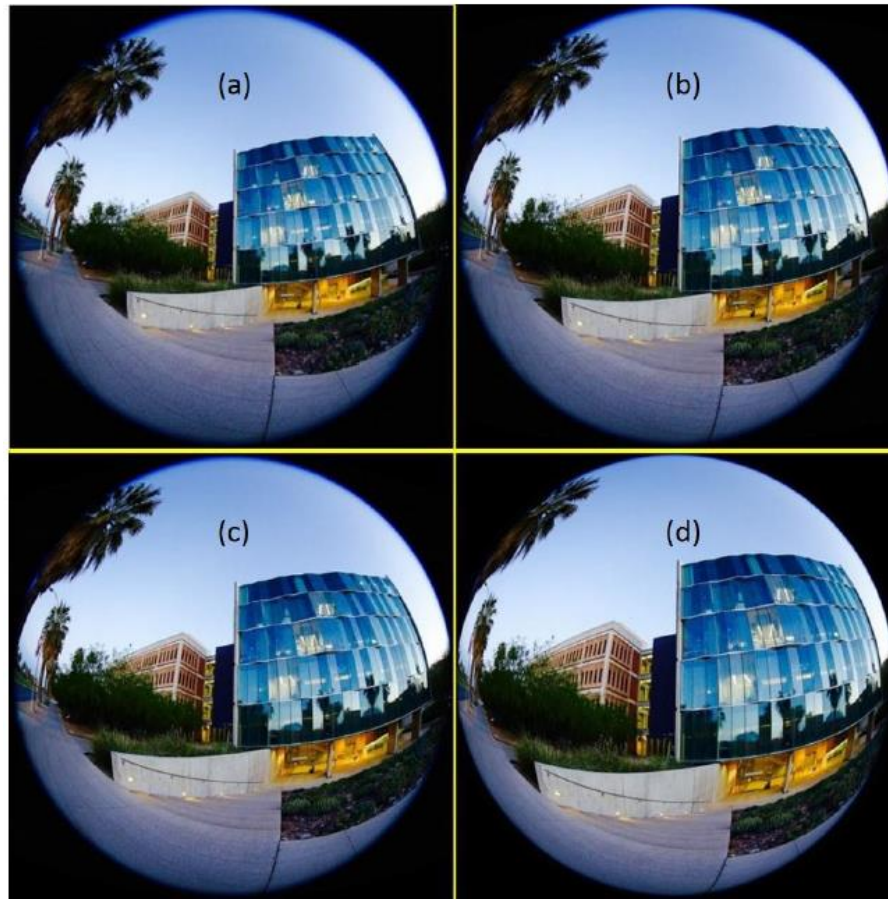


**Figure 2.4. Different distortion profile images for the same object, demonstrating
(a) stereographic distortion, (b) equidistant distortion, (c) equisolid distortion, and
(d) orthographic distortion [4]**

These four projection methods are the most common way to describe the distortion which is present in fisheye lenses. However, it should be noted that these profiles and equations which represent each distortion act more as guidelines for how to refer to the distortion, and not so much an exact equation which must be followed in an optical prescription. Many times, the final distortion profile of a lens will be a variant of these equations; for example, the Nikkor 16mm F/2.8 fisheye lens follows equisolid projection, but has a distortion profile of $y=1.8\sin(\theta/1.78)$ instead of equisolid projection's equation $y=2\sin(\theta/2)$. Allowing the distortion to vary can aid the optical designer in correcting other aberrations during the optimization process.

To conclude, all four of the fisheye distortion profiles are plotted in Fig. 2.5, along with the rectilinear distortion which is used to describe ordinary photographic lenses.

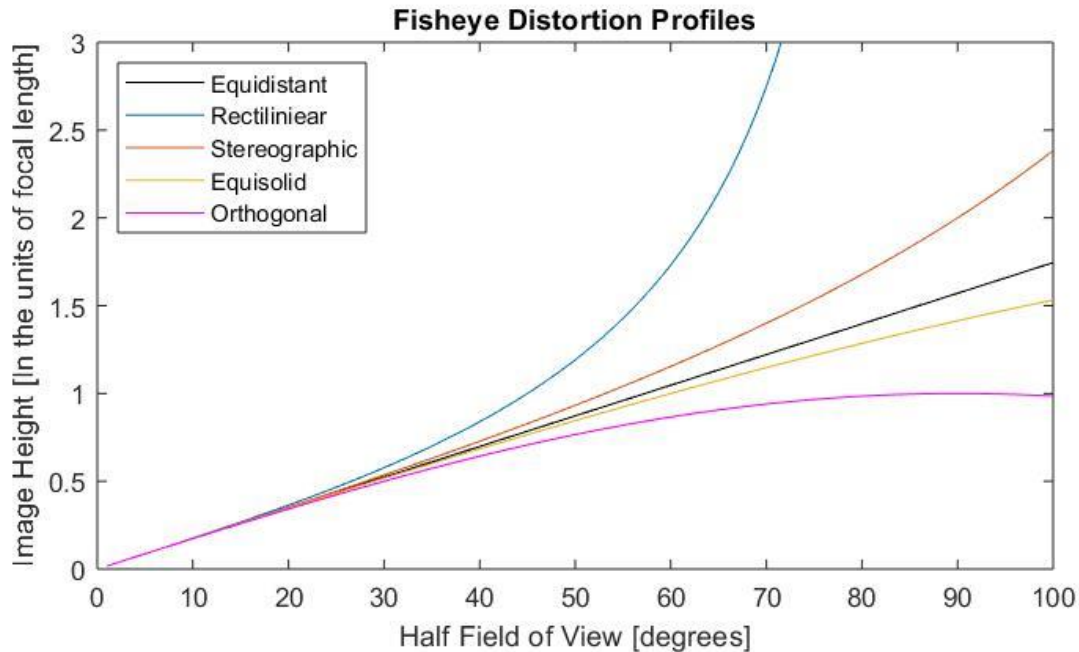


Figure 2.5. Image height versus field of view plots for each of the fisheye distortion profiles

Distortion profiles with low image heights at high field angles will exhibit more barrel distortion; in this case, orthogonal distortion has the most barrel distortion at the edge and stereographic shows the least. Any profiles within this range will show varying amounts of barrel distortion across the image.

2.4 Entrance Pupil Properties

The entrance pupil of a lens system is the image of the aperture stop in object space; for ordinary photographic lenses which have low amounts of distortion, the entrance pupil lies at the same axial position for all field angles. However, this is not the case for lenses which exhibit large amounts of pupil aberrations, like fisheye lenses.

In fisheye lenses, the negative meniscus lenses in front of the aperture stop will introduce pupil spherical aberration; the spherical aberration in the pupil will cause the entrance pupil location to translate laterally for different fields of view, where the displacement increases as the cube of the field of view [29]. This effect is commonly referred to as entrance pupil walking, and is a significant effect in wide angle and fisheye lenses. As shown in Fig. 2.6, the entrance pupil position changes quite drastically between a 0-degree field, 45-degree field, and 90-degree field in the Nikkor 8mm F/8 fisheye lens. Not only is the position along the optical axis changing with field height, but the pupil is also tilted in angle.

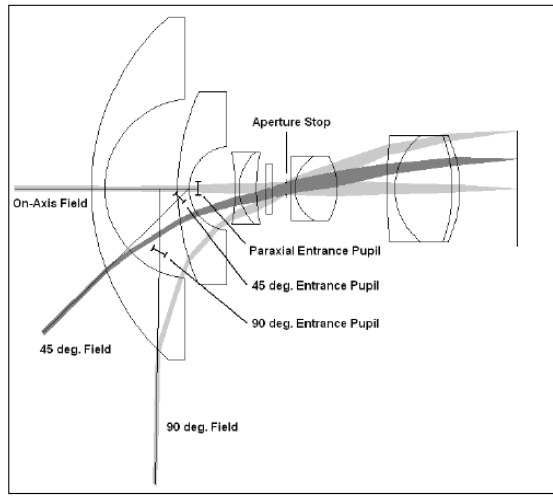


Figure 2.6. Entrance pupil walk in the Nikkor 8mm F/8 fisheye lens [8]

In addition to a large presence of pupil spherical aberration causing the entrance pupil walk, fisheye lenses exhibit large amounts of pupil coma and create an elliptically shaped entrance pupil which becomes more elliptical as the field of view increases. The pupil coma is present due to the large amounts of image distortion. The two are related by the equation

$$\bar{W}_{131} = W_{311} + H \cdot \frac{\Delta(\bar{u}^2)}{2} \quad (2.5)$$

where \bar{W}_{131} is the pupil coma, W_{311} is the image distortion, H is the Lagrange invariant, and \bar{u} represents the chief ray angle [29]. As the field angle increases, the ellipticity of the pupil

increases; however, the area of the pupil increases also with field, which allows fisheye lenses to have higher irradiance in the off-axis fields than the on-axis field. This effect is known as the Slyusarev effect [29], and allows fisheye lenses to break the standard $\cos^4 \theta$ relative illumination trend. Fig. 2.7 demonstrates coma aberration in the pupil, and how the elliptical pupil will contain a larger area compared to the on-axis pupil.

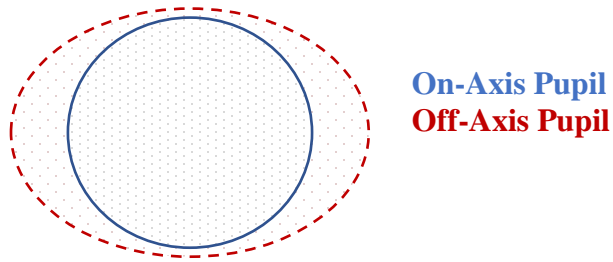


Figure 2.7. Off-axis coma aberration seen in the entrance pupil of a fisheye lens.

To visualize the aberration in a fisheye lens' entrance pupil, the author mounted a compact fisheye lens onto an electroluminescent panel which exhibits relatively Lambertian behavior. As the fisheye lens is rotated, the entrance pupil of the lens can be seen translating axially and changing from a circular shape on-axis to a highly elliptical shape at 90 degrees of rotation where the area inside the pupil changes as a function of rotation angle [Fig. 2.8]. In this example, the lens is rotated about the on-axis entrance pupil location, and the axial pupil shift can also be observed.

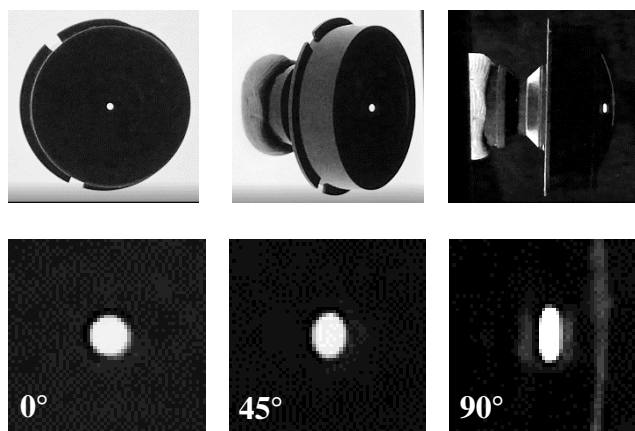


Figure 2.8. Off-axis entrance pupil aberration seen in a compact fisheye lens from 0° to 90°

These pupil aberrations can cause some complications when tracing rays in optical design software with fisheye lenses. If the rays are aimed at the paraxial entrance pupil location, as is a common assumption, the chief ray will not pass through the center of the aperture stop, and rays will vignette or may miss the aperture stop completely.

Fortunately, most sequential optical design software like Zemax and CodeV include ray aiming tools which will ensure that the chief ray passes through the center of the stop for every field. This is an iterative process, where the program first aims the rays at the paraxial entrance pupil, and changes that location until the chief ray has 0 height at the aperture stop; because this process is iterative, it takes more time and can slow down some analysis' in Zemax. Figure 2.9 shows the difference in rays being traced in Zemax when ray aiming is turned on and off; as shown, the 75° field cannot be traced without ray aiming, and the 50° field is highly vignetted. When ray aiming is turned on, the chief ray for each field height passes through the center of the aperture stop, and rays are traced properly.

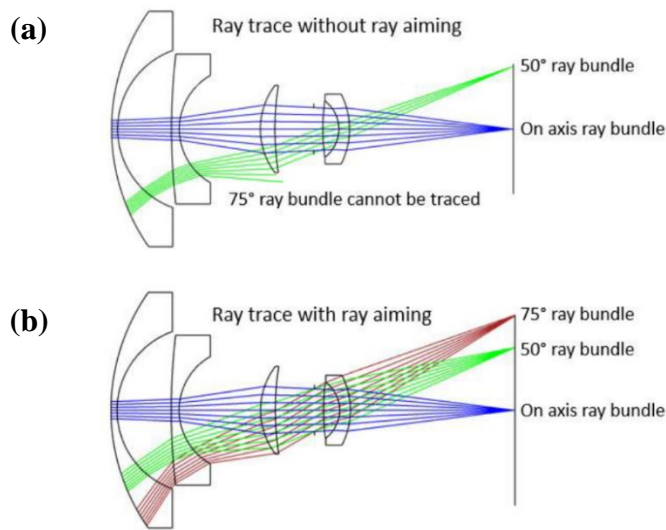


Figure 2.9. (a) Fisheye lens before ray aiming is turned on. (b) Fisheye lens with ray aiming turned on [4]

Unfortunately, at the time of the author writing this report, the non-sequential design software FRED does not have an advanced ray aiming tool like Zemax. Because of this, the entrance pupil shift of the folded fisheye lens must be mapped out and each field height must be manually aimed when performing a stray light analysis in non-sequential design software.

2.5 Relative Illumination

Relative illumination is defined as the ratio of light between the center of the image and the edge of the image. In standard photographic lenses, the relative illumination falls off according to the radiometric $\cos^4 \theta$ law, where the irradiance falls off as \cos^4 across the image plane [8]. In this case, E represents the off-axis illumination, E_0 represents the on-axis illumination, and θ is the chief ray angle in image space.

$$E = E_0 \cos^4 \theta \quad (2.6)$$

In fisheye lenses, the large amounts of barrel distortion cause significant pupil coma; As mentioned in Chapter 2.4, the Slyusarev effect [29] allows fisheye lenses to break the standard $\cos^4 \theta$ relative illumination trend, because pupil coma causes the area of the pupil to increase as the ray angle increases [Fig. 2.7]. The increased size of the pupil allows the imaging system to collect more light as the field angle increases, which increases the relative illumination for the higher field heights at the expense of barrel distortion; in general, the greater the barrel distortion is present in an image, the higher that the relative illumination will be at the edge. In some cases, the relative illumination can be greater than 1 at higher field heights.

The 210 degree field fisheye lens example in the Zemax documentation [30] exhibits the type of relative illumination behavior attributed to the Slyusarev effect [Fig 2.10]. In this lens, the relative illumination reaches a peak at the 105-degree half field of view, which is roughly 20% higher than the illumination in the center field of this lens.

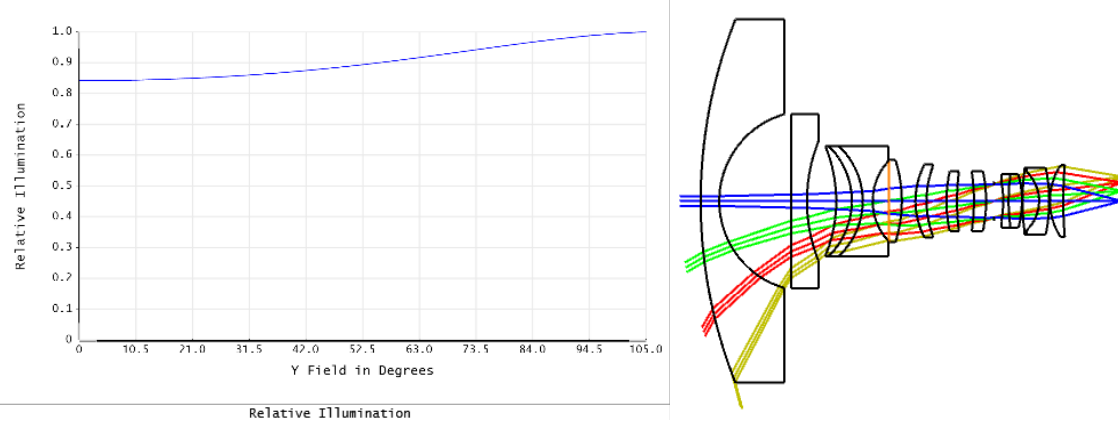


Figure 2.10. A 210-degree field of view fisheye lens exhibiting the Slyusarev effect, where the illumination is greater at the edge of the field of view than in the center field [30].

This type of relative illumination behavior can be incredibly advantageous to a lens designer; if required, the optical designer can intentionally vignette the rays in the higher field heights to control optical aberrations while still maintaining an acceptable relative illumination profile. A tradeoff between relative illumination, barrel distortion, and image quality can be done to optimize the performance of the lens.

2.6 Depth of Field and Hyperfocal Distance

In practical imaging lenses, there is generally some allowable image blur that defines the performance requirement of the optical system [32]; in digital image systems, this is often defined to be two times the pixel pitch of the image sensor being used. In the past, this was determined by the expected viewing conditions such as the size and distance between the image and the viewer and the minimal object size viewable by the human eye. The depth of field describes the amount that a detector can be shifted from the nominal image plane before the resulting blur exceeds some criteria, usually named B' . The depth of field, DOF, is proportional to this blur criteria and the F-number of the lens, defined by equation 2.7.

$$DOF = \pm B' * F/\# \quad (2.7)$$

With this depth of field range, there is a range of distances in object-space where the image will appear in focus, generally referred to as L_{near} , and L_{far} [Fig. 2.11]. These values can be obtained geometrically.

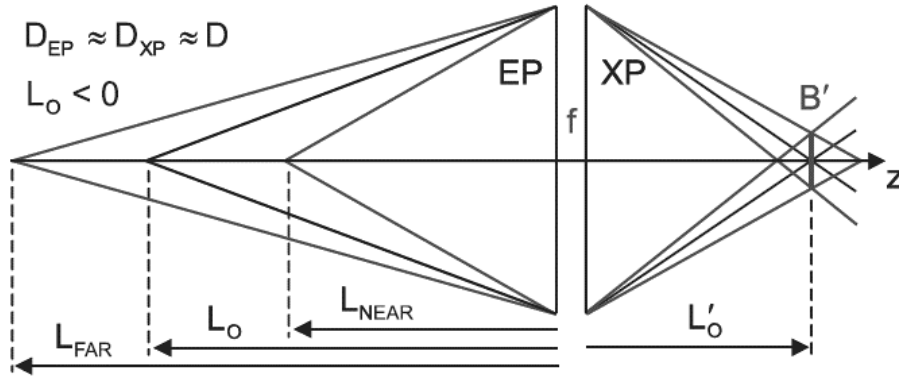


Figure 2.11. Depth of Field and Hyperfocal Distance schematic [32]

L_{near} is proportional is represented by

$$L_{near} = \frac{L_0 f D}{f D - L_0 B'} \quad (2.8)$$

and L_{far} is expressed as

$$L_{far} = \frac{L_0 f D}{f D + L_0 B'} \quad (2.9)$$

where f is the focal length of the lens, D is the diameter of the pupil, L_0 is the nominal object distance which results in the nominal image plane location L_0' , and B' is the blur criterion which is generally a constant related to the pixel pitch on the image sensor.

An important location in the depth of field is the object location where L_{far} first becomes ∞ ; this location is commonly referred to as the hyperfocal distance, L_h , and represents the minimal object-distance in which everything from that distance to infinity will be equally in focus on the detector. When an imaging system is focused at the hyperfocal distance, everything from $\frac{L_h}{2}$ to ∞ will be equally focused. The hyperfocal distance is represented mathematically as

$$L_H = -\frac{fD}{B'} \quad (2.10)$$

where L_{near} and L_{far} then become

$$L_{near} \approx \frac{L_h}{2} \quad (2.11)$$

$$L_{far} = \infty \quad (2.12)$$

respectively.

An important relationship can be seen in the hyperfocal focal distance equation, that the hyperfocal distance is directly proportional to the focal length of the lens being used. Fisheye lenses demonstrate the quality of having very small focal lengths, which makes L_H very short. As L_H decreases, L_{near} becomes very small, where L_{far} is always equal to ∞ . Because of this, fisheye lenses with short focal lengths commonly have the quality of exhibiting very large depth of fields, where objects from very close to very far are all equally in focus. In addition, the depth of field is proportional to the F-number of the system; for very large F-numbers, the depth of field also increases.

In the folded fisheye lens which the author has designed, the focal length is only 1.3mm with an exit pupil diameter of 2.7mm and a blur criterion of 0.006mm. Using these numbers, $L_H = 585mm$, meaning that if the lens is focused for an object distance of 585mm, everything from $L_{near} = 293mm$ to $L_{far} = \infty$ will be within the tolerable blur limit and are in focus. Practically, this means that every object which is approximately one foot or further away from the first lens element will be equally in focus; This can be advantageous for many applications where it is ideal for all objects to be in focus, such as automotive, machine vision, and street photography.

2.7 Diagonal versus Circular Fisheye Lenses

Because of the rectangular shape of film and image sensors, most ordinary photographic lenses are designed such that the diameter of the image circle matches the diagonal of the image

sensor. The corner of the image then shows the 100% IH location of the image where the vertical and horizontal dimensions do not show the full field of view extent of the lens; this is referred to as a ‘diagonal lens.’ Contrarily, if the image circle diameter is the same size or slightly smaller than the vertical dimension of the image sensor, the full image circle will be captured. Lenses which have an image circle which is smaller than the vertical dimension of the sensor are referred to as ‘circular lenses’ [4]. Because of the ability to capture a hemispherical image with 180-degree field of view or greater, fisheye lenses will sometimes be designed such that the image circle lies within the image sensor. Fisheye lenses which are designed to have the image circle inside of the sensor are referred to as circular fisheye lenses, where fisheye lenses which are designed to have the image circle match the diagonal of the sensor are referred to as diagonal fisheye lenses. Both diagonal and circular fisheye lenses find use in photography, whereas scientific applications tend to use circular fisheye lenses. The difference in these image circle dimensions are demonstrated in Fig. 2.12.

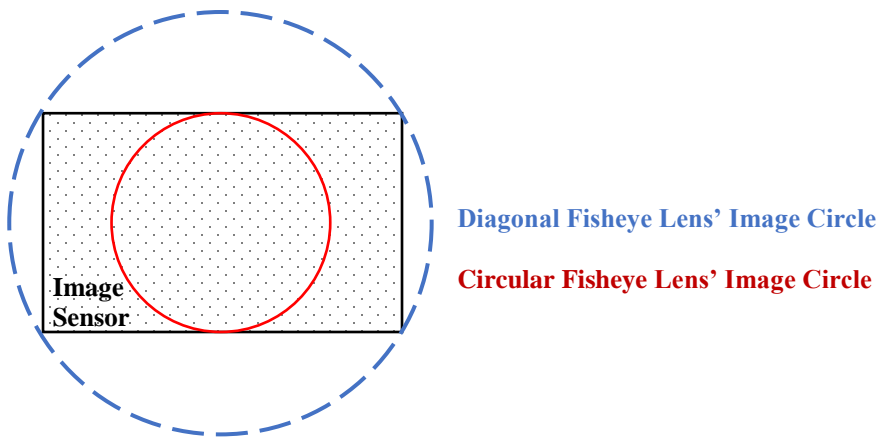


Figure 2.12. Diagonal Fisheye Lens versus Circular Fisheye Lens

An example of the difference in how much of a scene a circular fisheye lens can capture in comparison to a diagonal fisheye lens is shown in Fig. 2.13. In this example, the object is the Meinel College of Optical Sciences in Tucson, Arizona; The circular fisheye lens allows the full 180-degree field of view of this fisheye lens to be seen, whereas the diagonal fisheye lens is

designed so that the diagonal of the sensor fits to the edge of the field of view, and a significant amount of the information is lost in the vertical and horizontal dimensions.

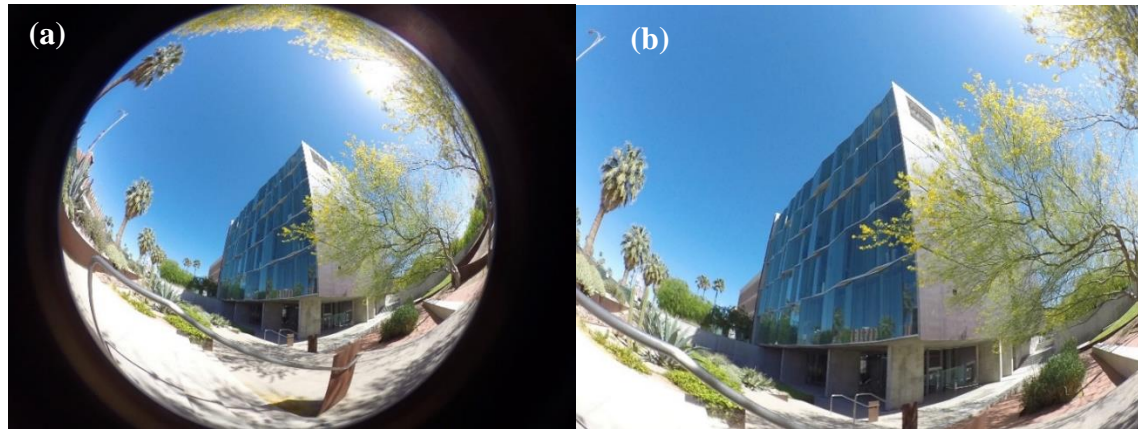


Figure 2.13. (a) Circular fisheye image versus (b) diagonal fisheye image

Many of the fisheye lenses which were first introduced to the market were circular fisheye lenses; however, in today's market, diagonal fisheye lenses are more common. Most action cameras and automotive back up cameras utilize diagonal fisheye lenses, and even fisheye lenses for DSLR cameras are most commonly designed to be diagonal fisheye lenses. Diagonal fisheye lenses will cut out some of the information, and thus a full hemispherical image will not be captured.

The optical design for some applications still require circular fisheye lenses. Some examples are surveillance cameras where the full hemispherical image is required, and virtual reality cameras where two hemispherical images are captured and combined into one full photosphere. In this master's report, the author designs a circular fisheye lens, because the entire hemispherical image information is needed to reconstruct a full 360° photosphere. Thus, the diameter image circle of the lens that the author has designed is defined by the vertical dimension of the CMOS image sensor which was selected. Some resolution and sensor real estate is lost; nonetheless, it is a requirement to allow a full unwrapping the 360° photosphere.

3 OPTICAL DESIGN REQUIREMENTS

Optical systems used in consumer devices must meet requirements which can make the design very challenging; the imaging system must be cost efficient and manufacturable, which limits the types of optical materials that can be used, the number of aspherical elements utilized, and the total number of elements in the system. As modern CMOS image sensors continue to achieve high resolution with increasingly smaller pixels, high quality imaging lenses with sharp image quality are required all while maintaining a compact form factor.

As discussed in Chapter 1.2, there is a strong demand for virtual reality cameras to be more compact in size. This push for the fisheye lenses used virtual reality cameras to become more compact has been a motivating factor for the author to design a folded fisheye lens which will allow a reduction in camera thickness while avoiding parallax error; The primary goal is to minimize the center-to-center thickness of the entire two-lens imaging module when two fisheye lenses are placed back-to-back at the prism interface.

The folded fisheye lens is designed to be used with a 1/2.7" ON-Semiconductor AR0237 CMOS image sensor which uses a RGGB Bayer color array with 3 μ m pixels and enables synchronization controls for multi-camera support [23]; this sensor will allow the two image sensors to be synchronized during video recording while capturing high resolution content in a compact form factor.

The characteristics of the image sensor drive the optical requirements of an imaging lens; thus, many of the optical requirements of the folded fisheye lens are dependent on the characteristics of the AR0237 sensor. This Chapter outlines all optical requirements that the folded fisheye lens design must meet, per the properties of the AR0237 CMOS image sensor.

3.1 Package Dimensions and First-Order Requirements

Based on current virtual reality camera thicknesses on the market [Table 1.1], the author aims to design a system where the vertex-to-vertex thickness of the two-lens module is less than 30mm; this would place this imaging module in between the thickness of the Ricoh Theta camera and the GoPro Fusion camera, while ensuring that this system doesn't suffer from parallax issues. Because the primary goal is to minimize this vertex-to-vertex thickness, the author has set a more relaxed goal for the width of the two-lens system to be less than the width of the GoPro Fusion which is 75mm. Figure 3.1 demonstrates the thickness-to-thickness dimension requirement in red and the sensor-to-sensor width requirement in blue.

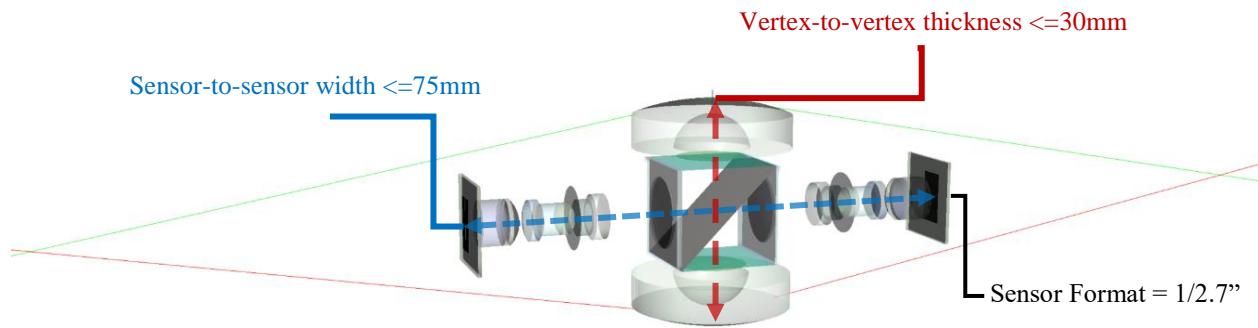


Figure 3.1. Package requirements for the folded fisheye lens, with thickness-to-thickness requirement illustrated in red, and package width requirement illustrated in blue.

As can also be seen in this image, the location where the maximum field of view of each lens meets together is dependent on the field of view of each lens; a higher field angle results in a closer object distance at which the images can be stitched together. However, it is difficult to maintain good image quality out to these extreme fields of view, leading to a tradeoff between stitch distance and image quality at the stitch line. To ensure that objects which are relatively close can be stitched within the photosphere, the author aims to design the lens to have a full field of view of 190 degrees or greater.

The F-number of the lens is designed to have a maximum aperture of F/2.8 to ensure that the MTF will be high enough to match the resolution of our sensor, and that enough light can be collected for short exposure times in the camera. As described in Chapter 2.6, the short focal length and depth of field characteristics of fisheye lenses will still allow for the depth of field to be very large at a F-number of 2.8. This lens will likely be a fixed-focus lens, meaning that there will not be any autofocus mechanisms used in the system; thus, this long depth of field is required.

3.2 ON-Semiconductor AR0237 CMOS Image Sensor Considerations

Most of the optical requirements such as MTF, chief ray angle, relative illumination, wavelength weighting, chromatic aberration, depth of focus and F-number, and back focal length are all dependent on the image sensor which is selected. Most compact consumer electronics cameras, like the virtual reality cameras discussed in Chapter 1.2, use CMOS image sensors ranging from $\frac{1}{4}$ " to $\frac{1}{2}$ " image format sizes. It is important to select a sensor which is readily available and fits the use-case application.

ON-Semiconductor is a sensor company whose products are frequently used in consumer electronic devices. After browsing their available sensors, the author chose the AR0237 CMOS Image Sensor, which has a $1/2.7$ " sensor format with $3\mu\text{m}$ pixels in an RGGB Bayer format. The ON-Semiconductor website recommends this sensor for many applications, including automotive dash cameras, rear-view cameras, and high definition cameras that wish to output high frame rate video. Most importantly, the AR0237 supports advanced line synchronization for multi-camera support [23]; this will allow the two sensors which are paired with two fisheye lenses to be synchronized as they read the data out of the image. The AR0237 has a resolution of 2.1 megapixels using active pixel dimensions of 1928 pixels by 1088 pixels with a $3\text{ m} \times 3\mu\text{m}$ pixel size, allowing full 1080P HD video capture at 60 frames per second [Fig. 3.2].

Table 1: Key Parameters		
Parameter	Typical Value	
Optical format	1/2.7-inch (6.6 mm)	
Active pixels	1928(H) x 1088(V) (16:9 mode)	
Pixel size	3.0 μm x 3.0 μm	
Color filter array	RGB Bayer, RGB-IR	
Shutter type	Electronic rolling shutter and GRR	
Input clock range	6 – 48 MHz	
Output clock maximum	148.5 Mp/s (4-lane HiSPi) 74.25 Mp/s (Parallel)	
Output	Serial Parallel	
	HiSPi 10-, 12-, 14-, 16-, or 20-bit 10-, 12-bit	
Frame rate	1080p 60 fps Linear HiSPi 30 fps Linear Parallel 30 fps Line Interleaved HiSPi 15 fps Line Interleaved Parallel	
Responsivity	4.0 V/lux-sec	
SNR _{MAX}	41 dB	
Max Dynamic range	Up to 96 dB	
Supply voltage	I/O Digital Analog HiSPi	1.8 or 2.8 V 1.8 V 2.8 V 0.3 V - 0.6 V (SLVS), 1.7 V - 1.9 V (HiVcm)
Power consumption (typical)	< 300mW Line interleaved 1080p30 <190mW 1080p30 Linear Mode	
Operating temperature	-30°C to +85°C ambient	
Package options	10x10 mm 80-pin iBGA 11.43x11.43 mm 48-pin mPLCC	

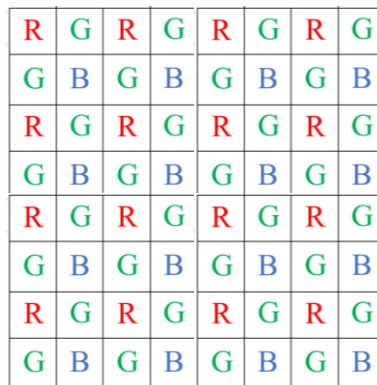


Figure 3.2. ON-Semiconductor AR0237 Key Parameters and RGGB Bayer format [23]

The operating temperature ranges from -30C to +85C, which will allow the imaging module to be used in harsh environments; this is a common operating range for consumer electronics devices. Overall, the AR0237 image sensor fits all needs for this application while enabling high resolution video output with synchronized readout between the two sensors used in the virtual reality camera

3.2.1. Sensor Package Dimensions and Back Focal Length Requirements

This system is assumed to be used in a compact consumer electronics camera, so there is no need to allow for space for a fold mirror which would be present in a DSLR. The main limitations to the back focal distance will be the package dimensions of the AR0237 CMOS image

sensor. This sensor cover glass material type, thickness, length and width dimensions, and distance between the cover glass and the sensor will all be used in our optical design. In addition, the tolerances reported for the sensor cover glass will be needed when performing a tolerance analysis of this lens.

The N-BK7 cover glass' dimensions are 10.7mm x 10.7mm x 0.385mm, and the distance from the bottom of the sensor cover glass to the sensor plane is 0.26mm [Fig 3.3]. This information is used in the Zemax prescription and tolerance analysis to ensure that the optical system is modeled as correctly as possible.

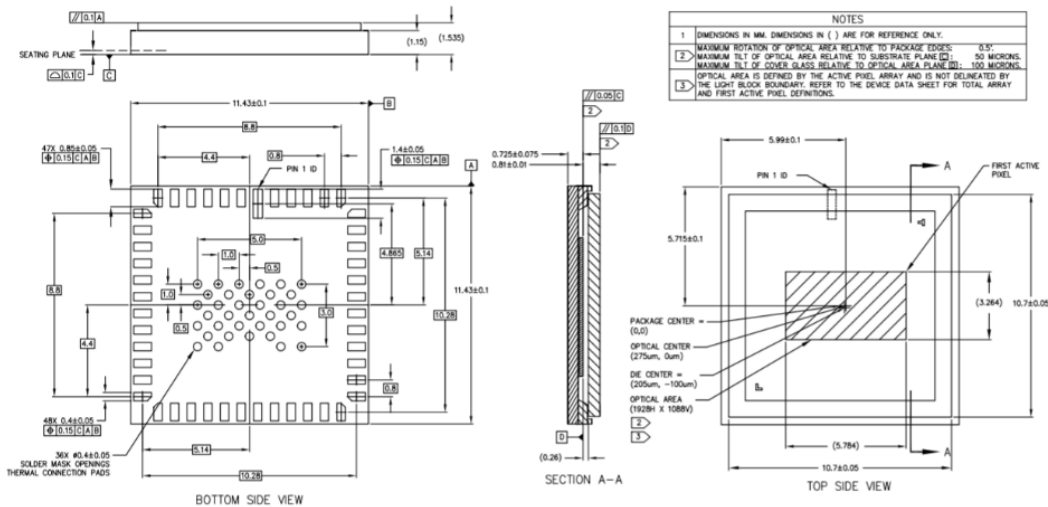


Figure 3.3. ON-Semiconductor AR0237 CMOS Sensor package dimensions

A sufficiently long back focal length is required to allow space between the lens barrel, image sensor package, and any other internal camera components which may be present. From this, the author has concluded that the minimum back focal distance for this lens system must be greater than the thickness of the sensor cover glass and the distance from the bottom of the cover glass to the image plane, which leads to a minimum back focal distance of 0.645mm. To allow for space for any optomechanical components on the lens barrel, the author has defined the minimum back focal length to be 1mm.

3.2.2 Image Circle Diameter

A unique property of fisheye lenses which are used for virtual reality is that the image circle must lie inside of the perimeter of the sensor via a circular fisheye lens. The centration tolerances between the optical axis and the center of the sensor must be considered in addition to the requirement of the image circle containing a full field of view of at least 190 degrees to stitch the two images together in the end. The sensor height of the AR0237 image sensor is 3.264mm; to ensure that there is always at least 190 degrees FOV inside of the image circle on the sensor while there are centration errors and tolerances between optical center and sensor's center, the lens must be designed to have a slightly smaller image circle than the 3.264mm sensor height. The author assumes that there will be a $\pm 50 \mu\text{m}$ centration tolerance between the optical center and the sensor's center. With this $\pm 50 \mu\text{m}$ tolerance, an image size of 3.164mm is required; Therefore, the folded fisheye lens will be designed to have an image circle semidiameter of 1.582mm at the full field of view of 190 degrees [Fig. 3.4].

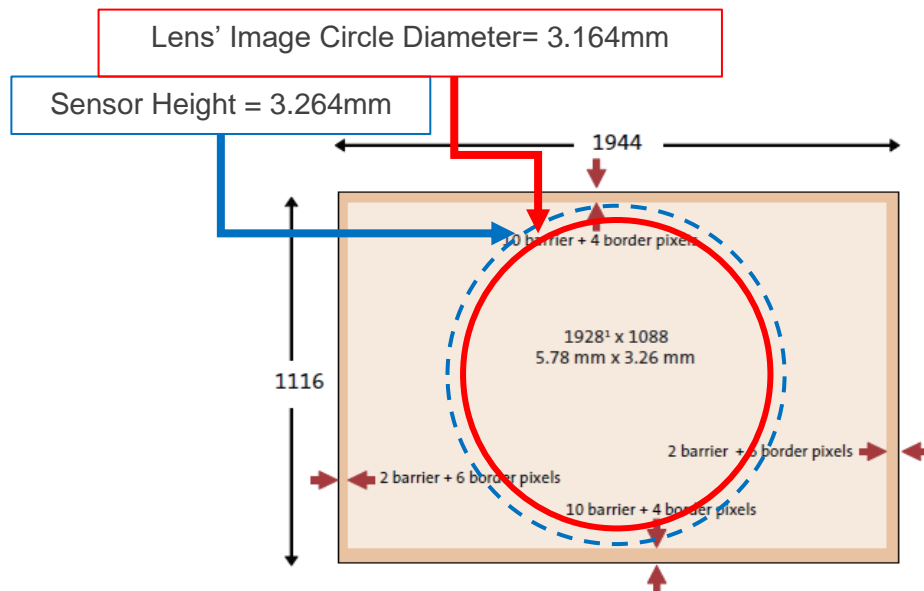


Figure 3.4. Image circle diameter set to be 3.164mm for the folded fisheye lens [23]

3.2.3 Chief Ray Angle

Digital image sensors are designed with an assumed chief ray angle, where a microlens array is placed on top of the sensor to maximize the light collection with this chief ray angle assumption. Some variation in this angle is allowed as long as it is less than the chief ray angle that the sensor was designed for [33]. Fig. 3.5 demonstrates the structure of a pixel in a classic CMOS sensor which uses a Bayer filter; If the incident angle of the ray is larger than the designed chief ray angle, the energy from that ray will not be fully collected in the photodiode and will cause a greater relative illumination falloff. In addition to the relative illumination falloff, the energy from the ray may pass through the barrier into the neighboring pixel causing chromatic cross talk.

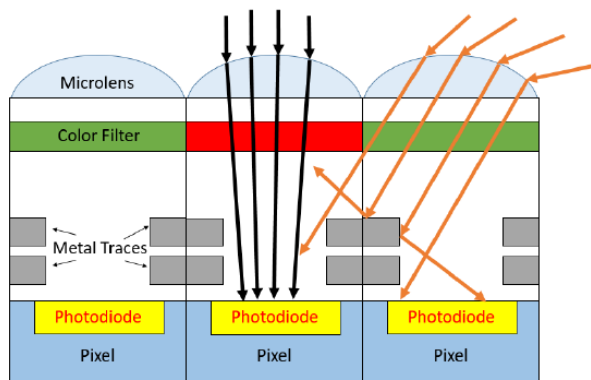


Figure 3.5. Pixel structure for common CMOS sensors [4]

The maximum chief ray angle of the ON-Semiconductor AR0237 CMOS image sensor is 12 degrees, meaning that the chief ray angle of the folded fisheye lens cannot exceed 12 degrees across the entire field of view. The chief ray angle in image space is often a function of the location of the aperture stop in the optical system; for example, if the stop is placed at the front focal point of the lens, the imaging system will be telecentric in image space. The closer that the stop is towards the front of the lens the smaller the chief ray angle will be, and the chief ray angle will increase as the stop is shifted towards the back of the assembly. Thus, this chief ray angle requirement of 12 degrees will likely determine the stop location in the lens.

3.4 MTF Requirement

The modulation transfer function, or MTF, is defined as the modulus of the optical transfer function and relates to the resolution of an imaging system. It can be thought of as a measure of how well an imaging lens transfers contrast from an object to the image [34]. MTF has units in contrast per the spatial frequency of the image in cycles per millimeter.

$$\text{Contrast} = \frac{I_{max} - I_{min}}{I_{max} + I_{min}} \quad (3.1)$$

In a perfect imaging system, the MTF would be unity for all spatial frequencies; however, in a real image the contrast is reduced due to diffraction limited airy disk spot diameters and optical aberrations in the system. Fig. 3.6 demonstrates the contrast reduction between an object and image as a function of increasing spatial frequency, where the MTF of that transfer function is then derived.

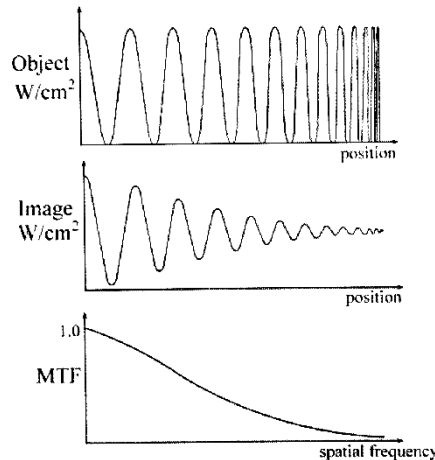


Figure 3.6. Modulation Transfer Function (MTF) [35]

Astigmatism, field curvature, chromatic aberration, and other optical aberrations will cause the sagittal and tangential rays to exhibit different MTF values. Generally, the MTF is reported for both the sagittal and tangential field lines in addition to the diffraction limited MTF for that F-number; the MTF is reported for several field points and is plotted as a function of spatial

frequency up until the Nyquist frequency of the system. Fig. 3.7 demonstrates an example MTF plot on the left, with subjective images of how a pair of bar targets would appear for the sagittal and tangential rays at a spatial frequency near 20cy/mm on the right.

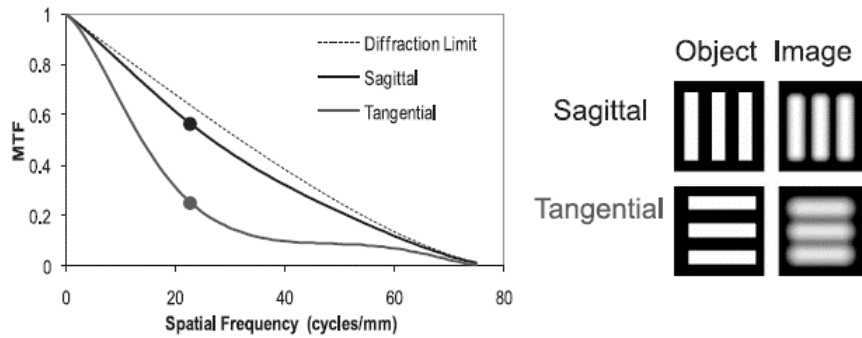


Figure 3.7. Modulation Transfer Function example [34]

Subjectively, the contrast reduction at higher spatial frequencies will cause the image of smaller objects to appear blurred. Fig. 3.8 demonstrates the difference in MTF between a lens which exhibits high MTF versus a lens with lower MTF. As shown, the image of the bar targets appears more blurred for the lens with low MTF. Thus, to obtain a sharp image as is required for camera applications, high MTF is preferred.

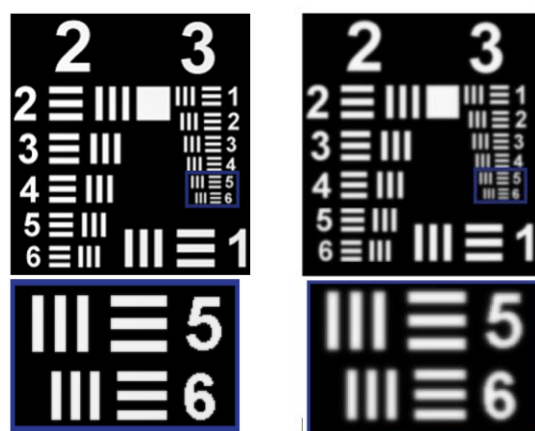


Figure 3.8. Demonstrating the contrast and image quality reduction from MTF between (a) a lens with high MTF and (b) a lens with lower MTF [36]

MTF is the magnitude of the complex optical transfer function (OTF), where the optical transfer function is the Fourier transform of the point spread function. Lenses with optical aberrations may exhibit a negative OTF, which represents what is called a phase or contrast reversal or light and dark features [35]. In the presence of an object showing line pairs, the bright lines will become dark and the dark lines will become bright [Fig. 3.9]. Because the MTF is the magnitude of the OTF, it is always reported as a positive value; in the presence of a phase reversal, the MTF will appear to ‘bounce’ off of the optical axis.

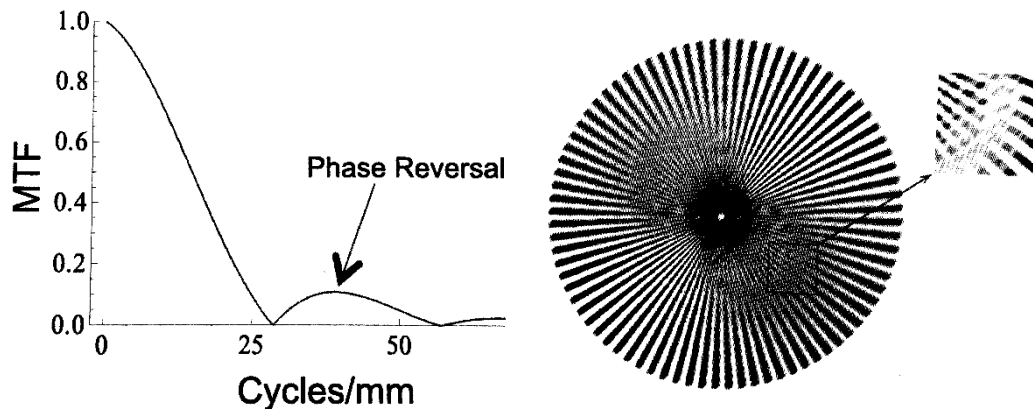


Figure 3.9. MTF plot and photo representation of phase reversal [34][35]

For digital image sensors, the pixel size of the sensor which is used with an imaging lens defines the Nyquist frequency, and thus what the MTF requirements of that lens must be [25]. The Shannon Sampling Theorem requires a minimum of two samples per cycle to perfectly reconstruct a sampled signal and the Nyquist frequency limit defines the maximum frequency at which features can be sampled. Nyquist corresponds to one full white-dark line pair cycle spanning two pixels. Therefore, the highest spatial frequency that can be detected equals the reciprocal of twice the pixel pitch of the image sensor [34]. This frequency is represented as

$$f_{Nyquist} = \frac{1}{2 * Pixel\ Pitch}. \quad (3.2)$$

With the $3\mu\text{m}$ pixel pitch of the AR0237 image sensor, the Nyquist frequency of the ON-Semiconductor AR0237 CMOS image sensor is calculated to be

$$f_{Nyquist} = \frac{1}{2*3\mu\text{m}} \cong 167 \frac{\text{cy}}{\text{mm}}. \quad (3.3)$$

The AR0237's Nyquist frequency of 167lp/mm defines the maximum resolution that the folded fisheye lens design must achieve. For digital imaging systems, the minimum contrast requirement of the lens is typically 30% MTF at Nyquist of the image sensor [25]. From this, the author has defined a minimum MTF requirement of 30% at 167lp/mm in the final system with manufacturing tolerances.

3.5 Lateral Color Aberration Requirement

Lateral color is an off-axis chromatic aberration that can contribute to a reduction in MTF of an image, which increases as the field height increases [25]. Lateral color refers to a chromatic change in chief ray height at the image plane referenced from the d (587nm) wavelength; this occurs due to refractive index differences for each wavelength, which causes the chief ray height to experience a lateral shift across the image as a function of wavelength. To maintain sharp image quality across the field, lateral color aberration must be tightly controlled. Fig. 3.10 demonstrates this shift as a function of wavelength, where the lateral color creates a spot offset for each color.

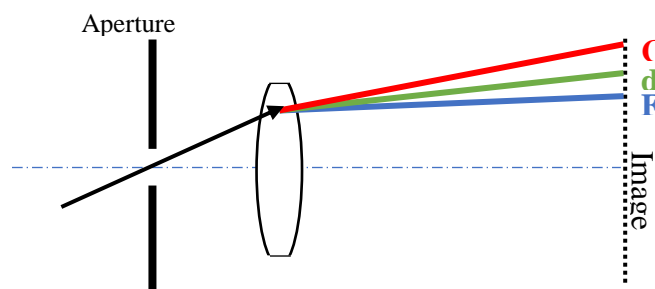


Figure 3.10 Illustration of lateral chromatic aberration of the Chief Ray for F (486nm), d (587nm), and C (656nm) wavelengths.

In addition to the sensor characteristics and pixel size defining the MTF requirements, they also define the allowable chromatic aberration in a lens system. There are 2 pixels that the chief ray must translate before it falls into a Bayer filter which will transmit the same color [Fig. 3.11]. Thus, a lateral chromatic aberration of less than 2 pixels, or $6\mu\text{m}$ when using the AR0237 CMOS sensor, will not be detected by the sensor. From this, the maximum allowable lateral chromatic aberration requirement for the folded fisheye lens is $6\mu\text{m}$.

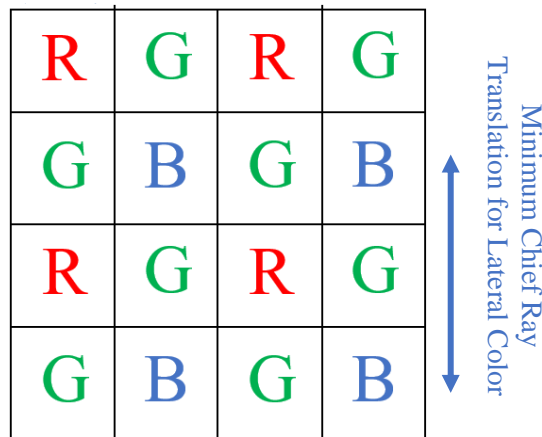


Figure 3.11. Lateral Color shift must be greater than two pixels to be detectable in the RGGB Bayer array format used in the AR0237 CMOS sensor.

A common method to achromatize a lens system is to first design the system for a single wavelength, and utilize a buried surface in an achromat to correct for chromatic aberration in the end. When doing this, it is most useful to choose glass types with similar refractive indices with large differences in Abbe numbers. Keeping the refractive index the same between both halves of the doublet ensures that the monochromatic aberrations are unaffected after color is introduced, while allowing the lens designer to vary the radius of curvature of the inner surface to correct for chromatic aberrations. With this method, a lens designer can achieve decent polychromatic performance, where the glass types of the doublet can then be substituted and reoptimized for better chromatic performance if needed.

Historically, it has been shown that an achromatic doublet placed behind the aperture stop can be used to efficiently correct lateral color in fisheye lens systems. M. Laikin's paper, "Wide Angle Lens Systems" [37] demonstrates the ability to utilize achromats on either side of the stop to reduce lateral color, while making note that achromats placed before the aperture stop are less effective. Many times, a single achromat placed behind the stop does not sufficiently correct the lateral color, and thus most modern fisheye lenses often utilize a negative achromat placed before the aperture stop.

3.6 Relative Illumination

Ordinary photographic imaging lenses with little to no distortion obey the $\cos^4\theta$ law of relative illumination fall off as a function of chief ray height, $E = E_0 \cdot \cos^4 \theta$, as was discussed in Chapter 2.5. Using the Eq. 2.6 shows that the image space chief ray must be less than 33 degrees to maintain a 50% relative illumination across the field in theory. However, as was also discussed in Chapter 2.5, fisheye lenses are able to defy the $\cos^4\theta$ law via the Slyusarev Effect [29] where large amounts of distortion and pupil aberration cause a change of entrance pupil location and diameter as a function of field height; this pupil aberration allows for the illumination at the edge of the field to be larger than the illumination in the center.

Digital image sensors use image signal processing to correct for relative illumination by applying a radial gain to the image; Because this can be corrected [4], photographic lenses tend to have more relaxed requirements for relative illumination. A common relative illumination specification for wide field of view photographic lenses is 50% [34], and common photographic fisheye lenses are shown to have relative illuminations ranging from 50% to 70% [31]. Thus, the author has set a 50% minimum relative illumination as the specification for this optical design, which should be easily achievable.

3.7 Wavelength Weighting Definition

It is important to match the wavelength weighting that is used to design the lens to the real-world application of the optical system. The responsivity of the sensor's silicon in addition to the Bayer filter transmissivity, the UV/IR-cut used, and the spectrum used to test the optical system will all play a factor in the wavelength weighting that is used while designing this lens. Fig. 3.12 shows the quantum efficiency of the AR0237 CMOS sensor and Bayer filter which is used [23].

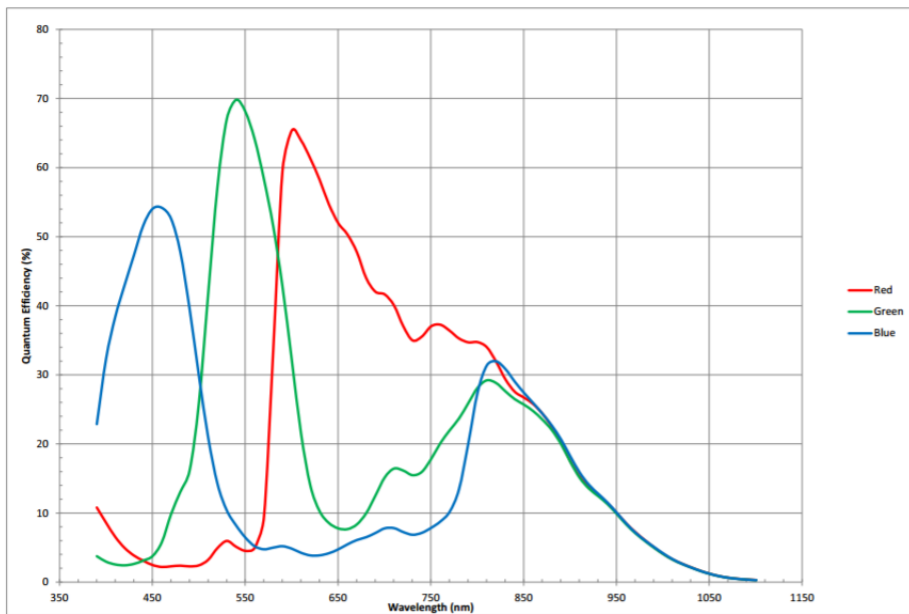


Figure 3.12. Quantum Efficiency of the ON-Semiconductor AR0237 CMOS image sensor

As shown, the quantum efficiency is relatively high in the ultraviolet and infrared regions which indicates that this optical system will require an optical filter to prevent UV and IR radiation from making it to the image sensor. A broadband-pass filter specifically designed to cut out the UV and IR radiation from the imaging system are commonly used, which are often referred to as a UV/IR-cut filter [27]. These filters transmit ~100% of the radiation between 450nm and 650nm, while transmitting ~0% of the radiation below 450nm and above 650nm.

The UV/IR-cut filter can either be coated onto a flat surface, such as the sensor cover glass or an added optical window to the system, or it can be coated on top of an optical element inside of the system. For stray light purposes, it is usually advantageous to have the UV/IR-cut coated on an element surface inside of the optical system. This option will be kept open during the design, and the final location of the UV/IR-cut filter is chosen by performing a stray light and ghost analysis of the lens design in the non-sequential optical design software FRED in Chapter 5.

Common UV/IR-cut filters cut on around 450nm and cut off around 650nm. For this design, the author referenced standard off-the-shelf UV/IR-cut filters to use as a reference [28]. The UV and IR-cut filters which were chosen as a reference from Edmund Optics can be seen in Fig. 3.13. The UV cut-on filter has less than 0.1% transmission for wavelengths below 450 nm, and transitions to approximately 95% transmission from 450nm +/- 2nm to 650nm. The infrared cut-off filter chosen has greater than approximately 95% transmission from 450nm to 650nm +/- 2nm, where wavelengths greater than 650nm has less than 0.1% transmission.

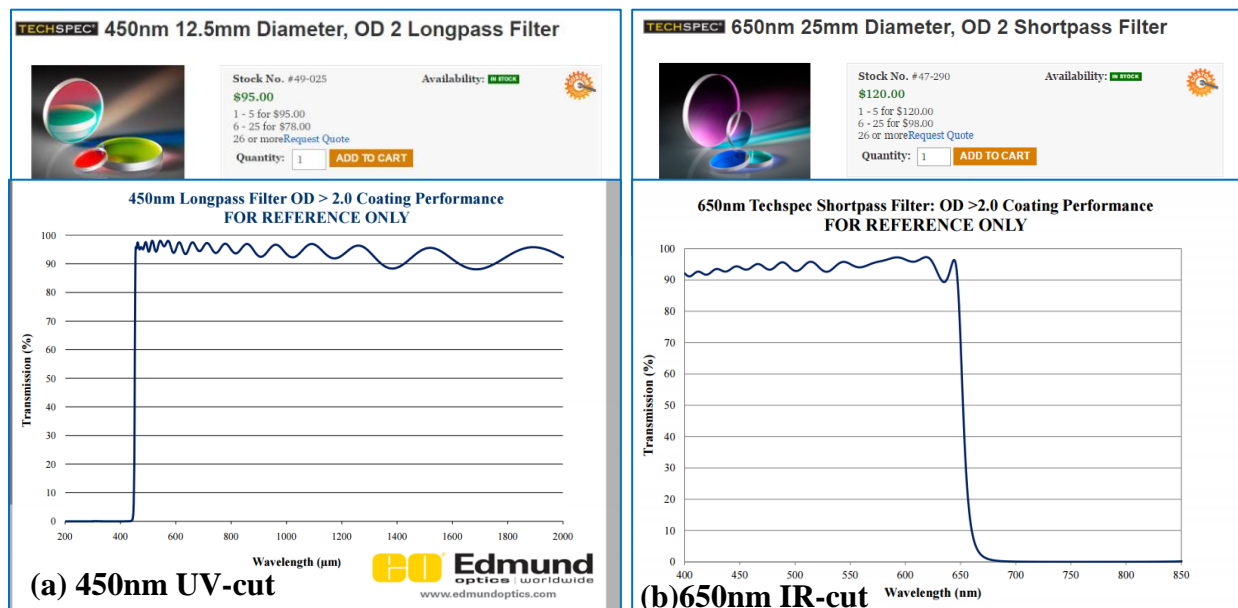


Figure 3.13. Transmission versus wavelength plots for (a) UV-Cut Filter and (b) IR-Cut Filter [28]

How this lens is tested will also need to be represented in the wavelength weighting that is used. There are many potential ways for this optical system to be tested; for consumer electronic cameras like the virtual reality camera that this lens is intended for, lenses must be tested at a very fast rate. A few potential testing methods which would satisfy this condition are professional MTF test stations, reverse-projection with a bar target image, or a slant-edge MTF analysis of the combined lens and sensor module.

With the application of this lens being a consumer-focused camera, this lens would likely be manufactured at a fast rate in large quantities; MTF test stations for compact imaging modules which are used in mass production environments, like the Trioptics ImageMaster Pro, commonly use the Photopic Eye spectrum when measuring MTF [38]. Thus, the author has assumed that the lens will be tested using the Photopic eye spectrum.

A plot of the spectra which this lens will be exposed to are shown in Fig. 3.14, including the quantum efficiency of the red, green, and blue pixels on the AR0237 image sensor, the Photopic eye testing spectrum, and the UV/IR-cut filters.

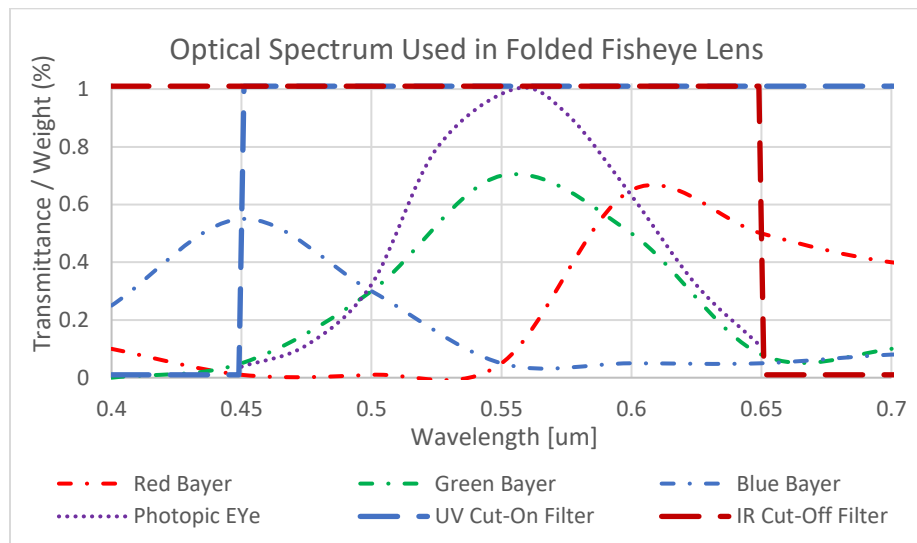


Figure 3.14. Optical spectra which the folded fisheye lens must operate with, including the quantum efficiency of the AR0237 sensor, Photopic eye test spectrum, and UV/IR filter

Lastly, an average is taken of the quantum efficiency of the AR023 CMOS image sensor, UV and IR-cut off filters, and the Photopic eye testing spectrum, to determine the wavelength weighting which will be used while designing the folded fisheye lens in Zemax. The black dotted line shows the weighted average between all wavelengths, and the solid black line is the normalized average of all of the wavelengths [Fig. 3.15]. This normalized average is the wavelength weighting which the author used while designing the folded fisheye lens, to ensure that the lens performs well for all use-case applications that it will be exposed to.

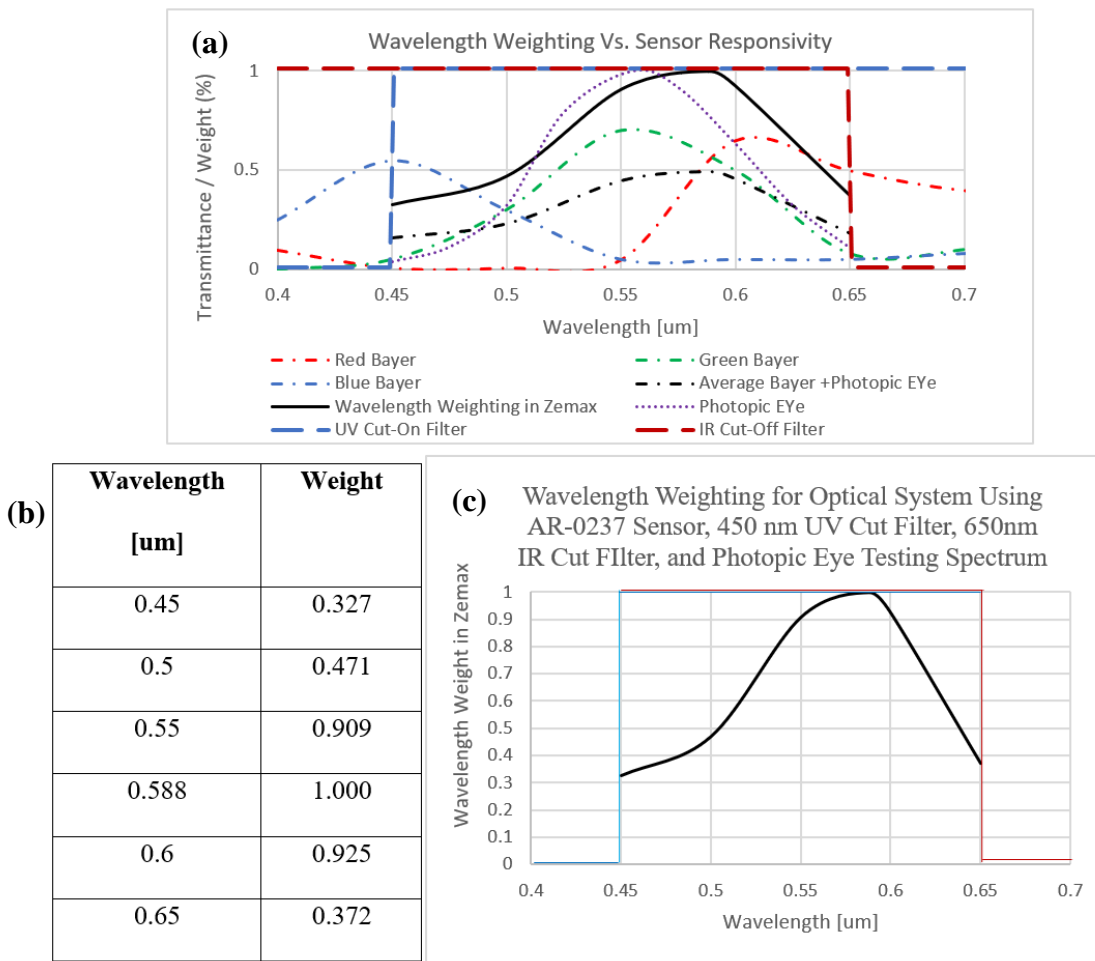


Figure 3.15. (a) All optical spectra that the lens will be used with, along with a weighted average and the wavelength weighting used in Zemax, (b) Wavelength weighting values and (c) plot of wavelength weighting values used in the design of the folded fisheye lens

3.8 Manufacturability and Cost

During the optimization of the folded fisheye lens, it is important to keep manufacturability in mind throughout the entire process. The center thickness to diameter ratio of lens elements must always be large enough to be fabricated reliably, and the distance between lens elements and the edges of each element must be long enough that the elements do not collide. The way that each lens might be assembled into a barrel must be considered, where mechanical mounting features may be ground into the optical elements to aid in achieving tighter tolerances [Fig. 3.16] [25]. Because the final optical design uses a molded glass prism which is expected to be very expensive, the author has chosen to limit all other optical surfaces in the design to be spherical glass elements which are known to be cheap. In addition, a requirement of less than 10 total elements must be used in the design to ensure low cost while also ensuring that the total track length is minimal.

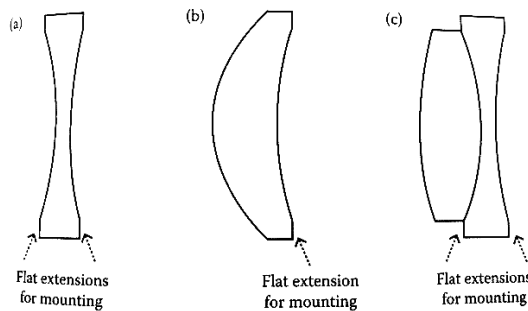


Figure 3.16. Mounting flanges on various lens element shapes to aid in assembly [25]

Tolerancing with small optical elements can often be challenging; in these cases, combining two elements which are especially sensitive to the optical tolerances into one doublet lens can help desensitize the effect of those tolerances on the overall performance of the lens assembly and increase the manufacturing yield. A system with high manufacturing yields can decrease the cost of the total system. Lastly, common glass types must be used. For the folded fisheye lens, the author aims to achieve greater than 90% yield when using commercial manufacturing tolerances with a 30% minimum MTF specification at 167lp/mm.

3.9 Optical Design Requirement Summary

A summary of the first-order requirements which have been defined in this Chapter is shown in Table 3.1, with a list of all optical performance requirements listed in Table 3.2.

Merit	Specification
Image Sensor	ON-Semiconductor AR0237 CMOS Sensor (3um pixel size)
Image Circle Half-Diagonal (mm)	1.582mm (+/- 50um tolerance on AR0237 Sensor Vertical)
FOV	>190 degrees
F#	<=2.8
Vertex-to-Vertex Thickness of 2-Lens Module	<30mm
Sensor-to-Sensor Width of 2-Lens Module	< 75mm
Number of Elements	<10. All Spherical
Optical Folding Mechanism	Moldable Glass Prism
Sensor Cover Glass Thickness	0.385mm, Made of N-BK7
CG to Sensor Distance	0.26mm
BFL	>= 1mm
Glass Types	Schott, Ohara, Hoya, CDGM Only
Yield	>90%

Table 3.1. First-Order Specifications for Folded Fisheye Lens

Merit	Specification
Wavelength Range (um)	450nm to 650nm, Custom Wavelength Weighting
MTF	>30% MTF at 167lp/mm
Lateral Chromatic Aberration	< 6um
Chief Ray Angle @ 100% IH	<12 Degrees
Relative Illumination	>50%

Table 3.2. Optical Performance Requirements for Folded Fisheye Lens

4 COMPACT FOLDED FISHEYE LENS DESIGN

The unique properties of fisheye lenses and the requirements that a compact fisheye lens must meet when used with the ON-Semiconductor AR0237 CMOS sensor have been described in Chapters 1 through 3. In this chapter, a new circular fisheye lens is designed for a compact virtual reality camera application, where the author has utilized a powered prism to fold the optical system with the primary goal being to minimize the vertex-to-vertex distance between the two fisheye lens modules in a potential camera. The design considerations, optical performance, and the overall performance of the two-lens system are presented and analyzed in detail.

4.1 Prior Art and Starting Point Design

A fisheye lens history was presented in Chapter 1 and the general fisheye lens structure was discussed in Chapter 2.2. While sufficient information exists about standard fisheye lenses, documentation about fisheye lenses which are folded via a prism is much more difficult to acquire. Fortunately, a sufficient amount of documentation regarding folded zoom lenses which are intended to be used in compact applications is available; Although they do not have fields of view greater than 180 degrees, D. Reiley's paper, "Folded zoom lenses – a review of patent literature" presents a handful of folded zoom lenses which utilize negative meniscus lens elements in front of the prism [39] similar to fisheye lenses. Taking inspiration from the designs presented in Fig. 4.1, the author chose to place the prism immediately after the first lens negative meniscus lens element in the system to maintain a compact form factor while allowing the design to capture a large field of view. Due to the large field of view of fisheye lenses, the glass material of the prism must be chosen such that light from all fields will experience total internal reflection in the prism. The rest of the folded fisheye lens will follow the general fisheye lens structure, where the author has limited the design to using only spherical glass elements for cost and manufacturability reasons.

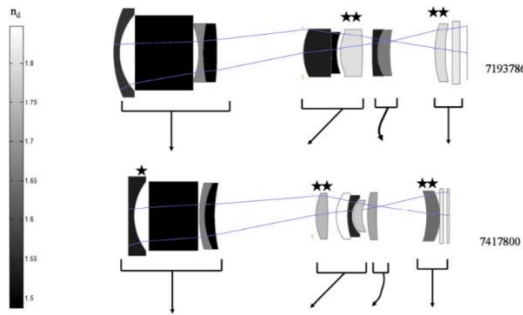


Figure 4.1. Schematic of two U.S. patents for compact folded zoom lenses. The systems are shown ‘unfolded’ with the prism represented as a thick plane parallel element [39]

US Patent 7,023,628, “Compact Fisheye Objective Lens” invented by A. Ning in 2006 [40], was used as the starting point for this optical design as it contains many of the qualities that the author is looking for in the final design. US 7,023,628 uses six spherical glass elements to obtain a full field of view of 180 degrees with a total track length of 21mm, while maintaining good polychromatic optical performance across the field at a maximum aperture of F/2.8 [Fig.4.2]. This lens uses two negative meniscus lenses at the front of the optical assembly and an achromatic doublet placed after the aperture stop, giving it the standard form of a fisheye lens as discussed in Chapter 2.2. The optical prescription is shown in Fig. 4.3. Upon converting the optical prescription into a Zemax file and scaling the lens to meet the image size requirement, the author noted that the lateral color and relative illumination of this patent meet the design specification, while the MTF and chief ray angle do not meet the design requirements.

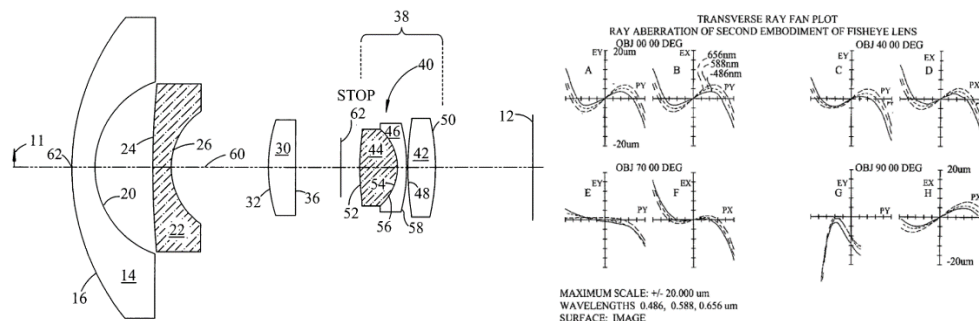


Figure 4.2. Lens schematic and performance of patent US 7,023,628 [40]

Focal length $f_o = 1.68$, Total track TT = 20.2
TT/fo = 12, Full field of view = 180 deg, F/# = 2.0

Sur f	Comment	Radius	Thickness	Index at 588 nm	Abbe Number
OBJ		Infinity	Infinity		
1	(14) (16) LENS 1	9.99	1.00	1.910	35.47
2	(14) (20)	4.15	1.98		
3	(22) (24) LENS 2	17.42	0.80	1.816	46.61
4	(22). . .(26)	3.07	5.32		
5	(30) (32) LENS 3	6.26	1.14	1.917	21.51
6	(30) (36)	39.78	1.56		
7		Infinity	0.62		
8	LENS 4 Doublet (44)(52)	9.81	1.82	1.729	54.67
9	(44) (54) LENS 5	-2.20	0.40	1.917	21.51
10	(46) (58)	-6.95	0.06		
11	Singlet (42) (48) LENS 6	45.11	1.03	1.640	60.15
12	(42) (50)	-10.04	3.50		
13	Sensor cover glass	Infinity	0.40	1.516	64.17
14		Infinity	0.55		
IMA		Infinity			

Figure 4.3. Optical prescription of patent US 7,023,628 [40]

To take the optical design from this patent to the final folded fisheye lens, the author must first fold the optical system, and improve upon the MTF while reducing the chief ray angle all while meeting the package and optical requirements outlined in Chapter 3.9.

4.2 Prism Considerations

Placing powered surfaces onto a right-angle prism will add manufacturing challenges with the added benefit of being able to remove the second negative meniscus lens which is used in fisheye lens designs to make the system as compact as possible. The author believes that this element could be fabricated by cementing negative plano-concave lenses onto the prism, utilizing a post-processing lapping and polishing method on a pre-fabricated prism to add concave surfaces, diamond turning procedures, or using precision glass molding. For the high manufacturing quantities generally associated with consumer electronics, the author has assumed that molding this component would be the cheapest option, and thus has chosen to use a high index moldable glass type for the powered prism element. To ensure that the element could be fabricated with another method in the case that precision glass molding is impractical, the surfaces are limited to being spherical surfaces in the optical design.

A high index prism is beneficial for many reasons. A higher index minimizes the optical path length through the glass and can allow for a smaller prism to be used as compared to a lower index glass [39]; in addition, the powered surfaces which are placed on the prism can have lower curvature compared to if a low index was used, which can decrease the sensitivity to tolerances in manufacturing. Lastly, a high index increases the chance for total internal reflection to occur within the prism across the high field heights.

The critical angle which defines total internal reflection is proportional to the prism index, defined by

$$\theta_{critical} = \sin^{-1} \left(\frac{n_2}{n_1} \right). \quad (6.1)$$

In air, $n_2 = 1$, and the critical angle becomes

$$\theta_{critical} = \sin^{-1} \left(\frac{1}{n_{prism}} \right). \quad (6.2)$$

Using Eq. 6.2, a table of critical angle versus the prism index is presented in Table 4.1. Rays which have an incident angle greater than the critical angle will experience total internal reflection.

Prism Index	Critical Angle
1.4	45.58
1.5	41.81
1.6	38.68
1.7	36.03
1.8	33.75
1.9	31.76
2	30

Table 4.1. Critical Angle versus Prism Index

A prism with an index of 2 requires the incident angle on the prism face to be greater than 30 degrees for TIR to occur, where an index of 1.4 requires the angle to be greater than 45 degrees. Thus, the author has chosen to use a high index moldable glass type to increase the opportunity for TIR to occur in the prism across the large field angles that exist in a fisheye lens. Because the prism uses powered surfaces, the author has assumed that the prism will be a molded optical element via precision glass molding to minimize the cost associated with this element. Ohara's low softening temperature glass types are specifically developed for precision glass molding (PGM) applications. Out of the list of available low softening temperature glasses, L-LAH86 is shown to have the highest refractive index while exhibiting a low glass transition temperature [Fig 4.4][42]. The glass type L-LAH86 from Ohara was chosen for the prism material, and has the properties shown in Table 4.2. With a refractive index of 1.9027, a prism made of L-LAH86 as a critical angle of 31.71 degrees. This glass has a relative cost of 3.3.

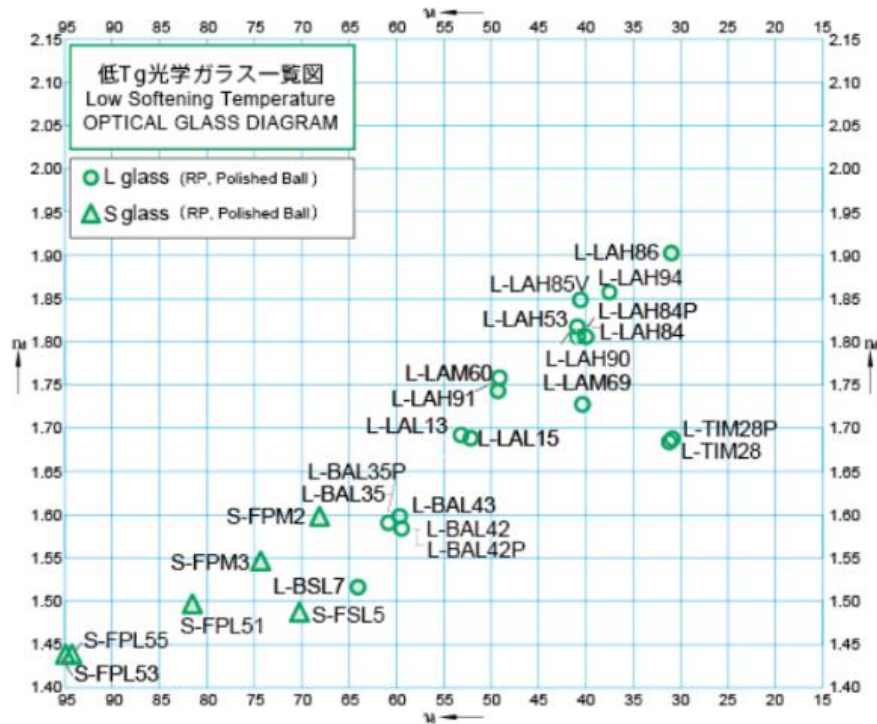


Figure 4.4. Ohara low softening temperature optical glass types intended for PGM [42]

Refractive Index, n_d	1.9027
Abbe Number, V_d	31.00
Glass Transition Temperature, T_g	578°C
Coefficient of Thermal Expansion (ppm/°C)	6.1

Table 4.2. Ohara L-LAH86 glass properties [41]

4.3 Glass Material Choices

Each of the glasses which are used in the patent design can be found in the Schott catalogue.

To ensure that the lens is manufacturable at a low cost, the author has limited the glass catalogues to Schott, Ohara, Hoya, and CDGM, with a preference on glass types with low relative cost. For Schott glasses, the cost is given relative to the cost of N-BK7, where Ohara's relative cost is given

in relation to N-BSL7 glass. Glass manufacturers commonly sort their optical glasses into four categories, including preferred, standard, obsolete, and special.

Preferred glasses are commonly used glass types, and manufacturers will often have these glass types manufactured in large quantities resulting in a lower price. These glass types should be used if possible. Standard glass types are also commonly utilized in lens designs and are readily available but may cost more than preferred glasses.

Obsolete and special glass types are avoided in the optical design. As noted by the name, obsolete glass types are no longer manufactured and may be difficult to acquire; these glass types are still included in the design program primarily so that older designs can still be evaluated but will often times be omitted during the optimization process. Special glass types are also hard to obtain in manufacturing and will have high cost associated with them.

For a consumer device, it is important for the outermost or exposed elements to be able to withstand harsh environments. In general, LaK and LaSF glasses have the highest Knoop hardness [43], meaning that they have a higher resistance to scratches and abrasion. Because of this, the author chose Schott glass type N-LASF46A with a Knoop Hardness of 666 for the first lens element to ensure that the final camera is scratch resistant. The relative cost of N-LASF46A is 6 which makes it the most expensive glass type used in this design. The image sensors which are used in compact cameras can create a lot of heat, which can cause a degradation in image quality as the camera heats up [25]. Because of this, the author has chosen a low CTE glass type of N-LAK34 for the element which is closest to the image sensor.

The three most expensive glass types each have a specific utility in the optical design. The most expensive glass, N-LASF46A has a high Knoop hardness to ensure that the camera is durable and scratch resistant. The second most expensive glass, N-LAK34, has the lowest coefficient of

thermal expansion, and is placed nearest to the image sensor to minimize thermal effects. S-FPL53 is the third most expensive glass used in the design; this glass has similar properties to CaF₂ with a very low index and high Abbe number, along with a high partial dispersion which makes this glass type useful for correcting secondary chromatic aberration in the system.

A table of each glass which was used in the optical design is shown in Table 4.3, along with data of the refractive index, abbe number, catalogue, relative cost, and any notes about why that material was chosen. All of the glass types used in the folded fisheye lens design are preferred except for L-LAH86 which is used for the molded glass prism.

Glass Name	Catalogue	n_d	V_d	Relative Cost	Status	Notes
N-LASF46A	Schott	1.9037	31.32	6	Preferred	High Knoop Hardness for Durability
L-LAH86	Ohara	1.9027	31.00	3.3	Standard	Low T _g , Used for Molded Prism
P-SF67	Schott	1.9068	21.40	2.5	Preferred	
S-LAH51	Ohara	1.7859	44.20	1.4	Preferred	
N-FK5	Schott	1.4875	70.42	2.0	Preferred	
S-FPL53	Ohara	1.4388	94.95	4.9	Preferred	Useful for secondary color correction
N-LAK34	Schott	1.7292	54.50	5.5	Preferred	Low CTE (5.81ppm/C)
N-BK7	Schott	1.5168	64.15	1.0	Preferred	Sensor Cover Glass

Table 4.3. Glass types used in the folded fisheye lens design

4.4 Optical Design

The author presents a new compact folded fisheye lens design with a focal length of 1.297mm at an aperture of F/2.8 which can capture a full 190-degree field of view on a 1/2.7" image sensor. This lens design uses eight spherical glass elements in six groups [Fig. 4.5], along with a powered prism to meet the optical requirements defined in Chapter 3. The moldable powered glass prism which is used to fold the optical path is a 6mm x 6mm right angle prism, with 25mm radii concave surfaces placed on the entrance and exit faces of the prism. The vertex-to-vertex thickness of the two-lens system is 24.94mm; assuming a 50 μ m gap between the two prisms, the vertex-to-vertex thickness is 25mm with a sensor-to-sensor width of 56mm [Fig. 4.6].

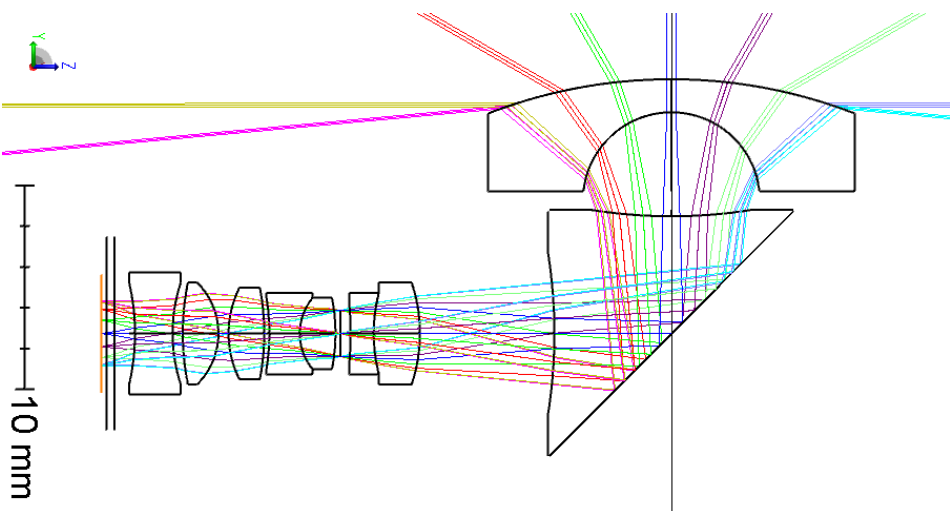


Figure 4.5. 2D Layout of Compact Folded Fisheye Lens Design

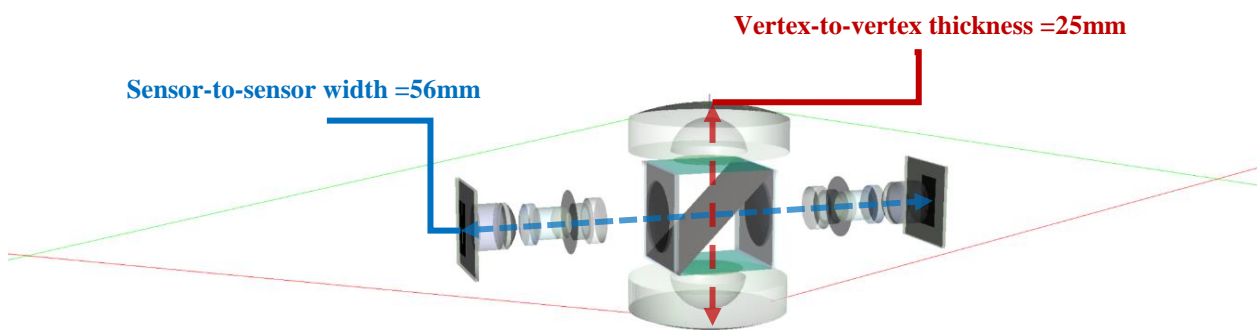


Figure 4.6. 3D Layout of Compact Two-Lens System Using Folded Fisheye Lens Design

The optical design process for the folded fisheye lens began by first increasing the thickness of the second negative meniscus lens element in US patent 7,023,628 to be 12mm thick, while optimizing the lens with constraints in the merit function on total track length, chief ray angle, back focal length, maximum image height, and glass and airgap thicknesses. With the prism inserted into the design, coordinate break surfaces were utilized to fold the optical system in the powered prism. To ensure that the prism can be manufactured with a variety of fabrication methods, the surfaces are set to be negative 25mm concave spherical surfaces.

The achromatic doublet and the positive glass element which lie behind the stop in US 7,023,628 [Fig. 4.2] were kept during the optimization process, while the positive element just before the stop was turned into an achromatic doublet to aid in lateral color correction. In addition, an S-FPL53 element is placed near the end of the assembly to control secondary color aberration, as the ray bundle width is relatively large in this region and chromatic aberration is proportional to the square of the clear aperture [29]. Lastly, a negative element was placed at the very end of the optical assembly to control field curvature. The aperture stop is placed in the center of the optical system with a slight asymmetry in the number of optical surfaces on each side of the stop to meet low chief ray angle requirement of 12 degrees as discussed in Chapter 3.2.3.

The radii of curvature of the first lens element maintains high relative illumination by reducing the Fresnel reflections with lower incident angles at the higher field heights, while allowing the lens to capture the 190-degree full field of view. The negative powered surfaces on the prism also reduce the field angle into the rest of the system. The back focal distance of the folded fisheye lens is 1.645mm, with a 1mm distance between the last lens element and the top of the sensor cover glass. Due to the concave shape of the last lens element, the mechanical flange distance between the edge of the final lens element and the sensor cover glass is 0.712mm.

Manufacturability was kept in mind throughout the entirety of the design; all elements have reasonable center thickness, edge thickness, clear aperture diameters, and reasonable airgap spacings set between each element to avoid collisions or issues in assembly. As seen in the prescription data [Table 4.4], many of the glass and airgap thicknesses were rounded off to integer values, with some radii constrained to even numbers when possible. Mechanical clear aperture and element semidiameters are all set to integer values to simplify the manufacturing requirements, and each lens is set to have sufficient semidiameter margin to allow each element to be assembled into a barrel without vignetting. As shown in Fig. 4.7, the elements near the stop have the smallest diameters, and the diameter increases as the distance from the stop is increased. This ensures that the lenses can be assembled into a barrel, where the elements near the stop would be placed in first, and each element is stacked out away from the aperture.

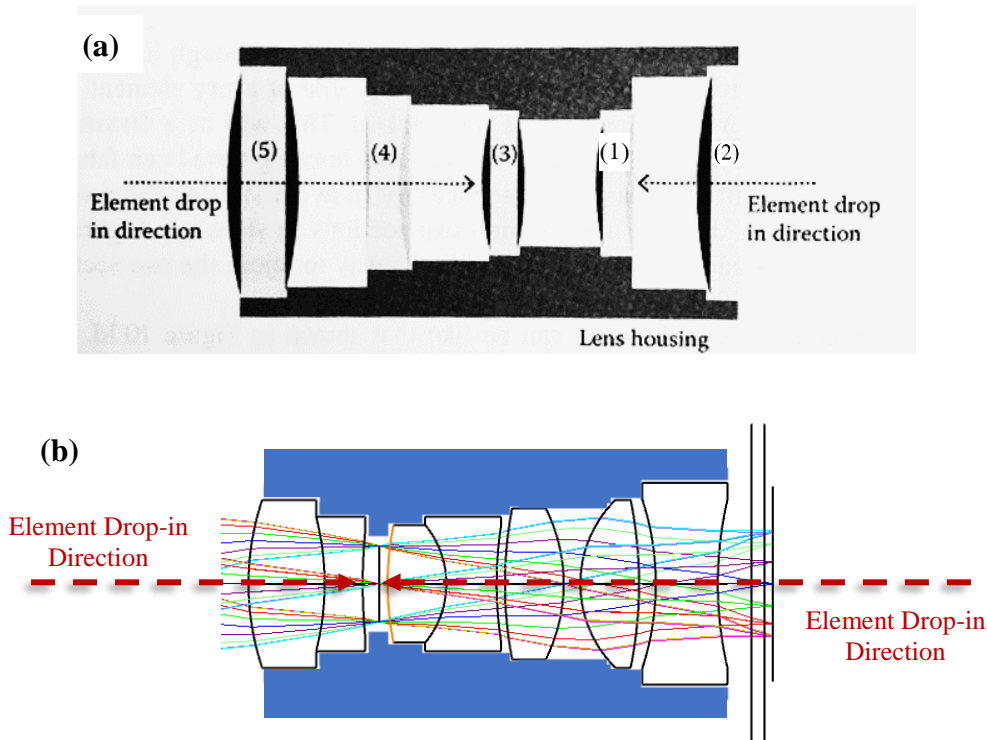


Figure 4.7. (a) Illustration of element size affecting mounting process and procedure [25],
(b) Element size chosen for easy loading procedure in manufacturing the folded fisheye lens

4.4.1 Optical Prescription Data

The compact folded fisheye lens was designed using Zemax OpticStudio 16, where coordinate break surfaces were utilized to fold the optical system in the powered prism. The coordinate breaks create complications when modeling the powered surfaces on the prism; thus, the prism was modeled with planar surfaces with thin plano-concave elements with the same material placed in contact on the entrance and exit faces. After a reflection occurs via the prism used in Zemax the sign of the radii of curvature and thicknesses are made negative. The optical prescription for the folded fisheye lens is presented in Table 4.4, with all units in millimeters.

Surface Number	Radius	Thickness	Material Name	Nd	Vd	Clear Aperture	Mechanical Diameter
1	25.000	1.621	N-LASF46A	1.9037	31.32	9.000	9.000
2	4.360	5.097				4.333	9.000
3	-25.000	0.250	L-LAH86	1.9027	31.00	4.000	6.000
4	Infinity	5.500	L-LAH86	1.9027	31.00	4.000	-
5	-	0	Coordinate Break Surface: Tilt About X = -45				
6	Infinity	0	MIRROR			8.500	-
7	-	-5.500	Coordinate Break Surface: Tilt About X = +45				
8	Infinity	-0.250	L-LAH86	1.9027	31.00	4.000	-
9	-25.000	-6.608				4.000	6.000
10	-7.838	-2.271	P-SF67	1.9068	21.40	2.500	2.500
11	7.944	-1.135	S-LAH51	1.7859	44.20	2.000	2.000
12	-16.697	-0.495	-	-	-	1.500	2.000
13	Infinity (STOP)	-0.250	-	-	-	1.125	1.125
14	-8.964	-1.750	N-LAK34	1.7292	54.50	1.750	1.750
15	2.750	-1.500	P-SF67	1.9068	21.40	1.750	1.750
16	-11.186	-0.250				1.750	2.000
17	-11.914	-1.750	N-FK5	1.4875	70.72	2.250	2.250
18	5.000	-0.500				2.250	2.250
19	-3.500	-1.750	S-FPL53	1.4388	94.95	2.500	2.500
20	12.555	-0.500				2.500	2.500
21	8.000	-1.850	N-LAK34	1.7292	54.50	2.500	3.000
22	-10.984	-1.000				2.500	3.000
23	Infinity	-0.385	N-BK7	1.5168	64.15	10.700	10.700
24	Infinity	-0.260				10.700	10.700
25	Image	-	-	-	-	1.582	1.582

Table 4.4. Optical Prescription for 1.3mm F/2.8 Compact Folded Fisheye Lens

4.5 Design Evaluation

In this chapter the optical performance of the compact folded fisheye lens design is evaluated and compared to the original design requirements defined in Chapter 3. The total aberrations present in the lens are presented as an Optical Path Difference (OPD) [Fig. 4.8], and RMS wavefront error vs Field [Fig 4.19]. This analysis show that the maximum OPD wavefront error is 1.214 waves at the 95 degree field, with a plot scale of +/- 2 waves. The RMS wavefront error versus field analysis demonstrates that the folded fisheye lens has a maximum polychromatic RMS wavefront error of 0.14 waves across the field. An analysis of the Seidel aberration coefficients show that in addition to large amounts of distortion, the primary aberrations in the folded fisheye lens are astigmatism and field curvature [Fig. 4.11]. This can also be observed in the field curvature analysis presented in Fig. 4.10. The image plane is placed in the middle of the tangential and sagittal fields, where higher order field curvature is present; by balancing astigmatism, field curvature, and image plane defocus, a minimal spot size is obtained.

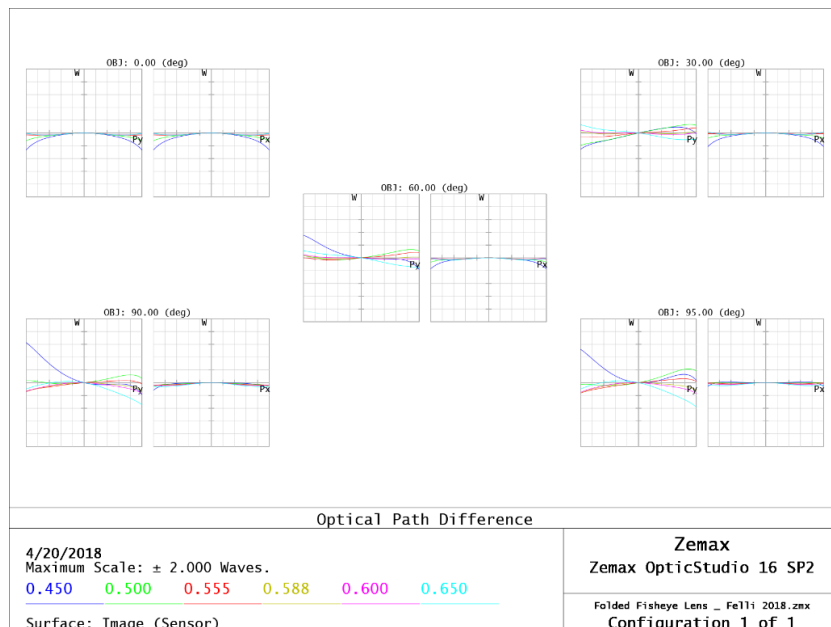


Figure 4.8. OPD for field heights ranging from 0 degrees to 95 degree half field of views, showing a maximum scale of +/- 2 waves

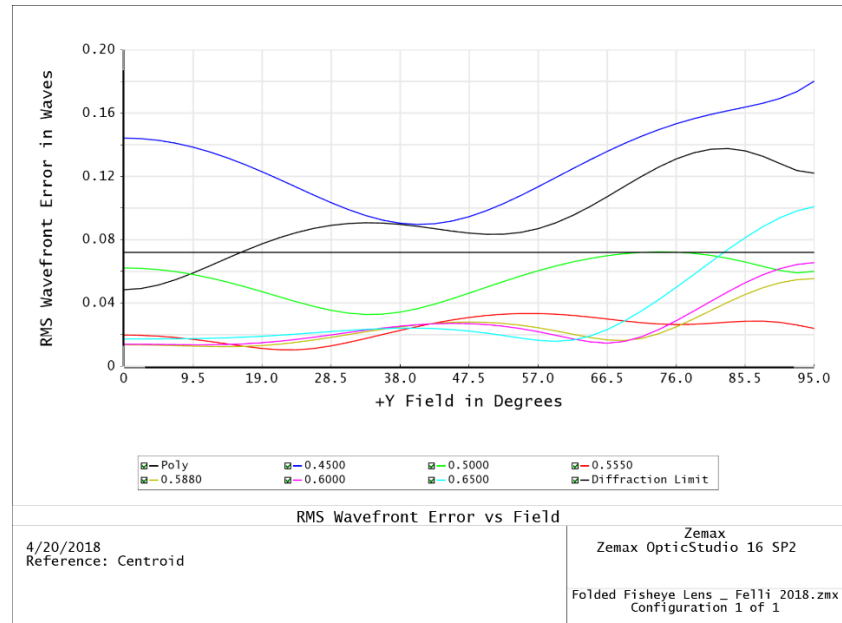


Figure 4.9. RMS Wavefront Error versus Field. Maximum RMS wavefront error is 0.18 waves at 450nm

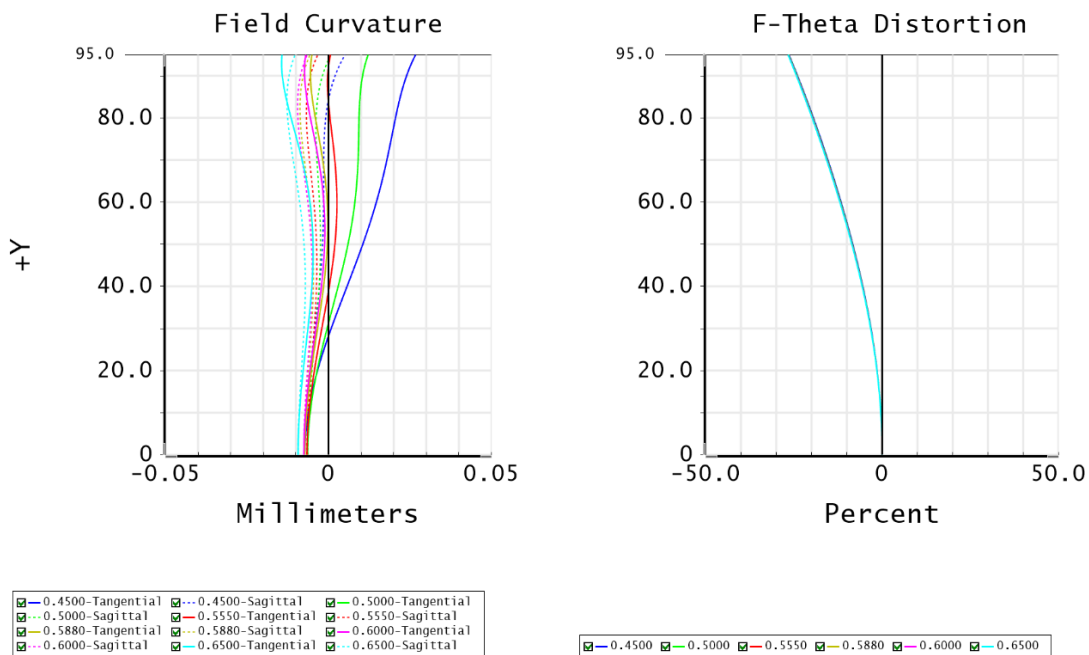


Figure 4.10. Field Curvature, Astigmatism, and $f\theta$ Distortion of Folded Fisheye Lens

Wavefront Aberration Coefficient Summary:							
TOT	W040 0.4561	W131 -0.7295	W222 25.4507	W220P 27.8730	W311 -2.69E+05	W020 0.2486	W111 19.0623
TOT	W220S 40.5983	W220M 53.3237	W220T 66.0490				

Figure 4.11. Wavefront coefficient aberration summary, showing lots of field curvature, astigmatism, and distortion left in the final image.

The distortion profile, measured as field of view versus image height, was analyzed in Zemax; This analysis shows that the folded fisheye lens has a distortion profile which is in between traditional equisolid angle distortion and orthogonal distortion. This distortion profile will have slightly more barrel distortion than ordinary equisolid fisheye lenses, but not as much barrel distortion as an orthogonal lens. Each type of distortion profiles discussed in Chapter 2.3 were scaled to the 1.3mm focal length of the folded fisheye lens and plotted for comparison [Fig. 4.12].

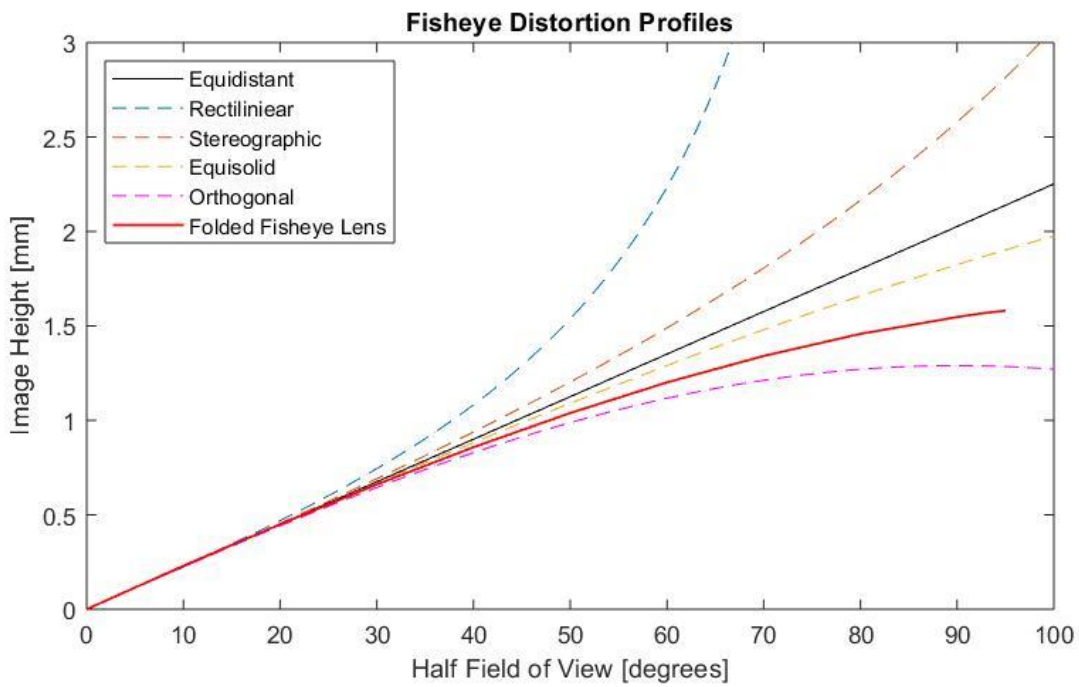


Figure 4.12. Half Field of View versus Image Height plot demonstrating the distortion profile in the folded fisheye lens compared to traditional fisheye distortion profiles with a focal length of 1.3mm

The use of two achromatic doublets and an element made of S-FPL53 resulted in the folded fisheye lens having excellent chromatic performance. An analysis of the chromatic focal shift [Fig. 4.13] shows that the folded fisheye lens is apochromatic, with zero chromatic focal shift between the wavelengths 408nm, 450nm, and 588nm. The maximum focal shift range for the full range of 400nm to 650nm is 3.011 μm . The lateral color aberration is shown to be diffraction limited in Fig. 4.14, with a maximum lateral color shift of 1.496 μm across the entire field. This lateral color shift is less than one pixel on the ON-Semiconductor AR0237 CMOS sensor, meaning that there should not be any lateral chromatic aberration which shows up in the final image per the design. While the lens will only be used between the 450nm to 650nm wavelength range per the UV/IR-cut filter chosen in Chapter 3.7, the fantastic chromatic performance would allow the lens to perform well in a wider wavelength range if necessary.

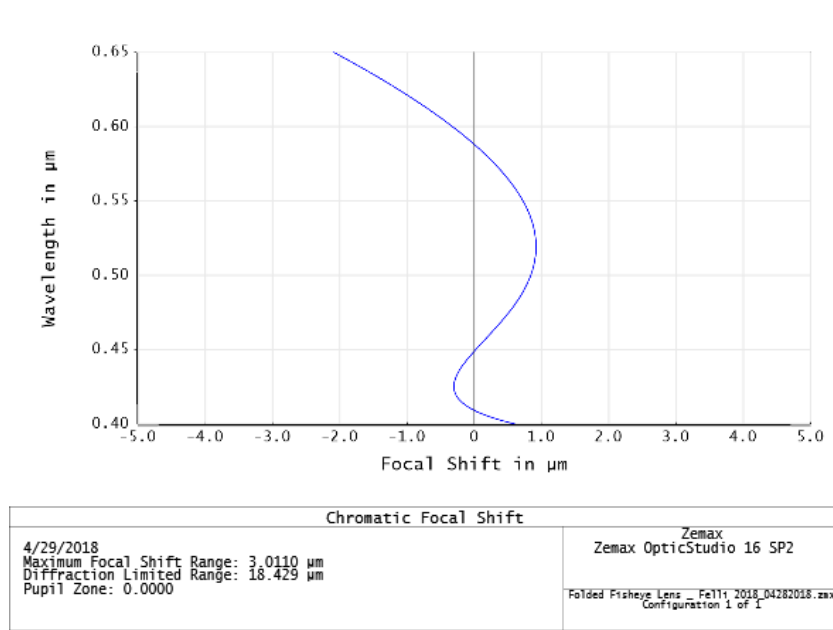


Figure 4.13 Chromatic Focal Shift versus Wavelength shows that the folded fisheye lens is apochromatic with zero chromatic focal shift between 408nm, 450nm and 588nm, with a maximum shift range of 3.011 μm

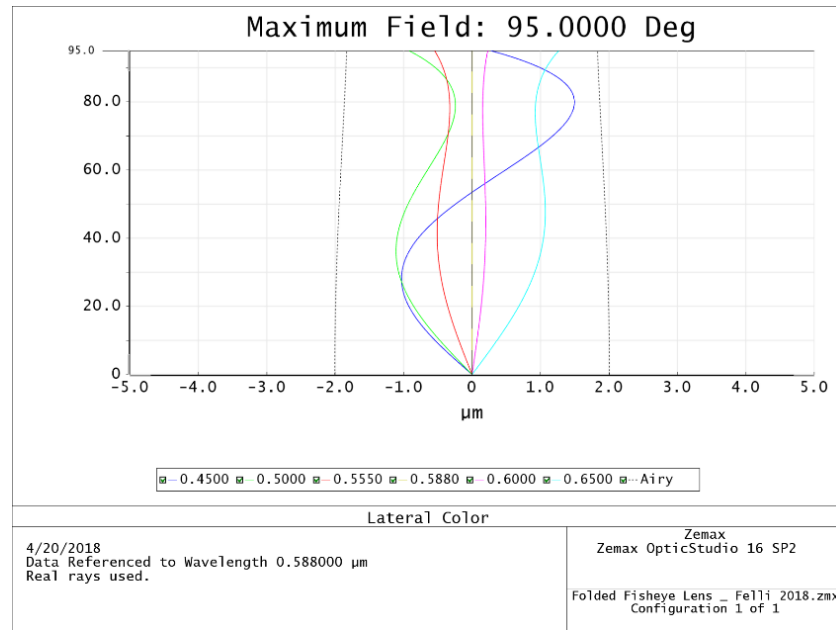


Figure 4.14 Lateral Chromatic Aberration Wavelength showing maximum lateral color shift of 1.496μm

The Spot Size vs Field analysis [Fig 4.15] and point spread functions [Fig. 4.16] show that the maximum RMS spot size is 1.296μm, with a geometrical radius of 5.664μm.

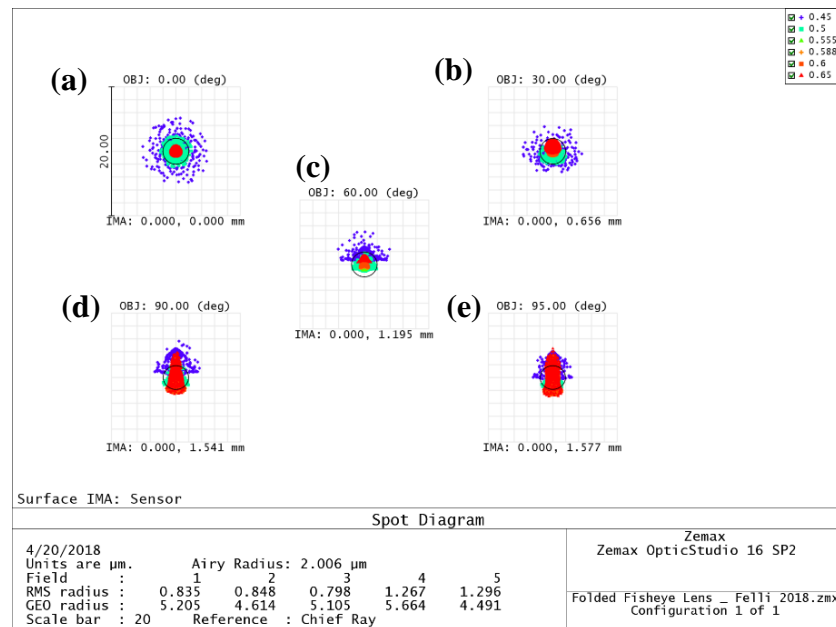


Figure 4.15 Spot Diagram for half fields of view of (a) 0 degrees, (b) 30 degrees, (c) 60 degrees, (d) 90 degrees, and (e) 92.5 degrees

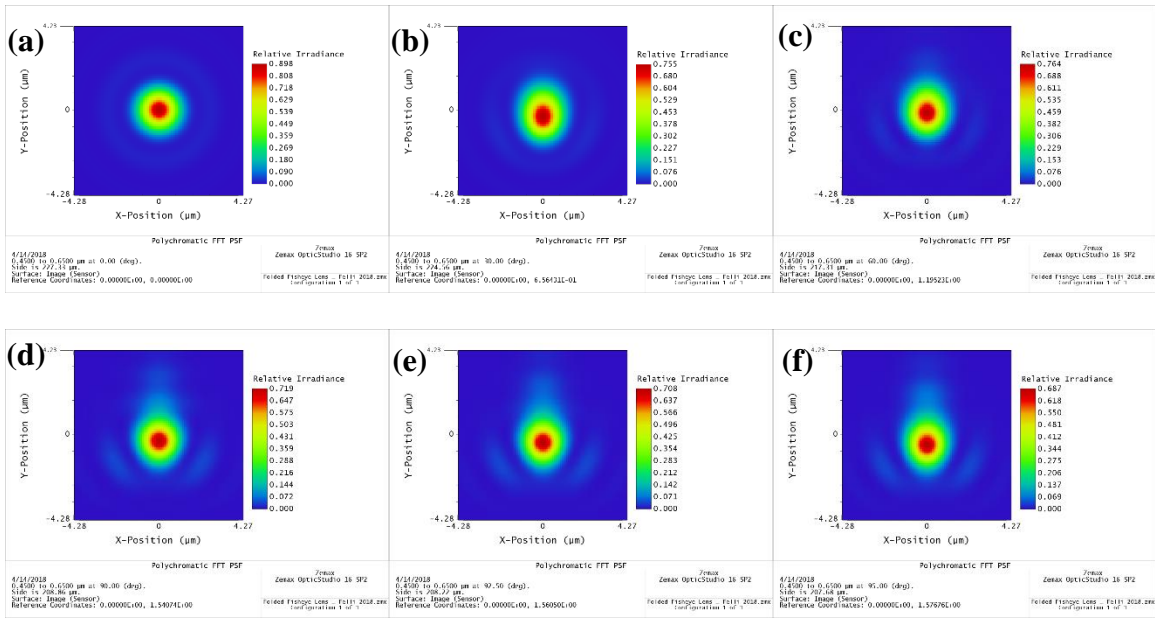


Figure 4.16 Polychromatic Point Spread Functions for half fields of view of (a) 0 degrees, (b) 30 degrees, (c) 60 degrees, (d) 90 degrees (e) 92.5 degrees and (f) 95 degrees

As the AR0237 image sensor has 3 μ m pixels, this shows that the root mean square of the optical energy in each spot will be kept within one pixel across all fields. All of the aberrations which are present in the optical system play a role in the point spread function that is received at the image plane. Because the modulation transfer function is related to the magnitude of the Fourier transform of the point spread function, the MTF performance of the lens is also directly related to the aberrations which in the lens.

The MTF performance of the folded fisheye lens is very high across all fields, which will ensure that the image quality of the full two-lens camera system will be very sharp all the way out to the region where the 190-degree field heights are stitched together. The minimum contrast at the Nyquist frequency of the AR0237 CMOS image sensor of 167lp/mm is 48% at the 95-degree half field of view [Fig. 4.17]. The MTF requirement defined in Chapter 3 is a minimum 30% MTF at 167lp/mm, which this design far exceeds; This is advantageous, as it provides room for the MTF to degrade during the tolerancing of the optical system while still meeting the requirement.

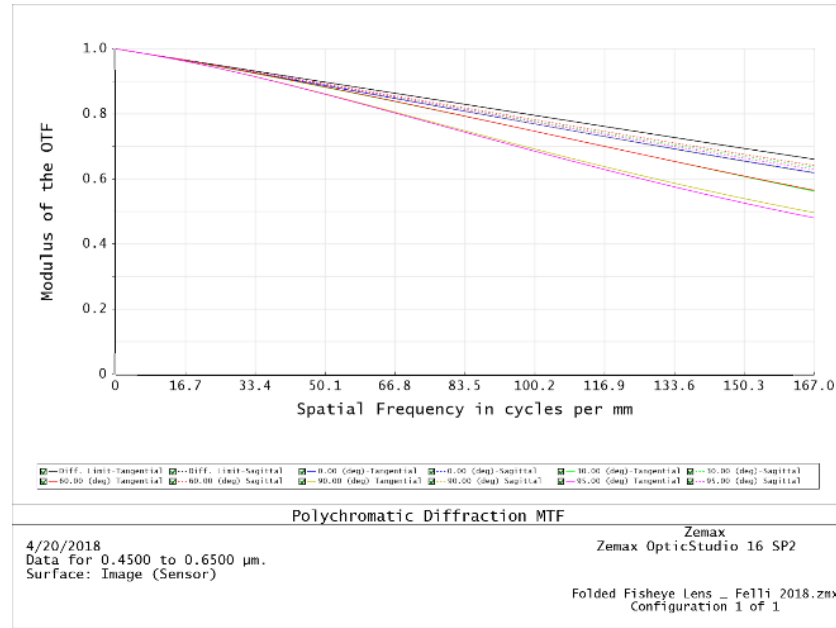


Figure 4.17. Polychromatic MTF versus spatial frequency up to 167lp/mm for field heights ranging from 0 degrees to 95 degrees. Minimum design MTF is 48%.

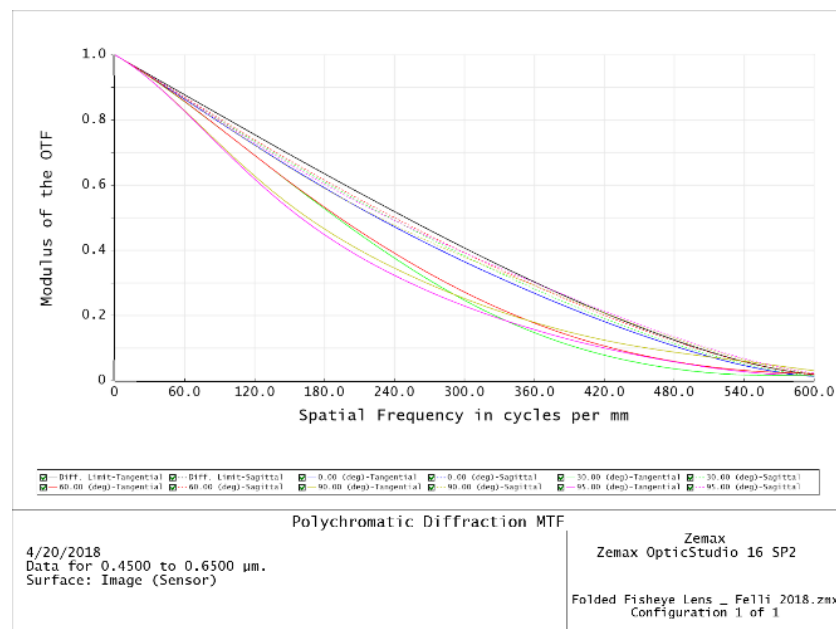


Figure 4.18. Polychromatic MTF versus spatial frequency up to 600lp/mm for all field heights, demonstrating greater than 30% MTF up until 240lp/mm

While analyzing the relative illumination in Zemax with fisheye lenses where there may be high incident angles on the first optical surfaces, the “Use Polarization” box must be checked. The relative illumination analysis of the folded fisheye lens [Fig. 4.19] shows a minimum relative illumination at the 95-degree field of 83.3%, where the peak relative illumination occurs at the 66.5-degree field height due to the Slyusarev Effect [29] as earlier discussed in Chapter 2.4.

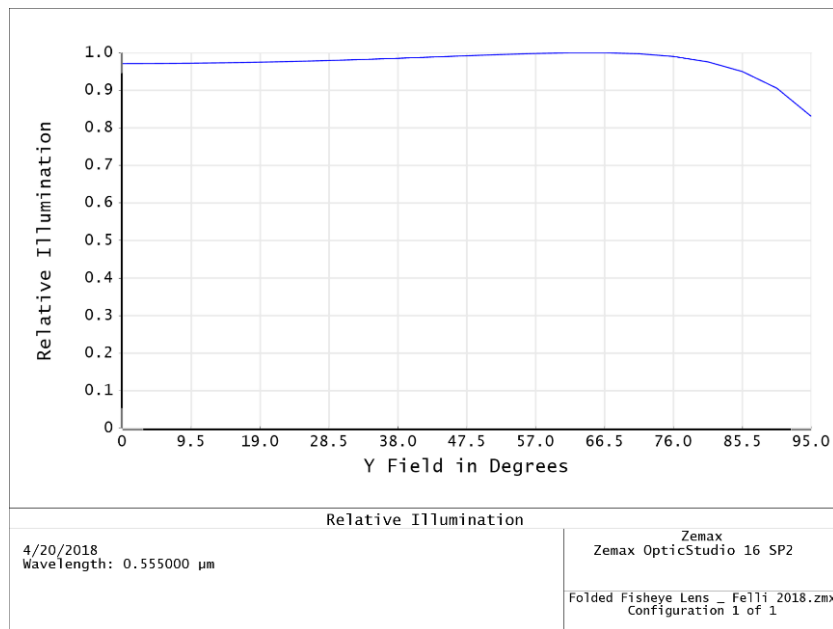


Figure 4.19 Relative Illumination plot, showing minimum R.I. equal to 83.3%

The ON-Semiconductor AR0237 CMOS image sensor is designed to accept a maximum chief ray angle of 12 degrees; an analysis of the chief ray angle shows that the maximum chief ray angle of the folded fisheye lens is 11.44 degrees at an image height of 1.582mm [Fig. 4.20], which meets the specification. It is common for other compact image sensors to be designed to accept chief ray angles larger than 12 degrees, all the way up to 30 degrees in some cases[33]; if this lens would need to be used with another imaging device in the future, the low chief ray angle would likely allow it to be a candidate for use with many other sensors.

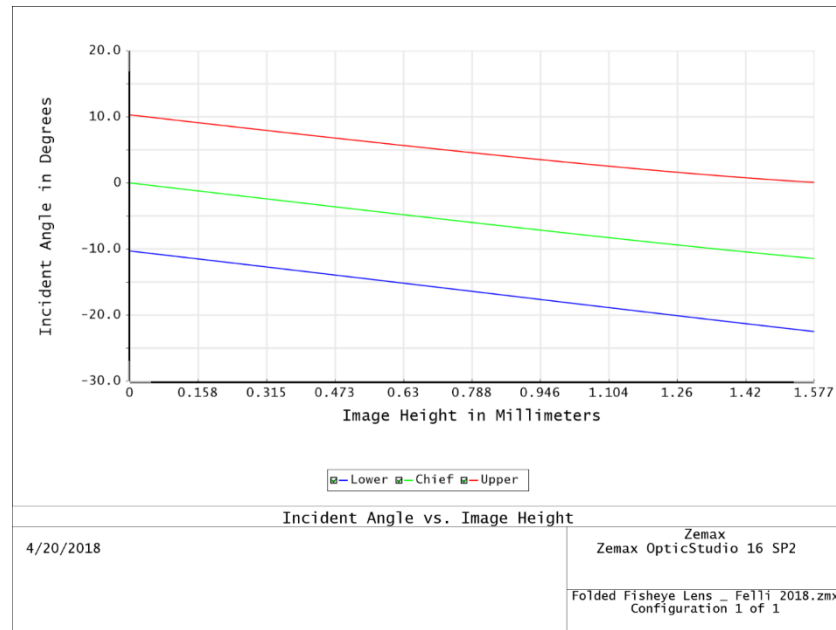


Figure 4.20 Chief ray angle versus image height, with a maximum CRA of 11.44 degrees

Lastly, the size of the compact folded fisheye lens is compared to the consumer-focused virtual reality cameras which were presented in Chapter 1. It can be seen that the two-lens folded fisheye lens system has a vertex-to-vertex thickness which is comparable to the Ricoh Theta, while being 11mm longer in width; however, the folded fisheye lens system is more compact than all of the other virtual reality options on the market currently, while exhibiting very high optical performance.

VR Camera Name	Vertex-to-Vertex Thickness	Height	Width
Ricoh Theta V	23mm	130mm	45mm
Folded Fisheye Lens	25mm	-	56mm
GoPro Fusion	39mm	73mm	75mm
Samsung Gear 360	45mm	101mm	46mm
Nikon Keymission 360	61mm	61mm	66mm
Garmin Virb 360	70mm	59mm	39mm

Table 4.5 Center thickness, height, and width dimensions of common virtual reality cameras. The Folded Fisheye lens' package size is just slightly larger than the Ricoh Theta

4.5.1 Tolerance Analysis

Consumer electronics are commonly manufactured in very high quantities, and the cost of the lenses used in these devices are directly related to the manufacturing yield. While a lens design can appear to perform very well in Zemax, the manufacturing tolerances associated with fabricating each element will degrade the image quality and can often lead to the as-built performance not meeting the design requirement specifications. Because of this, it is incredibly important to have an optical design which has high manufacturing yield when tolerances are considered. The tolerance analysis that the author used was a Monte Carlo analysis in Zemax; a Monte Carlo analysis applies random perturbations within a user-defined range to the parameters of each element over thousands of trials to simulate the manufacturing distribution of the final as-built optical performance. Tolerances will be applied to the radius of curvature, thickness, lens spacing, refractive index, surface tilt and decenter, and element tilts and decenters. For this tolerance analysis, the author utilized a tolerance guide from Zemax [30] to guide the tolerances which are used [Fig. 4.21].

Operand	Standard	Precision	High Precision
Wavefront Error	0.25λ RMS 2λ P-V	0.1λ RMS 0.5λ P-V	<0.07λ RMS <0.25λ P-V
Thickness	0.1 mm	0.01 mm	0.001 mm
Radius	1%	0.1%	0.01%
Index	.001	.0001	.00001
Decentre	0.1 mm	0.01 mm	0.001 mm
Tilt	1 arc min	10 arc sec	1 arc sec
Sphericity	2 fringes	1 fringes	0.25 fringes
Irregularity	1 fringe	0.25 fringe	<0.1 fringe
Aspherics	1%	0.5%	0.1%
Element Tilt	5 arc min	3 arc min	1 arc min
Element Decentre	0.25 mm	0.025 mm	0.005 mm

Figure 4.21. Standard Manufacturing Tolerances [30]

The tolerances which were selected fall between precision and high precision; tighter tolerances can often be achieved with very small lenses in high quantity manufacturing environments [44] through process optimization while still keeping cost to a minimal when using spherical glass elements. The tolerances which are used are listed in Table 4.6; in addition, the test wavelength which defines the radius fringe tolerance is set to 633nm, and the focus compensation option is turned on which will allow the lens to adjust the back focal distance to maximize MTF after each Monte Carlo trial.

	Operand	Tolerance
Surface Tolerances	Radius	1 Fringe
	Thickness	5um
	Decenter X,Y	5um
	Tilt X,Y	1 arcsec

	Operand	Tolerance
Element Tolerances	Decenter X,Y	7.5um
	Tilt X,Y	1 arcsec
	Index Tolerance	0.0001%
	Abbe Tolerance	1%

Options Used	
Test Wavelength	633nm
Use Focus Compensation	ON

Table 4.6. Tolerances used in the Monte Carlo analysis of the folded fisheye lens design

The author ran 1000 Monte Carlo trials using the Zemax settings shown in Fig. 4.22; The criterion for the analysis was set to geometrical tangential MTF because the tangential MTF is always lower than the sagittal MTF in the folded fisheye lens, with the test frequency set to the Nyquist frequency of the sensor of 167lp/mm. In addition, ray aiming is forced to be on. The results from running 1000 Monte Carlo trials are shown in Fig. 2.23.

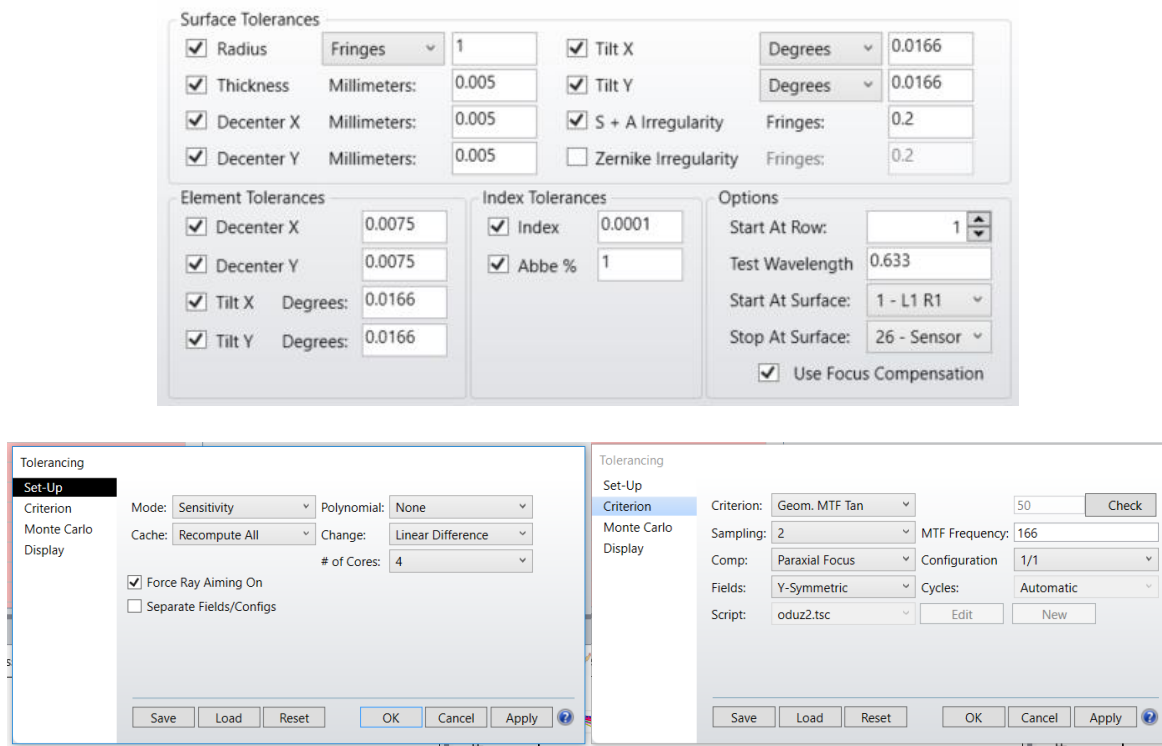


Figure 4.22. Monte Carlo Tolerance analysis settings used in Zemax

The results from running 1000 Monte Carlo trials are shown in Fig. 2.23. The analysis shows that 90% of the lenses have a minimum MTF greater than 33.6%, meaning that the folded fisheye lens would meet the MTF specification defined in Chapter 3 with a manufacturing yield of >90%. The mean MTF across all trials is reported at 42.3% with a standard deviation of +/- 5.9%, and the back focal length had a standard deviation change of +/- 7.7 μm across all trials. A plot of the distribution is shown in Fig. 4.24, which shows that a 94% yield can be expected with the tolerances used in Fig. 4.22.

```

Number of traceable Monte Carlo files generated: 995

Nominal      0.50854604
Best         0.51395425   Trial    434
Worst        0.17110308   Trial    807
Mean          0.42323781
Std Dev      0.05934916

Compensator Statistics:
Change in back focus:
Minimum       : -0.022598
Maximum       : 0.023001
Mean          : -0.000199
Standard Deviation : 0.007738

98% >     0.26185854
90% >     0.33692652
80% >     0.37841151
50% >     0.43677207
20% >     0.47249669
10% >     0.48492619
 2% >     0.50000133

End of Run.

```

Figure 4.23. Monte Carlo Tolerance Analysis results from 1000 trials

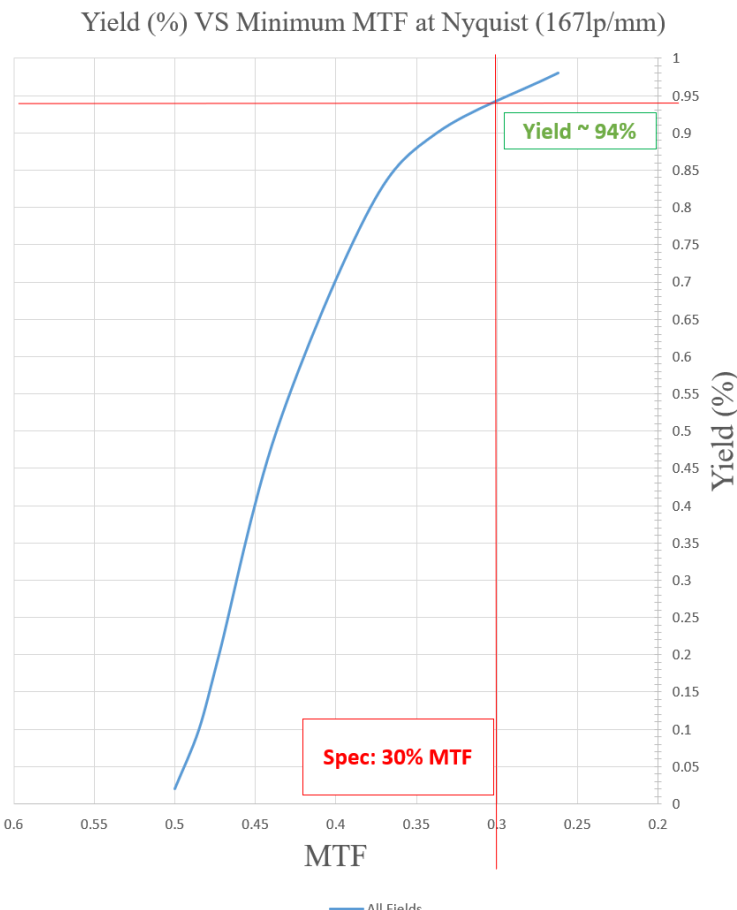


Figure 4.24. Minimum MTF Distribution at 167lp/mm, showing a 94% yield with the tolerances listed in Table 4.6

The Monte Carlo analysis also provides a sensitivity analysis to determine which surfaces in the design are the most sensitive, and which tolerance it was the most sensitive to. The report lists the worst offenders in a list [Fig. 4.25]. The sensitivity analysis shows that the three most sensitive surfaces in the optical design are surface 10, surface 15, and surface 12 [Fig. 4.26] in that order, with each being the most sensitive to tilt in the Y direction by 1 arcsecond. Surface 10 and surface 12 are the front and back surfaces of the first achromatic doublet used in the optical design, where the chance of misalignment between the two surfaces are less likely than air-spaced elements. Surface 15 is the buried surface in the second achromatic doublet and has the smallest radius of curvature of all the optical surfaces used in the design.

Worst offenders:				
Type		Value	Criterion	Change
TIRY	10	0.01660000	0.41534780	-0.12806549
TIRY	10	-0.01660000	0.41794338	-0.12546992
TIRY	15	-0.01660000	0.46032071	-0.08309259
TIRY	15	0.01660000	0.46032071	-0.08309259
TIRY	12	-0.01660000	0.46239210	-0.08102120
TIRY	12	0.01660000	0.46301785	-0.08039545
TIRY	18	0.01660000	0.47418155	-0.06923175
TIRY	18	-0.01660000	0.47418155	-0.06923175
TIRY	21	-0.01660000	0.47461863	-0.06879466
TIRY	21	0.01660000	0.47461863	-0.06879466

Figure 4.25. Worst offenders list from the Monte Carlo sensitivity analysis with 1000 trials

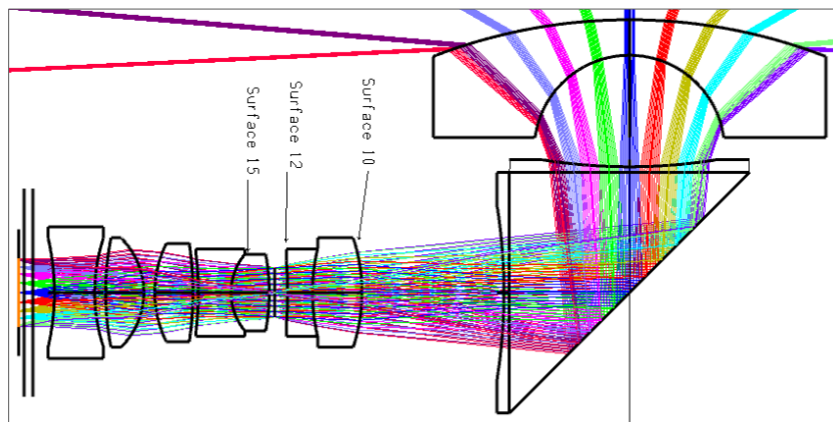


Figure 4.26. 2D Layout of folded fisheye lens highlighting the three most sensitive surfaces to tolerance perturbations in the optical design

While running a tolerance analysis in Zemax, the performance of each Monte Carlo trial can be overlaid onto the analysis windows which are open. To visualize the MTF performance spread, the author has performed 20 Monte Carlo trials where the MTF performance of each trial is shown along with a line representing the 30% minimum MTF specification [Fig. 4.27]. All field heights from on-axis to 95 degrees are plotted, and only 2 out of 20 of the plots are shown to drop below the 30% MTF line, representing a ~90% yield.

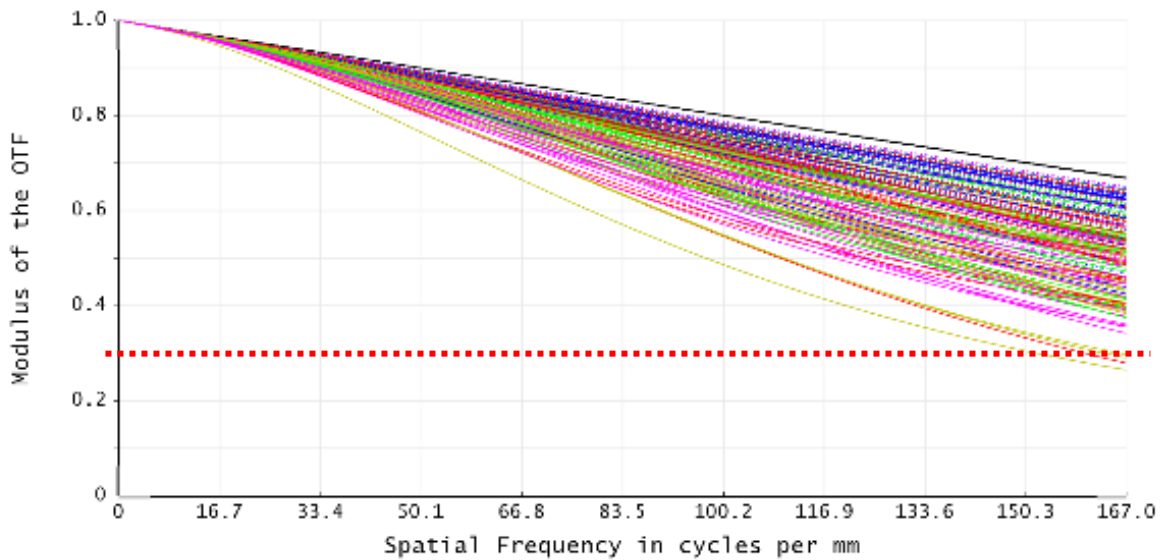


Figure 4.27. MTF distribution over 20 Monte Carlo trials, showing an estimated 90% yield

While the tolerances used in this optical design are assumed to be relatively tight, the performance of the lens is very high and meets the MTF specification for an estimated 94% of the lenses which would be manufactured using the tolerances outlined in Table 4.6. The high yield that this lens would achieve can offset the cost associated with tight tolerances and result in an overall low-cost optical system which could be manufactured in large quantities.

4.5.2 Total Internal Reflection Evaluation

A high index prism was chosen in Chapter 4.2 to improve the chances of TIR occurring at the higher field angles. It is crucial for there to be 100% total internal reflection on the prism interface for all field angles, or the optical system may experience an increased drop in relative illumination. In addition, some complications may arise if light escapes the prism due to the other fisheye lens' prism being on the other side; this could result in stray light occurring in one fisheye lens system which comes from the opposite lens. To determine whether TIR occurs for all field angles, an analysis on the incident angle of the chief and marginal rays at the prism was performed.

For TIR to occur, the incident angle must be larger than 31.71 degrees for the L-LAH86 glass type with an index of 1.9027 used for the molded glass prism. From the analysis, it was determined that the incident angle on this surface ranges from a minimum of 35.39 degrees to a maximum of 54.61 degrees [Fig. 4.28], meaning that 100% of the light from all fields will experience total internal reflection within the prism as long as an airgap is present.

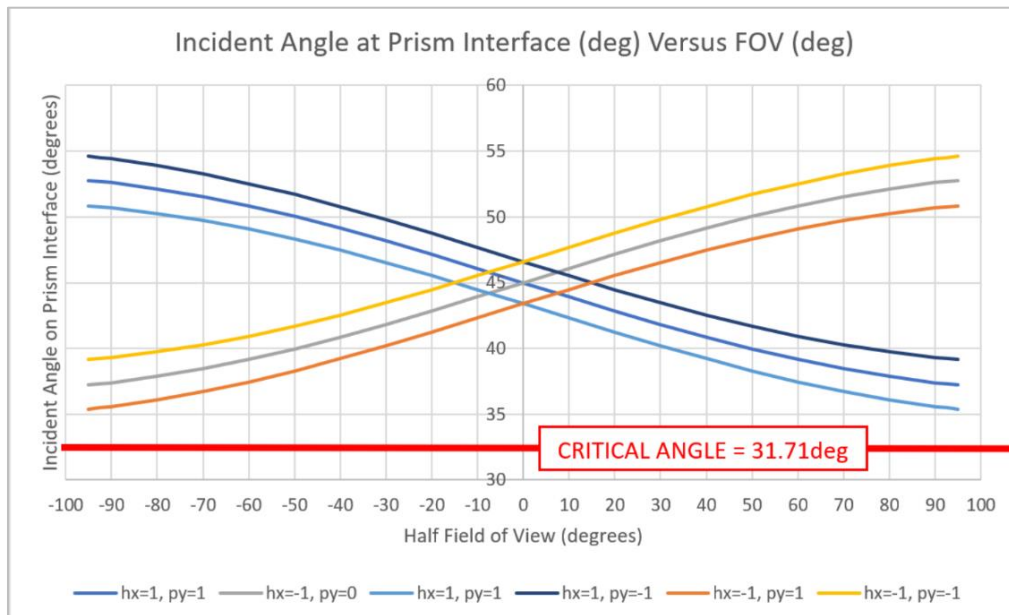


Figure 4.28. Incident angle versus half field of view on the prism's reflecting interface, demonstrating 100% TIR for all field angles in the folded fisheye lens design

4.5.3 Entrance Pupil Position versus Image Height

As discussed in Chapter 2.4, fisheye lenses exhibit large amounts of pupil aberration including pupil spherical aberration from the negative meniscus lens elements and pupil coma from the large amounts of image distortion. These cause the entrance pupil to change axial location (pupil walking), tilt with respect to the optical axis, and become elliptical as the field of view increases. Quantifying how the pupil changes is generally not necessary when analyzing a fisheye lens in Zemax as long as the Ray Aiming tool is turned on; however, the folded fisheye lens' stray light will be analyzed in the non-sequential optical design software FRED which does not have a ray aiming tool. Because of this, the pupil walk in the folded fisheye lens is quantified to be used in other analysis'. To find the axial location of the entrance pupil for each field, the chief rays which are entering the first lens surface are projected through the system until they reach the optical axis, where that axial location is defined as the entrance pupil location for that field height. This process is shown in Fig. 4.29 for the folded fisheye lens design; the entrance pupil locations for the 30-degree field, 60-degree field, and 95-degree field are noted.

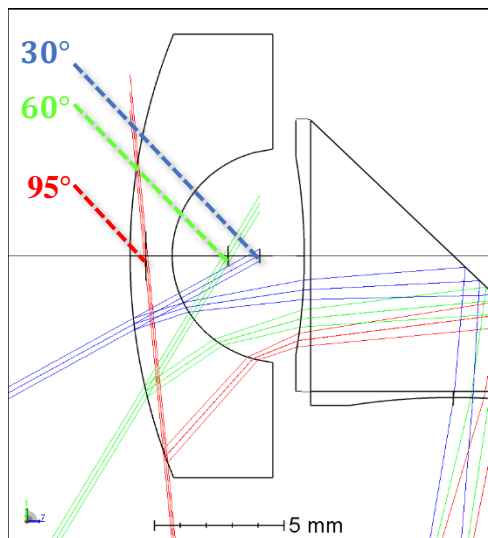


Figure 4.29 Entrance pupil shift visualized for the folded fisheye lens design at 30-degree, 60-degree, and 95-degree field heights.

The measured entrance pupil position versus field of view of the folded fisheye lens is shown in Fig. 4.30. This data was measured in Zemax by locating where the chief ray for each field intersects the optical axis. The entrance pupil position is referenced from the first surface of the first element, where a positive value refers to a shift along the optical axis towards the image plane. The entrance pupil on-axis is located 5.295mm behind the vertex of the first lens surface in the design, and the pupil shifts towards the object as the field of view increases for a minimum entrance pupil distance of 0.613mm at the 95-degree field height. The full entrance pupil shift range for this lens is 4.682mm which is relatively large in relation to the size of the total track length of the lens.

Half FOV (degrees)	Image Height (mm)	E.P. Location (mm)
0	0	5.295
10	0.23	5.235
20	0.45	5.125
30	0.661	4.935
40	0.858	4.658
50	1.039	4.278
60	1.201	3.776
70	1.341	3.125
80	1.458	2.295
90	1.547	1.266
92.5	1.566	0.931
95	1.581	0.613

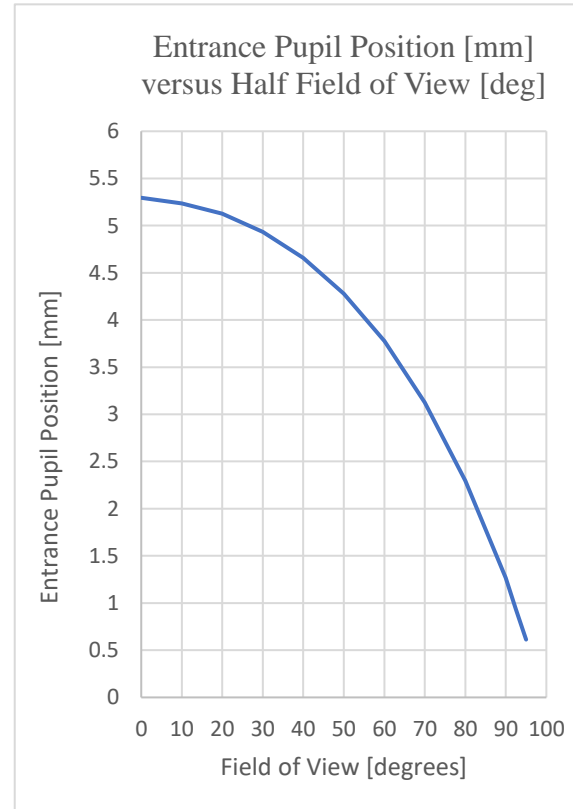


Figure 4.30. Measured entrance pupil position versus field of view in the folded fisheye lens

4.5.4 Optical Performance versus Requirements Summary

A summary of the optical performance versus requirements is shown in Table 4.7.

Merit	Requirement	Folded Fisheye Lens Performance
Image Sensor	ON-Semiconductor AR0237 CMOS Sensor	ON-Semiconductor AR0237 CMOS Sensor
Image Circle Half-Diagonal (mm)	1.582mm	1.582mm
FOV	>190 degrees	190 degrees
F#	<=2.8	F/2.8
Vertex-to-Vertex Thickness of 2-Lens Module	<30mm	25mm
Sensor-to-Sensor Width of 2-Lens Module	< 75mm	56mm
Number of Elements	<10. All Spherical	8 spherical elements in 6 groups
Optical Folding Mechanism	Moldable Glass Prism	Moldable Glass Prism
Sensor Cover Glass Thickness	0.385mm, Made of N-BK7	0.385mm, with N-BK7 used in prescription
CG to Sensor Distance	0.26mm	0.26mm
BFL	>= 1mm	1.645mm
Glass Types	Schott, Ohara, Hoya, CDGM Only	Schott, Ohara
Wavelength Range (um)	450nm to 650nm, Custom Wavelength Weighting	450nm to 650nm, Custom Wavelength Weighting
Maximum RMS Spot Size	3um (one pixel)	1.296um
MTF	>30% MTF at 167lp/mm	>48% MTF at 167lp/mm
Lateral Chromatic Aberration	< 6um (two pixels)	<2um
Chief Ray Angle @ 100% IH	<12 Degrees	11.44 Degrees
Relative Illumination	>50%	>83%
Total Internal Reflection	100% TIR at all fields	100% TIR at all fields
EP Shift Range	-	4.682mm shift from 0° to 90°
Manufacturing Yield	>90%	~94% Yield

Table 4.7. Optical Performance Requirements for Folded Fisheye Lens

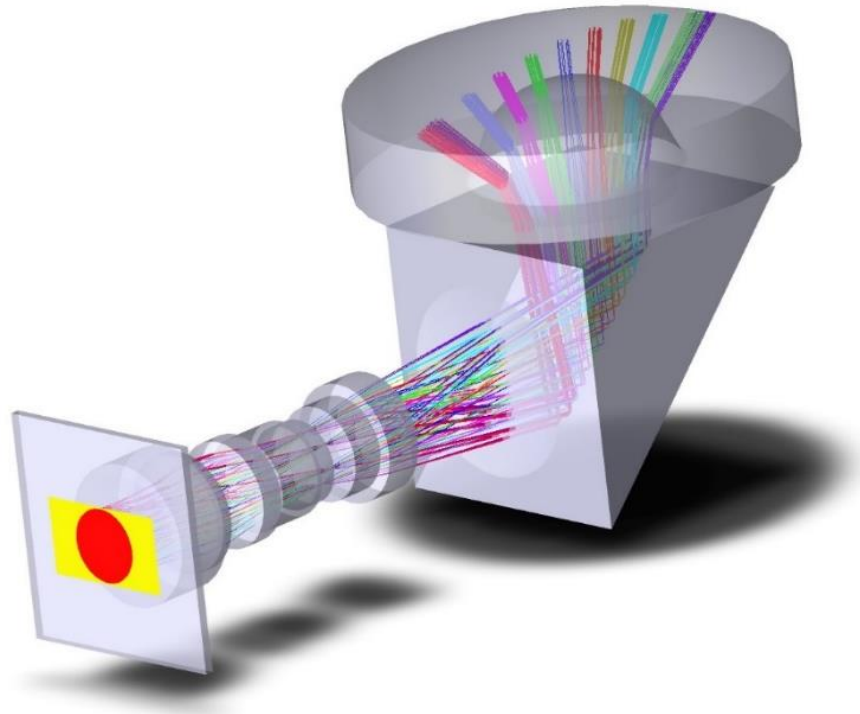


Figure 4.31. 3D Layout of the compact folded fisheye lens design.

As seen in Table 4.7, the optical performance of the folded fisheye lens designed in this master's thesis report exceeds all optical requirements which were defined in Chapter 3. The 1.297mm focal length F/2.8 lens is well-matched with the ON-Semiconductor AR0237 CMOS image sensor across the entire 190-degree field of view, all while maintaining a very compact form factor of 25mm x 56mm for the two-lens system. All eight optical elements in the system and the molded glass prism use only spherical surfaces to allow for this lens to be manufactured at low cost with high yield.

4.5 Multi-Camera Configuration and Stitch Location

Each fisheye lens in a virtual reality camera captures a hyper-hemispherical image; When two of the folded fisheye lenses are placed back-to-back at the prism's reflecting interface, the 95-degree fields will overlap on the optical axis [Fig. 4.32]. The distance at which both fields overlap is referred to the stitch location and is measured with respect to the vertex of the first lens element. Any objects which lie outside of this overlap region can be stitched into the reconstructed photosphere.

The distance from the vertex of the first lens element to the location where the 95-degree field crosses the optical axis for the folded fisheye lens occurs at approximately 135mm [Fig. 4.33], enabling the compact folded fisheye lens to stitch any objects which lie outside of a 270mm diameter sphere from the center of the two-lens assembly [Fig. 4.34].

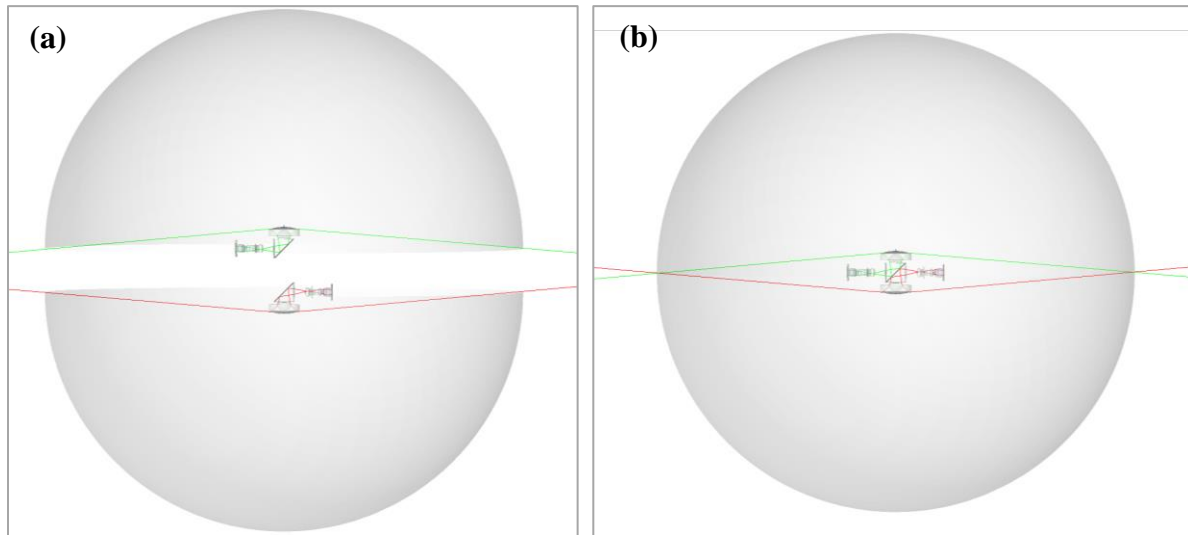


Figure 4.32. (a) Two folded fisheye lenses shown each capturing hyper-hemispherical images when separated. **(b)** Two folded fisheye lenses capturing a full 360-degree photosphere when both systems are placed back-to-back at the prism's reflecting interface.

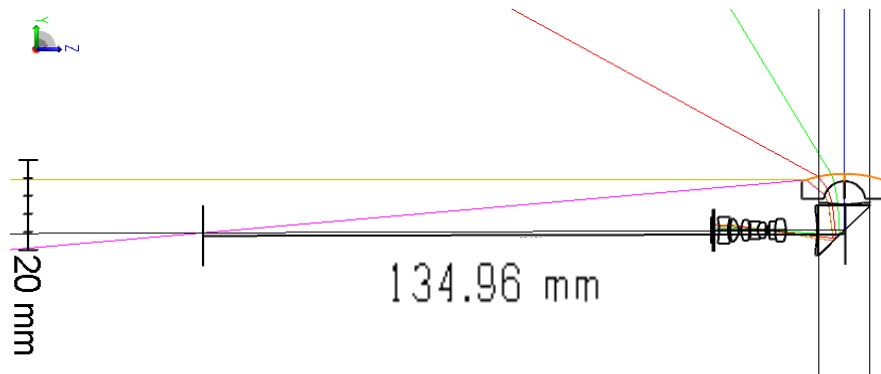


Figure 4.33. 2D Schematic of the folded fisheye lens showing the 95-degree field crossing the optical axis at a distance of 135mm from the vertex of the first lens.

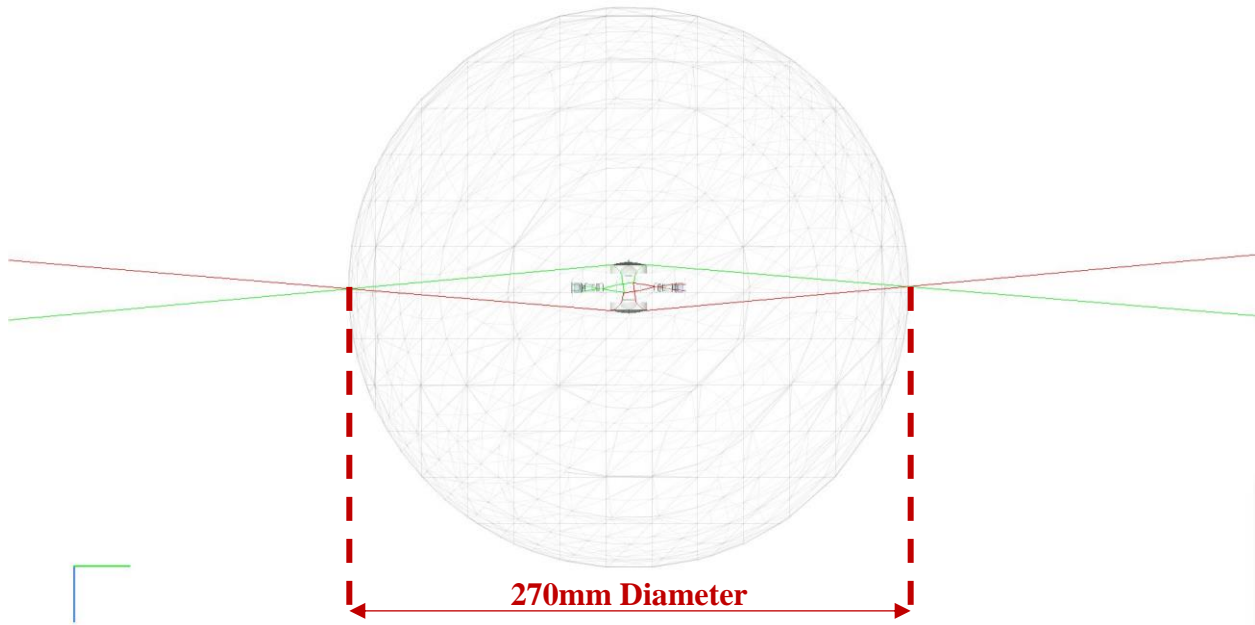


Figure 4.34. 3D Schematic of the folded fisheye lens showing the two-lens system's ability to stitch/reconstruct any objects outside of a 270mm diameter sphere.

Many use-case scenarios for consumer-focused virtual reality cameras will find the user holding the camera out at arm's length; a stitch distance of 135mm will allow the camera to reconstruct any objects from the middle of the forearm onward with an outstretched arm for most people, which is comparable to many products on the market today.

5 STRAY LIGHT ANALYSIS OF FOLDED FISHEYE LENS

Optical ghosts, which are dim and out of focus images of a bright source like the sun, are created by internal reflections of light on lens element surfaces; Rays which experience an even number of reflections off lens element surfaces while ending at the image sensor will be seen in the final image which can cause undesirable effects such as a reduction in contrast and distracting ghost images. In addition, stray light which scatters off the lens barrel and any other mechanical components in the system may also make it to the image sensor and will create distracting artifacts. This stray light plays a large role in the day-to-day experience of consumer electronic cameras where the contrast reduction and bright ghost images are expected to be minimal.

Due to their utilization of two fisheye lens imaging systems, where the image is stitched together to reconstruct a 360⁰ photosphere, virtual reality camera systems require special attention to the lens' stray light performance. The stray light and ghosts which are seen on one lens system will often not be replicated on the other which can accentuate the appearance of these ghosts. Stray light may cause the contrast of one half of the image to be lower than the contrast of the other half, or ghosts may appear to be 'cut off' as they pass through the stitch line. Because of this, it is crucial to optimize stray light performance of virtual reality imaging systems.

In this chapter, the author utilizes the non-sequential design software package FRED by Photon Engineering to analyze the ghost performance of the folded fisheye lens which was designed in Chapter 5. By performing a stray light analysis and ghost analysis of this optical system, the stray light of the final compact virtual reality camera can be simulated, and the optimal position of the highly-reflective ultraviolet and infrared cut-off filters can be chosen to minimize any distracting stray light artifacts in the use-case of the final camera product.

5.1 Stray Light in Cameras

Unwanted stray light effects have always been a problem in camera systems; incoming light which internally reflects off of lens elements and makes it back to the image will cause a reduction in contrast of the scene that one is photographing, and in many instances will cause ghost images artifacts in the image which can have high irradiance in relation to the image of the scene. Fig. 5.1 demonstrates the potential reflection paths that are present in a thick lens [24]; as shown, only the rays which experience an even number of reflections continue propagating towards the image plane. These even-numbered ray paths are the primary focus of this chapter.

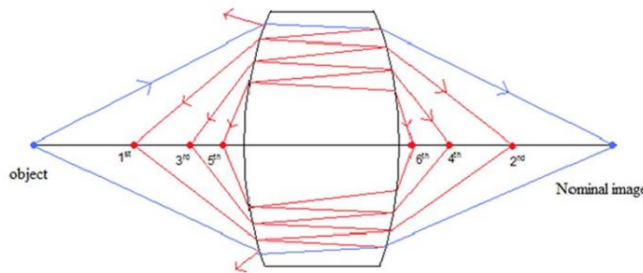


Figure 5.1. Ghost image locations formed by a thick lens [24]

In more complicated optical systems, there are many potential paths for a reflected ray to take before landing back at the image plane. Fig. 5.2 shows two potential ghost ray paths in a doublet lens. The ghost image plane is generally not coincident with the nominal image plane, which often causes the ghosts to appear as large defocused spots.

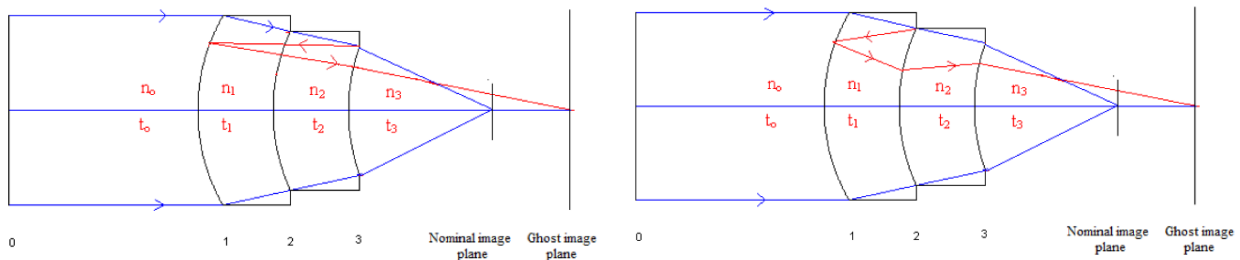


Figure 5.2 Ghost ray paths in a doublet lens [24]

Each time that a ray interacts with an optical surface, some percentage of the energy in that ray is reflected, absorbed, and transmitted through the optical system. While glass surfaces generally have a reflectance of 4% at normal incidence, many lens systems utilize multilayer thin-film antireflection coatings which can reduce the reflectance down to 0.4%. When the ghost image plane is far enough from the nominal image plane, the defocused ghost image can cover the entirety of the image sensor which results in a general reduction of contrast in the image [Fig 5.3]. When the ghost image plane is relatively close to the nominal image plane, it will show up as brighter defocused spots which often have color as can be seen in Fig. 5.4.

Other effects can be seen in Fig. 5.4 such as pedal flare and shower flare, neither of which are caused by the light reflecting off of lens element surfaces; Because a mechanical enclosure has not yet been designed for the folded fisheye lens, this effect will not be addressed in this paper. However, it is worth noting that this effect can be modeled using non-sequential optical design software if a mechanical model of the full system is available.



Figure 5.3. Contrast reduction due to stray light in an imaging system. (left) Photo with stray light. (right) Photo without stray light [24]

In virtual reality cameras, this stray light can be especially problematic. Most consumer virtual reality cameras today utilize two fisheye lenses paired with two image sensors, where the field of view of each fisheye lens is greater than 180^0 . Because the fields of view of both lenses overlap, the two hemispherical images can be stitched together to reconstruct a full 360^0

photosphere. When viewing the final video or photograph which is captured from this camera, the user commonly has the option pan around and view any portion of the photosphere, meaning that the image quality at the edge of the field of view of each lens is equally important as in the center of the lens to the end-user.

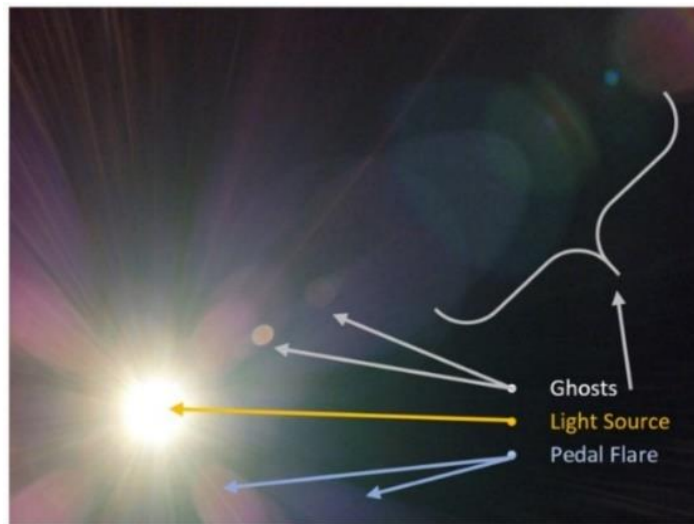
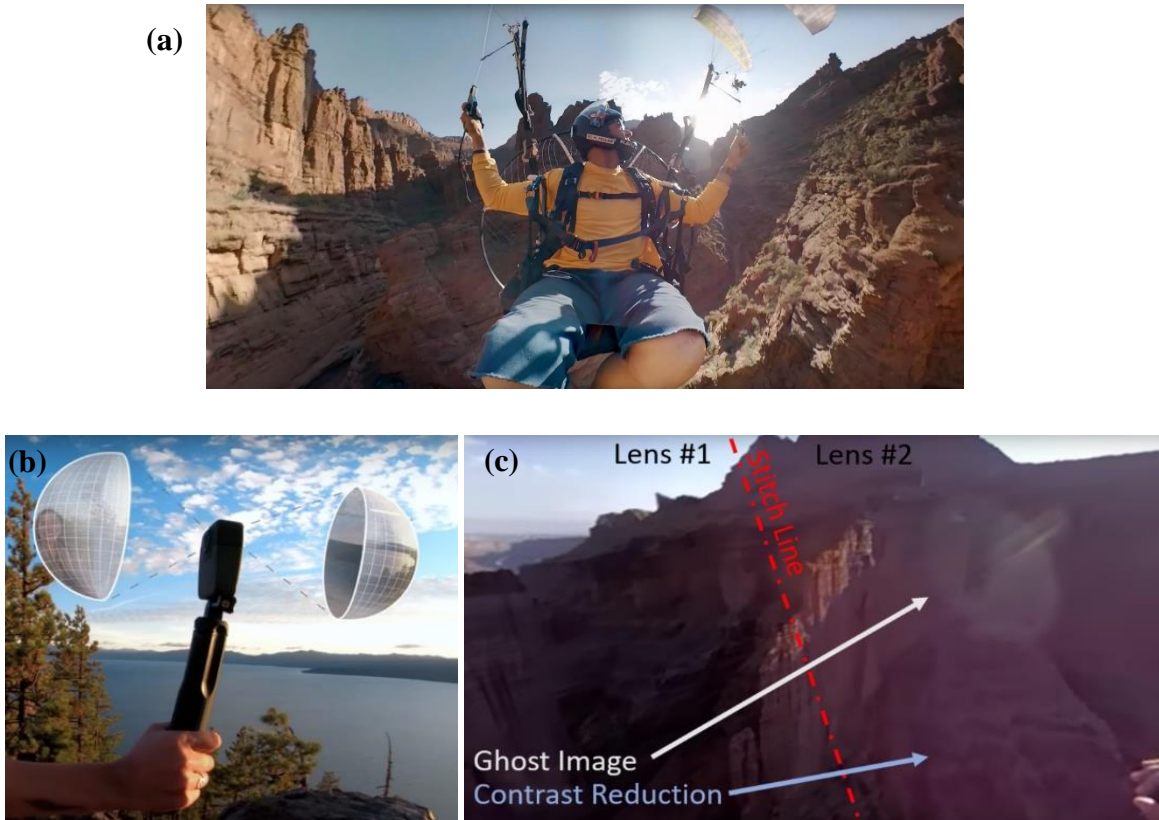


Figure 5.4. Ghost images and pedal flares seen in a digital GoPro camera. Taken in a dark room with a bright flashlight directed at the camera.

Fig. 5.5 demonstrates how two fisheye lenses capture a full 360-degree photosphere in the GoPro Fusion VR camera. When viewing the region where these two images are stitched together, stray light effects can be accentuated. An example of a ghost and contrast reduction from of stray light that is caused by the sun being in the field of view of only one of the fisheye lenses in this camera is also shown [Fig. 5.5 (c)]. In this example, a user is using the VR camera while paragliding in a canyon where shadows create high contrast regions. The ghosts and contrast reduction which occur as a result of stray light in only one lens of the two-lens system become accentuated when viewing the region where the two images are stitched together, emphasizing the need for optimal stray light performance in these devices.



**Figure 5.5. (a) Person using a VR Camera in a canyon while paragliding,
(b) Demonstrating the photosphere image capture on the GoPro Fusion VR Camera,
(c) Stray light effects observed when the sun is only in the field of view of one lenses [5]**

In the author's experience, ghost images which are seen in the final image are highly dependent on which optical element the highly reflective UV/IR-cut filter is coated onto; While it is not possible to eliminate these unwanted stray light effects entirely, the optical designer can choose to place the highly-reflective UV/IR-cut filter onto a surface which does not heavily contribute to ghost images to minimize the stray light artifacts in this imaging system. The goal in this chapter is to analyze the ghost performance of the folded fisheye lens to determine which surfaces contribute to the most prominent ghosts and locate the most optimal location for the UV/IR-cut filter such that the ghost images are minimal.

5.2 Reflectance and Coating Assumptions

The irradiance of a ghost image in an imaging system is directly related to the reflectance of the surfaces which make up that ray path. The reflectance of an optical surface assuming normal incidence is given by

$$R = \left(\frac{n_1 - n_2}{n_1 + n_2} \right)^2 \quad (5.1)$$

where n_1 and n_2 are the indices of refraction of the two materials which form the surface. Assuming $n_1=1$ and $n_2=1.5$, one can assume a general reflectance of $R = 4\%$ for glass surfaces which are being used in air. When the incident angle is not at normal incidence to the surface, the reflectance becomes polarization dependent and is described by the Fresnel Reflection equations [25]. The Fresnel reflection equations for s and p polarization are expressed by

$$R_s(\theta_1, \theta_2) = \left[\frac{n_1 \cos(\theta_1) - n_2 \cos(\theta_2)}{n_1 \cos(\theta_1) + n_2 \cos(\theta_2)} \right]^2 \quad (5.2)$$

$$R_p(\theta_1, \theta_2) = \left[\frac{n_1 \cos(\theta_2) - n_2 \cos(\theta_1)}{n_1 \cos(\theta_2) + n_2 \cos(\theta_1)} \right]^2 \quad (5.3)$$

where θ_1 is the incident angle and θ_2 is the exitance angle. Snell's law can be applied to express both equations in terms of only the incident angle θ_1 , where the reflectance of the s-polarized and p-polarized rays are then represented as

$$R_s(\theta_1) = \left[\frac{n_1 \cos(\theta_1) - n_2 \left[1 - \frac{n_1^2}{n^2} \sin(\theta_1)^2 \right]^{0.5}}{n_1 \cos(\theta_1) + n_2 \left[1 - \frac{n_1^2}{n^2} \sin(\theta_1)^2 \right]^{0.5}} \right]^2 \quad (5.4)$$

$$R_p(\theta_1) = \left[\frac{n_1 \left[1 - \frac{n_1^2}{n^2} \sin(\theta_1)^2 \right]^{0.5} - n_2 \cos(\theta_1)}{n_1 \left[1 - \frac{n_1^2}{n^2} \sin(\theta_1)^2 \right]^{0.5} + n_2 \cos(\theta_1)} \right]^2. \quad (5.5)$$

If the material is assumed to be glass with index of 1.5 in air, the reflectance for the p-polarized rays go to zero at 56.31 degrees which is commonly referred to as Brewster's angle. This same phenomenon does not occur for the s-polarized light, however, and the reflectance only increases with incident angle. Imaging optics for cameras are most commonly used in scenarios with randomly polarized light; for randomly polarized light, the s-polarized and p-polarized light is assumed to have equal power [25], and the total reflectance can be represented as

$$R(\theta_1) = \frac{R_s(\theta_1) + R_p(\theta_1)}{2}. \quad (5.6)$$

When plotting $R_s(\theta_1)$, $R_p(\theta_1)$ and the randomly polarized $R(\theta_1)$ together [Fig. 5.6], it can be seen that the reflectance for randomly polarized light is near 4% up until a 60-degree incident angle where the reflectance begins to increase until reaching 100% reflectance at a 90-degree incident angle.

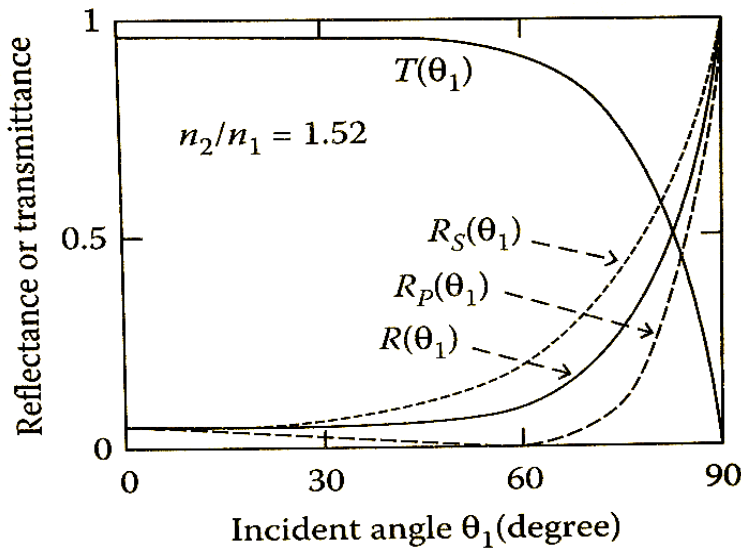


Figure 5.6. Reflectance of s-polarized $R_s(\theta_1)$, p-polarized $R_p(\theta_1)$, and randomly polarized $R(\theta_1)$ light as a function of incident angle on an optical surface

The most common way to reduce the reflectance of optical surfaces is to utilize multilayer antireflection (AR) coatings. Generally, the optical designer must consult an optical coating designer for details on the reflectance of AR-coatings as a function of wavelength and incident angle. For the sake of this stray light analysis, the author has assumed antireflection properties of commonly used coatings in the industry. Edmund Optics [26] has a catalogue of standard antireflection coatings which are designed to be used in the visible wavelength region [Fig. 5.7]. Out of Edmund Optics' selection of coatings, the Vis0° coating that they offer best suits the needs for this application; the Vis0° coating covers a wavelength region from 425nm to 675nm, and is advertised to have a maximum reflectance of 0.4% [26].

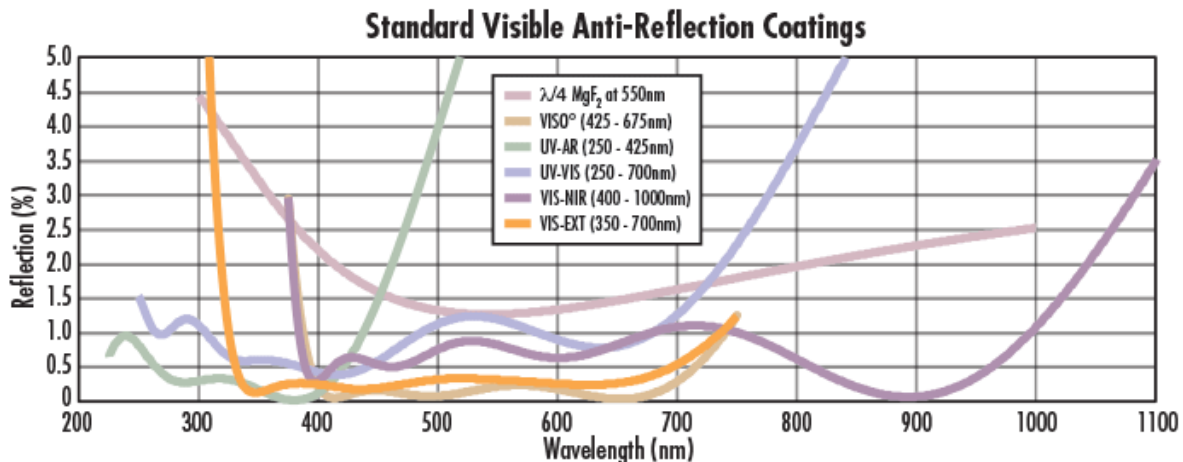


Figure 5.7. Standard antireflection coatings for the visible wavelength region which are offered by Edmund Optics [26]

For the ghost analysis of the folded fisheye lens the author has assumed that the Vis0° coating will be used, where all optical surfaces with antireflection coatings will assume to have a reflectance of 0.4%.

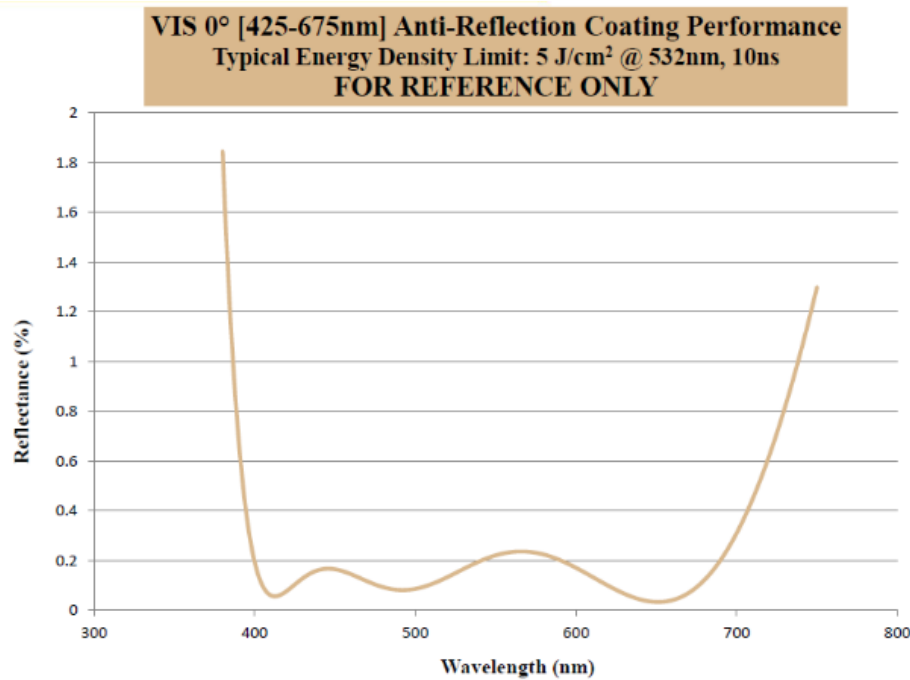


Figure 5.8. Reflectance versus Wavelength for the Vis0° antireflection coating [26]

The folded fisheye lens is designed to operate in the 450nm to 650nm wavelength range, per the ultraviolet long pass filter and infrared short pass filters which were selected in Chapter 3. It is common to deposit both components into one complex multilayer filter which combines the properties of the long pass and short pass filters into one broadband-pass filter [Fig. 5.9] or what is commonly referred to as a UV/IR-cut filter in camera applications [27]. This UV/IR-cut coating can be coated on a lens element surface in the lens assembly to block ultraviolet and infrared radiation from transmitting to the CMOS sensor.

The standard reflective UV-cut filters and IR-cut filters in Edmund Optics' catalogue have average reflectance of 5% in the visible transmission region while reflecting what is assumed to be 100% of the light in the cut off regions [Fig. 5.10] [28]. When these are combined into a single UV/IR-cut filter, the reflectance for ghost analysis purposes will be assumed to be 5%.

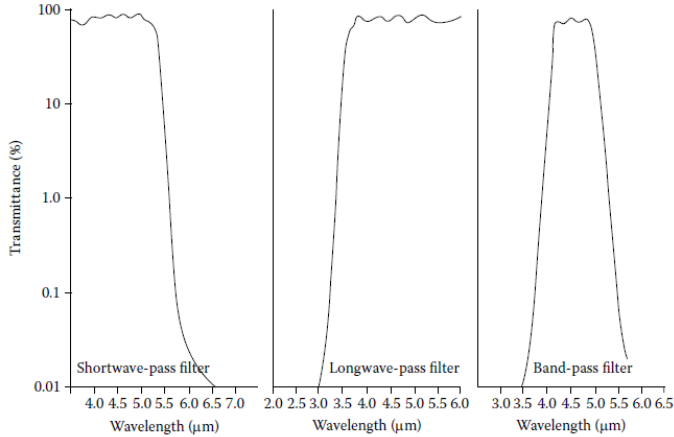


Figure 5.9. Demonstration of ultraviolet long-pass filter and infrared short-pass filter being combined into one band-pass filter [28]

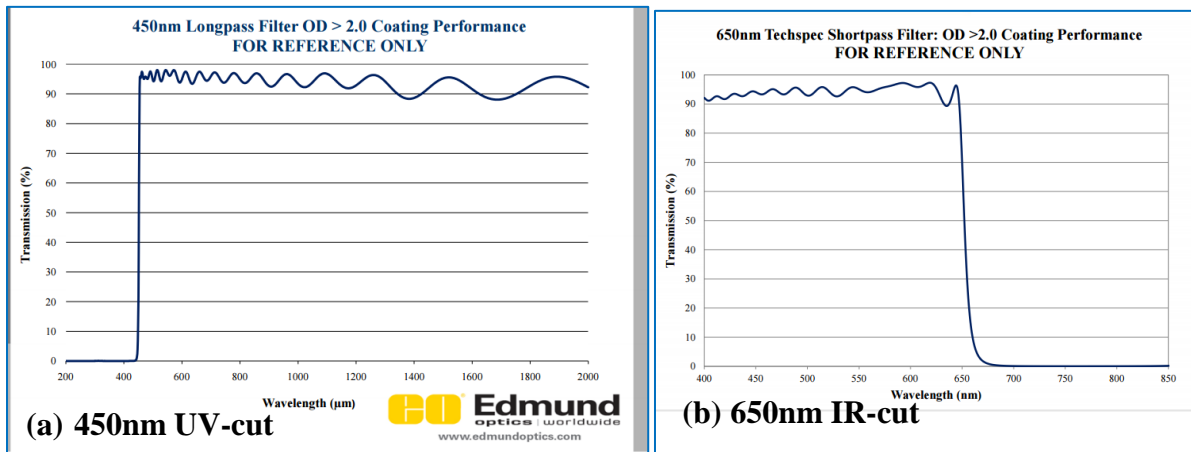


Figure 5.10. Transmission vs wavelength plots for (a) UV-Cut Filter and (b) IR-cut Filter

To conclude this chapter, there are several assumptions that must be made while the author is analyzing the stray light performance of the folded fisheye lens; to simplify the simulation of each optical coating used in the design, the author has assumed 4% reflectance for uncoated optical surfaces, 0.4% reflectance for optical surfaces with antireflection coatings, and 5% reflectance for the surface which will be coated with a UV/IR-cut filter. The reflectance for each of these coatings is assumed to be uniform for all wavelengths; Chapter 5.3.2 describes in more detail how these coating properties are configured in FRED when performing the ghost analysis.

5.3 Ghost Analysis Process in FRED

Ghosts images are simulated with non-sequential optical design software such as FRED (Photon Engineering), LightTools (Synopsys), or ASAP (Breault Research Organization). In these programs, an optical ray can be thought of as splitting into a ‘parent’ and ‘child’ ray each time that it interacts with a surface, where the energy is distributed between the parent and child ray according to the reflectance of that surface. When a child ray interacts with a surface, it is split into a grand-child ray, and so forth. In theory, there are an unlimited number of times that a ray can be split in this manner; because of this, it is common to limit the number of splits that can happen for all rays in the ray tracing software. Due to the efficiency low reflectance of optical surfaces and AR-coatings, one is generally only concerned with the 2nd order ghost paths. At most, the ghost ray which experiences two reflections from AR-coated surfaces will contain 0.16% of the energy of the original ray.

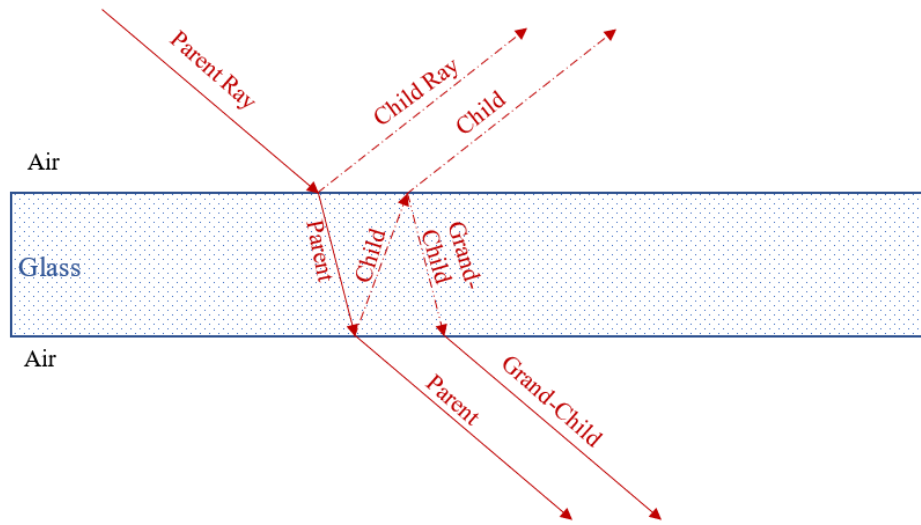


Figure 5.11. Ray splitting at an optical surface

By utilizing the ray history file in these non-sequential optical design software, the optical designer can analyze all of these ghost ray paths that are present in the system. In addition, color

image plots of the ghost image of all rays that end at the image plane can be simulated to understand how the ghost images will appear, and the irradiance of these ghosts can be studied. Through this analysis, the author determines which surface will be the most optimal location for the UV/IR-cut filter in this folded fisheye lens to optimize the stray light performance.

The author has chosen to use FRED for the analysis of the folded fisheye lens. To begin the analysis, the folded fisheye lens' Zemax prescription was imported and converted into a FRED file. The 'Add analysis surface to image surface' box is checked when importing the optical prescription, and the rest of the default settings are left as-is. FRED builds each lens element per the geometry and glass materials defined in the Zemax file, and automatically adds edges and bevels to each element. After importing the lens, a few changes were made. First, the aperture is set to have a finite diameter such that it halts all rays which don't pass through the clear aperture; This modification is done by going into the aperture surface settings in FRED and setting the 'Trimming Volume Outer Boundary' to have a 5mm semi-diameter radius, and the 'Trimming Volume Inner Hole' is set to the stop diameter in our Zemax file [Fig 5.12]. In the coating/ray control tab the raytrace control is set to 'HALT ALL,' which simulates 100% absorption for any ray which interacts with this aperture surface.

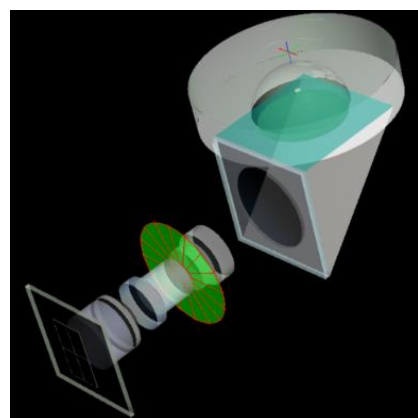


Figure 5.12. Defining the aperture stop in FRED to have an outer diameter of 10mm

5.3.1 Coating and Raytrace Control Settings

The FRED design program has four default optical coatings and four different raytrace commands that can be assigned to each surface. The ray commands include ‘Transmit,’ ‘Reflect,’ ‘Halt All,’ and ‘Allow All.’ The ‘Transmit’ coating tells the surface to transmit 100% of the ray, ‘Reflect’ reflects 100% of the ray, ‘Halt All’ stops the ray from transmitting or reflecting, and ‘Allow All’ tells the ray to split according to the reflectance of the surface. The default coatings include ‘Transmit,’ ‘Reflect,’ ‘Absorb,’ and ‘Standard Coating.’ ‘Transmit’ tells the surface to transmit 100% of the ray, ‘Reflect’ simulates a perfect mirrored surface with 100% reflection, ‘Absorb’ sets 100% absorption on the surface, and ‘Standard Coating’ places a reflectance of 4% and transmission of 96% on the surface. The user can define their own optical coatings where the reflection and transmission percentages are manually input to the program.

By default, FRED gives all optical surfaces the ray command “Transmit” and the optical coating “Transmit.” This combination results in 100% transmission causing no reflection to occur, and only the specular sequential ray path will be traced. To analyze the ghosts of this lens system, the ray command for all optical surfaces must be set to “Allow All,” and the optical coating properties must be defined to control the reflection and transmission through the optical assembly.

Two additional coatings were created for this analysis be defined including a simple AR-coating which has 0.4% reflection and 99.6% transmission, and a UV/IR-cut coating which has 5% reflection and 95% transmission. The author does not have access to the coating prescriptions for the Vis0°, 450nm long-pass filter, or 650nm short-pass filter from Edmund Optics; thus, FRED’s simple coatings are utilized in this analysis where all wavelengths are reflected uniformly at the reflectance and transmissivity values which the user defines. An example of this definition for the AR-coating is presented in Fig. 5.13.

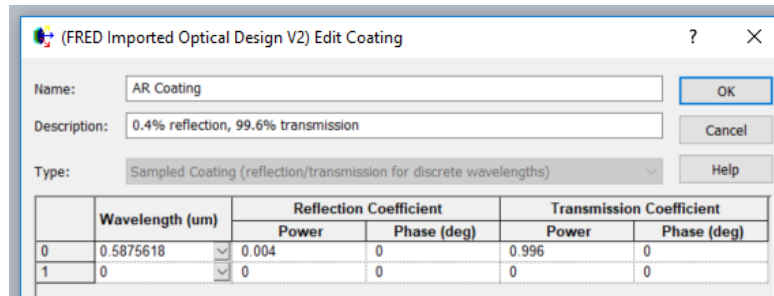


Figure 5.13. Simple Coating definition in FRED for the antireflection coating which has 0.4% reflection and 99.6% transmission

For now, the author is assuming that the prism and sensor cover glass would be too expensive to AR-coat, and analyzes the stray light performance for this scenario. These surfaces have a reflectance of 4% with 96% transmission. For the initial ghost analysis of the folded fisheye lens design, the author has set the coating and raytrace controls to the following configuration:

1. All lens element surfaces are set to have the coating type “AR-Coating” and raytrace control “Allow All” which will reflect 0.4% of the light and transmit the other 99.6% per every lens-surface interaction.
2. The prism’s optical surfaces and the flat sensor cover glass are set to have the “Standard Coating” and raytrace control “Allow All” which will reflect 4% of the light and transmit the other 96% per every lens-surface interaction.
3. All lens-edges and the aperture stop are set to have coating type “Absorb” and raytrace control “Halt All.” This will ignore any effects from light scattering off of the lens edges and simulate 100% absorption on the aperture stop.
4. The prism reflecting face is set to have coating type “Reflect”, and raytrace control “Reflect All.” This ensures 100% reflection at the total internal reflection interface.

5.3.2 Optical Source Configuration

The optical sources which will be used in our analysis must now be defined. The author created detailed optical sources for each for field height ranging from 0 degree to 100 degree half fields of view, where the goal is for each optical source to simulate what the sun would appear as in the sky as seen from that field angle. The sources are set to follow the solar spectrum per blackbody radiation with the temperature is set to 5780 Kelvin and wavelengths ranging from 0.38 μm to 0.75 μm and has power units in Watts [Fig. 5.14].

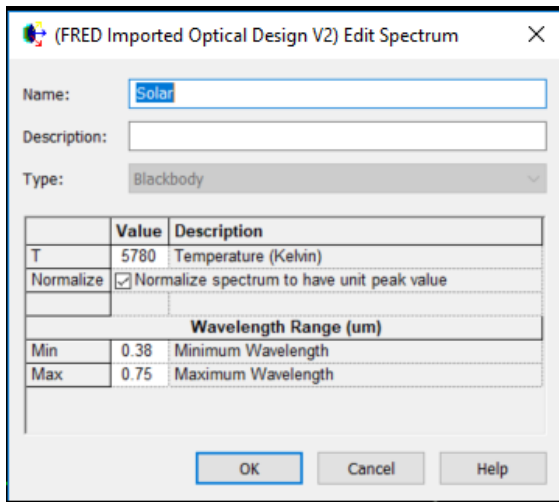


Figure 5.14. Simple blackbody solar spectrum definition in FRED

Each field is defined to originate 100,000mm away from the first lens element, and the rays are aimed at the entrance pupil location for the field which is being traced. The diameter of each ray bundle is set to fill the clear aperture of the first lens element to ensure that the aperture stop of the lens is always filled, in addition to simulating the way that light from the sun would interact with this lens in a real-world setting. When aiming the rays, the author utilizes the ‘sines of two angles’ to define the ray propagation direction, where the ‘b’ angle is used to define the angle along the y-axis which the author will use to define the field of view for that configuration. To simulate the solid angle subtended by the sun, the field type ‘random angles into an angular range,’

with X and Y semidiameter set to 0.25° to simulate the solid angle subtended by the sun is used [Fig. 5.15].

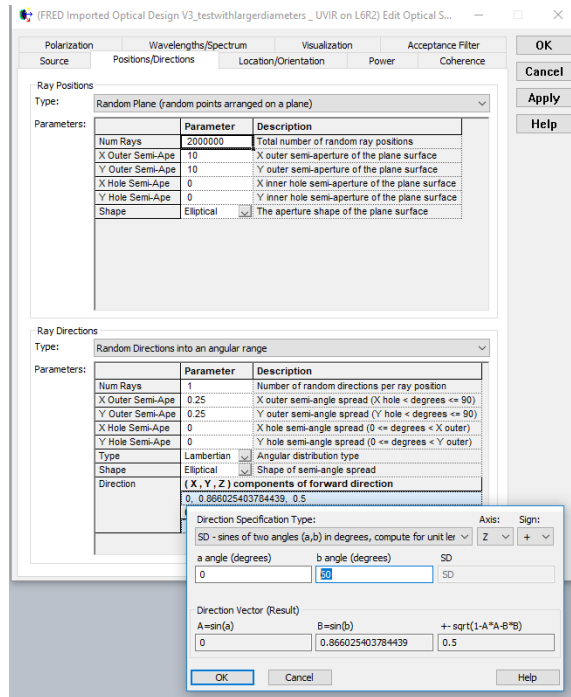


Figure 5.15. Optical Source Settings example for 60-degree field

The entrance pupil position, or ray aiming location in FRED, for each field height is defined in the Locations/Orientation tab. As discussed in Chapter 2.4 fisheye lenses commonly have large amounts of pupil aberration which results in the entrance pupil changing size and location as rays are traced off-axis. In addition to the entrance pupil position translating along the optical axis, the size and shape of the pupil is changing as well. In the author's experience, an efficient way to ensure that the pupil is filled is to first aim the ray bundle at the entrance pupil location for that ray height, and set the ray bundle diameter to be equal to the clear aperture of the first lens element. This more accurately emulates the way that light from the sun would interact with this lens in a real-world setting and ensures that the aperture stop of the lens is always filled.

The entrance pupil position versus field of view of the folded fisheye lens was measured in Chapter 4.5.3; To simplify the visualization of the shift, the entrance pupil locations for the 30-degree field, 60-degree field, and 90-degree fields are shown [Fig. 5.16]. These entrance pupil position values will be used while configuring the optical sources in FRED by aiming the bundle of rays from the source at the entrance pupil location for each field. The values listed [Table 5.1] are referenced from the first surface of the first element, and a positive value indicates a shift towards the image plane.

Half FOV (degrees)	E.P. Location (mm)
0	5.295
10	5.235
20	5.125
30	4.935
40	4.658
50	4.278
60	3.776
70	3.125
80	2.295
90	1.266
92.5	0.931
95	0.613

Table 5.1 Entrance pupil location as a function of image height for the folded fisheye lens

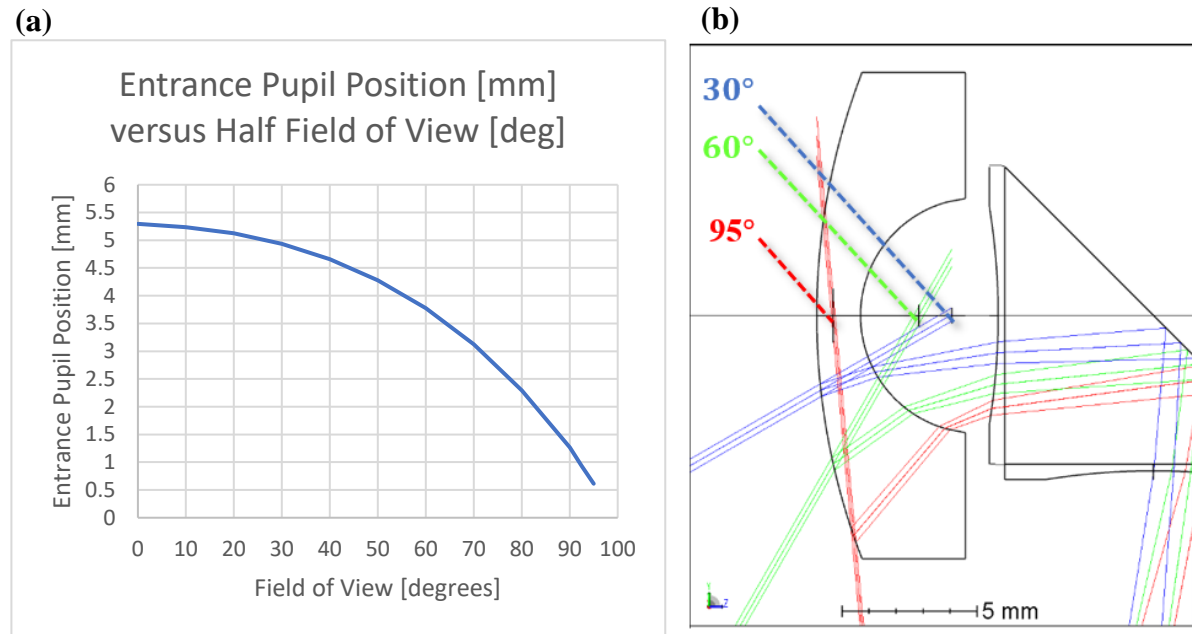


Figure 5.16. Entrance Pupil Position vs Image Height (a) plot and (b) visualization

To manually aim the rays for each field height, the entrance pupil location is defined as a Z-position shift in locations/orientations tab is utilized in the optical source settings. This process was repeated for each field height ranging from 0 to 100⁰. In each case, the field of view is changed in the Positions/Directions tab, and the entrance pupil position for that field height is defined in the Locations/Orientation tab [Fig. 5.17].

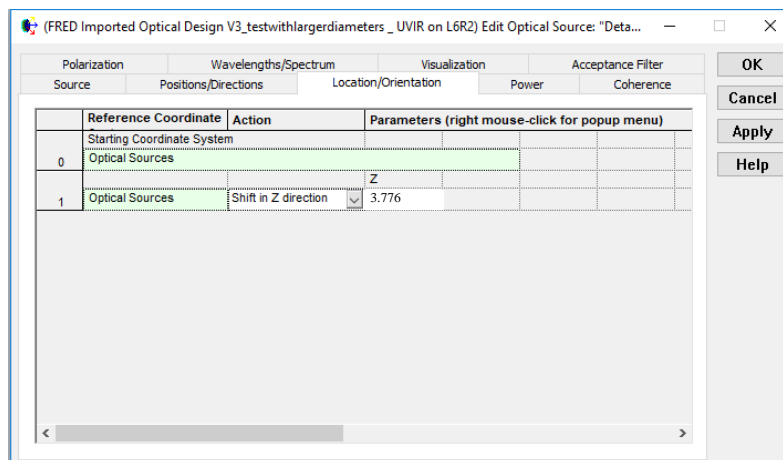


Figure 5.17. Manual ray aiming via the location/orientation tab in optical source settings

To ensure that the first lens element is fully filled, the ray bundle width is set to a 10mm semidiameter for all fields. The entrance pupil diameter of the folded fisheye lens on-axis is 0.46mm, and it grows significantly as rays are traced off axis; because of this, many rays will be clipped by the aperture stop when tracing on-axis, and fewer rays will be clipped with higher field angles. This presents a challenge to the optical designer, where either more rays are required to be traced for the lower field heights to obtain the same ray density at the image plane as the higher field heights. An example of a color image plot from the 30-degree field ghosts in the folded fisheye lens is shown in Fig. 5.18, where the image on the left had 500,000 rays traced, and the image on the right had 5,000,000 rays traced; as shown, a higher ray density at the image plane produces favorable results and allows the designer to differentiate between optical ghost images much more clearly.

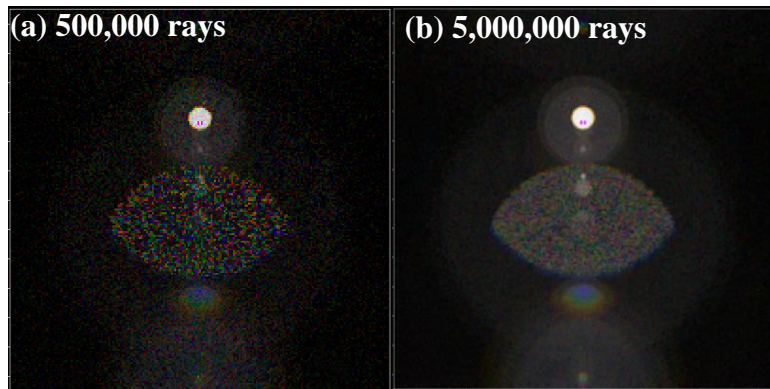
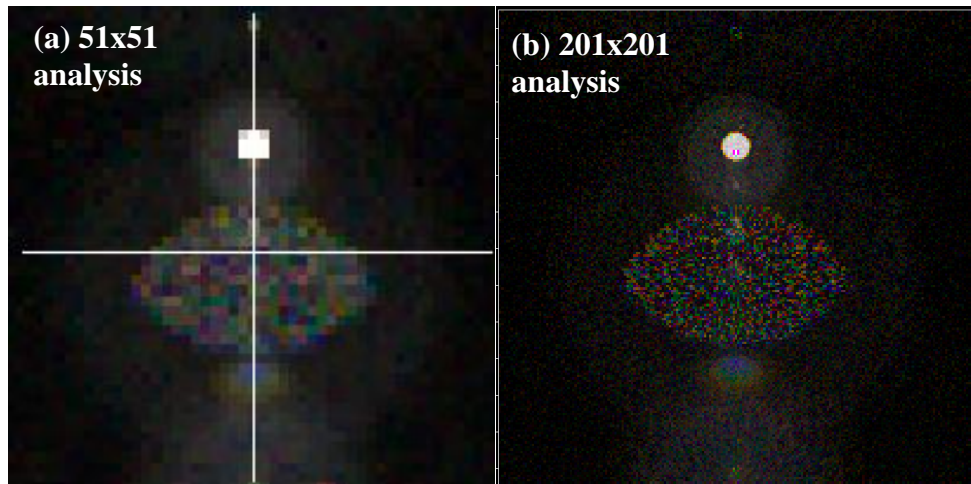


Figure 5.18. Color Image Plot of 30-degree field as a function of the numbers of rays traced. (a) 500,000 rays traced (b) 5,000,000 rays traced

Unfortunately, the amount of time that it takes to trace rays in the non-sequential design software is proportional to the number of rays being traced and the number of times that each ray is split. In this analysis, 2 million rays are initially defined for each field height and adjusted until the ray density in the color image plots are the same across all fields.

The size of the analysis surface is set to the vertical dimension of the AR0237 CMOS image sensor, which the full image circle will lie within. The sampling rate defined in the Analysis Surface will also play a role in the ray density which is required to be at the image plane. The author has chosen to set a sampling rate of 201 x 201 divisions in the image plane for higher quality ghost images [Fig. 5.20] and 51 x 51 for lower quality ghost images. While performing quick comparisons or setting up a new optical source, the author traces fewer rays while using analysis surfaces set to 51 x 51 divisions to allow for a quicker analysis. Fig. 5.19 demonstrates the color image plot obtained when 500,000 rays are traced at the 30-degree field and compares the results between an analysis surface set to a 51x51 grid versus a 201x201 grid. With the 201x201 sampling, the color image plot appears under-sampled; however, the results are sufficient when using a 51x51 grid. In general, a lower sampling frequency on the analysis surface requires fewer rays to be traced, thereby reducing the computation time required for each analysis.



**Figure 5.19. Analysis surface sampling frequency differences. (a) 51 x 51 sampling
(b) 201 x 201 sampling**

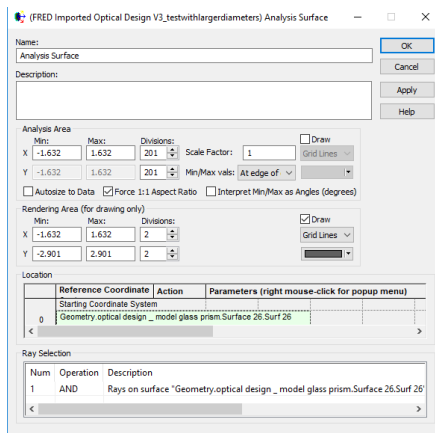


Figure 5.20. Analysis Surface Settings showing a sampling division of 201 x 201

Once the author was confident in the results, higher resolution images are obtained by tracing more rays with a higher sampling frequency on the analysis surface for further analysis.

5.3.3 Ghost Image and Ray Path History Analysis Process

While performing the ghost analysis, only one field source will be used at a time; This is easily done by right clicking on fields and selecting ‘Traceable’ for only the field which will be analyzed. To gather information about the ray paths and power associated with each path, the author utilizes the Advanced Ray Trace tool in FRED which saves all the ray history file and all ray paths for the stray light analysis by selecting the ‘Create/Use Ray History File,’ and ‘Determine Ray Paths’ check boxes before the ray trace. Another option in the advanced ray trace is to trace every n'th ray in the visualization window; allowing FRED to draw the rays while it runs the analysis shows how the light reflects, scatters, and propagates through the optical system. 2000 rays were drawn for the 30-degree optical source field to generate the 3D schematic shown in Fig. 5.21, which shows a significant amount of stray light present in this system which lies outside of the sequential specular path. Many of the rays are shown to be halted by the aperture stop, where only the rays which would pass through the clear aperture of the stop make it through to the image plane.

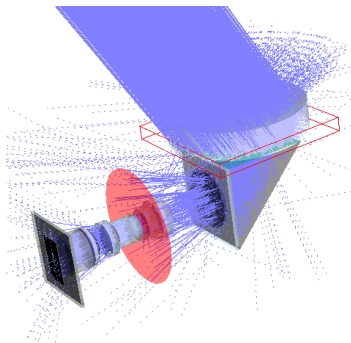


Figure 5.21. Stray light simulation for a 30-degree field in a folded fisheye lens

Using the Color Image Analysis tool provided in the FRED software provides an estimate of what the ghosts will subjectively appear as for the field height which was traced. To make the ghosts easier to visualize, the image brightness can be increased up to a maximum value of 10000. The color image plot tool shown in Fig. 5.22 shows what the image would look like for a 30-degree field height, the grayscale power per pixel across the X and Y crosshair shown in the image, and a chromaticity plot to analyze the color of the pixel that is in the center of the crosshair.

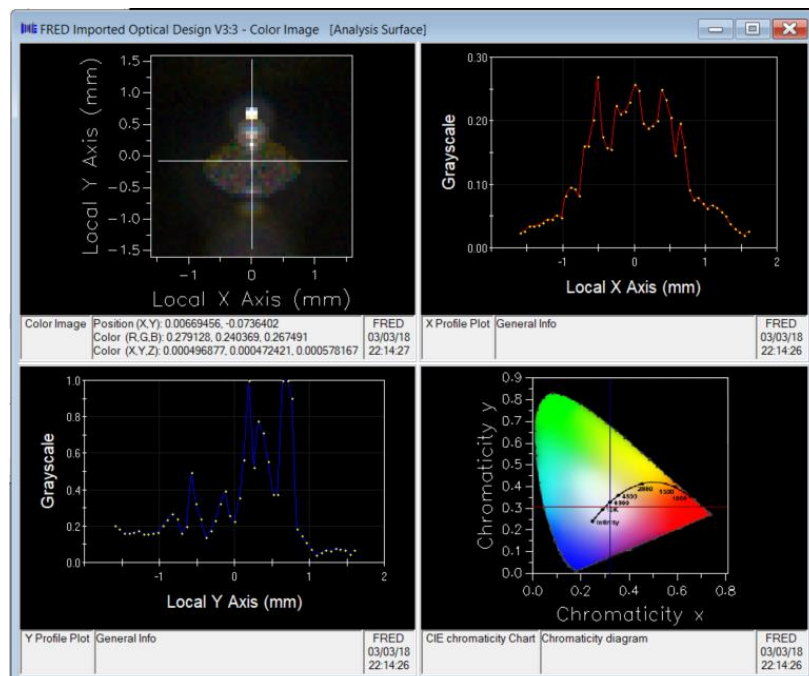


Figure 5.22. Color image plot simulation for 30-degree field in the folded fisheye lens

To understand the irradiance of the stray light on the image plane for that field height, the Irradiance Spread Function Analysis is utilized in FRED. This tool plots the irradiance across the entire image, which allows the optical designer to study how ‘bright’ a ghost will appear in the image more quantitatively than can be done with the color image plot. However, the scale on these plots are often skewed because the image of the sun contains a much higher irradiance than the ghosts in the image [Fig. 5.23]. To mitigate this, a log-scale can be applied to enable to help visualize the difference in irradiance between ghosts; most often, the log scale is applied with a floor ranging from -9 to -6 depending on the field to visualize the ghosts most easily. The irradiance of each ghost can then be determined by moving the crosshair around the image. It is common for the irradiance of a ghost is reported in relation to the irradiance of the sun in the same image, where the irradiance of the sun is normalized to a value of 1.

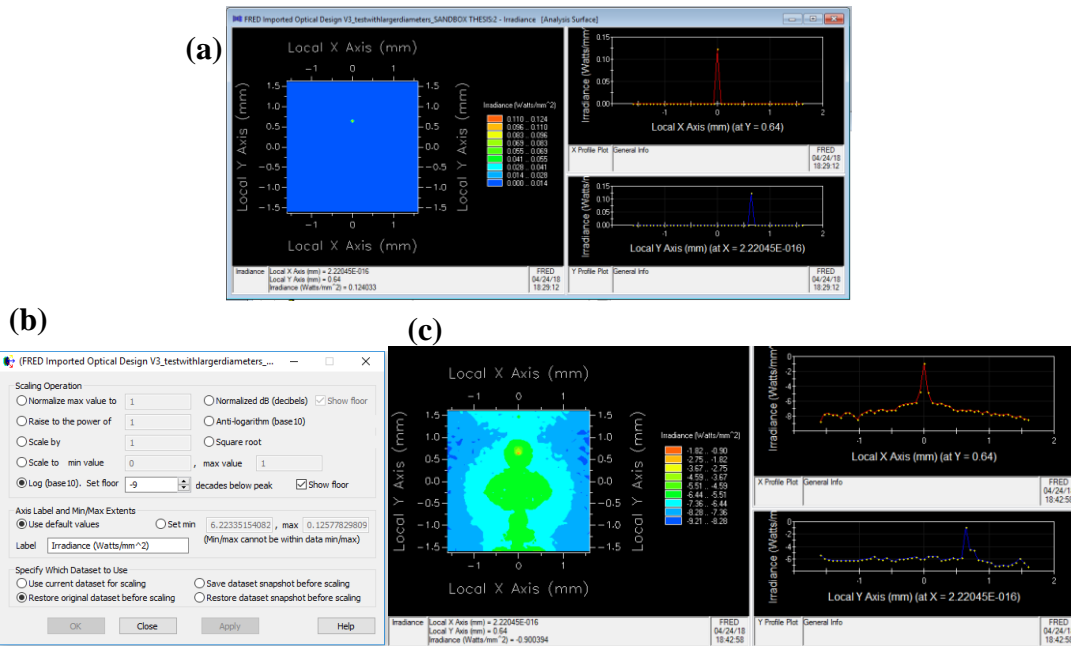


Figure 5.23. Irradiance Spread Analysis for 30-degree field in the folded fisheye lens.

- (a) Irradiance plot before log scale is applied**
- (b) Settings used to scale the plot**
- (c) Irradiance plot after log scale is applied with a floor set to -9.**

To learn more about what surfaces are causing each ghost, the Raytrace Paths Report and Stray Light Report are used in FRED. With total internal reflection occurring on the prism interface, the author is mainly focused on ray paths which have experienced 3 total reflections, of which two are ghost reflections. Sorting the ray path list to only show rays which have the image surface as their final surface interaction, while also having 3 specular reflections enables the author to isolate only the ghost paths from the previous raytrace. This list is then sorted in order of total power on the image plane, which sorts the list in an approximate order of the ray paths which cause the brightest ghost images. This list is approximate, because it does not show the irradiance of the ghost, only the total power; For example, ghosts with large surface area often show up near the top of this list even though they exhibit low irradiance on the image plane. Nonetheless, analyzing this ray path list can provide information about which surfaces contribute to each ghost [Fig. 5.24]

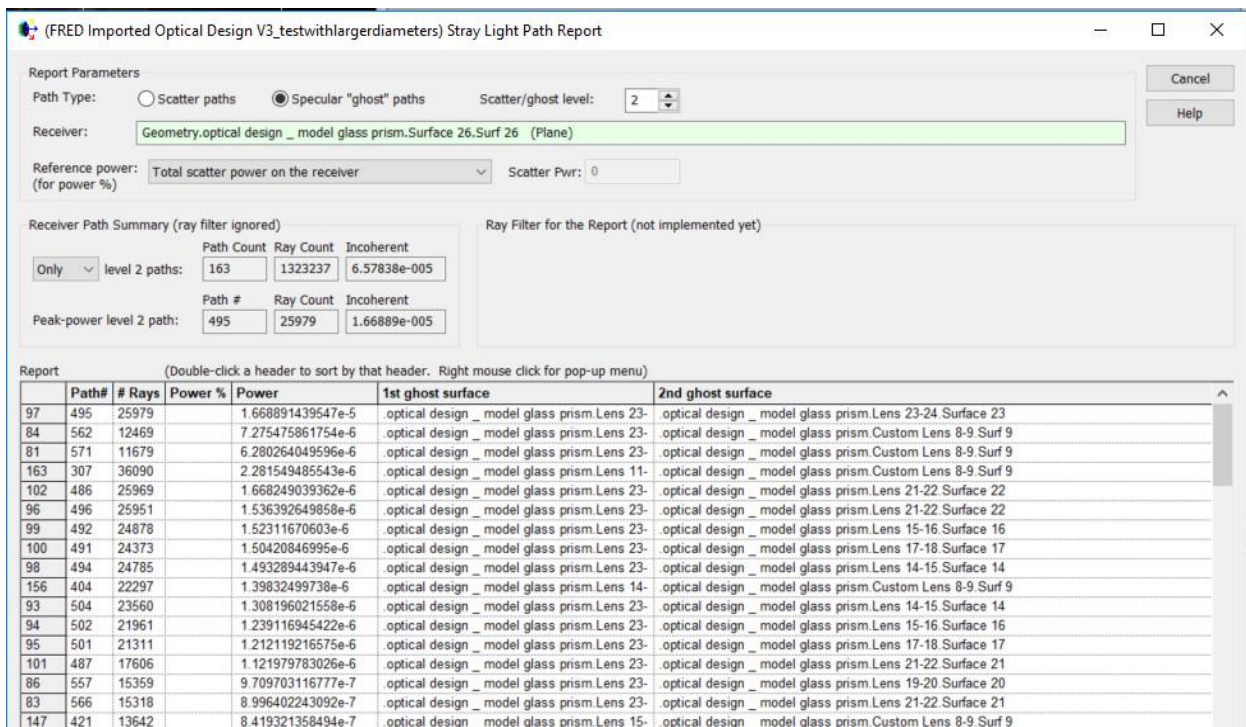


Figure 5.24. Stray Light Report showing only ghosts present on the image plane, sorted by total power contained in each ray path

To analyze which ghost is be associated with a particular ray path, another analysis surface must be defined which only shows the rays which land on the image plane surface *and* follow a specific ray path that the user defines. In this example, an analysis surface which isolates only the rays from path 505 is configured at the image plane [Fig. 5.25]. By generating another color image plot or irradiance analysis with this new analysis surface, a color image plot of the only the rays associated with path 505 will be shown. The color image and irradiance plots of this ray path compared to the original color image plot can be seen in Fig. 5.25, demonstrating that path 505 in this case is associated with the football-shaped ghost in the image.

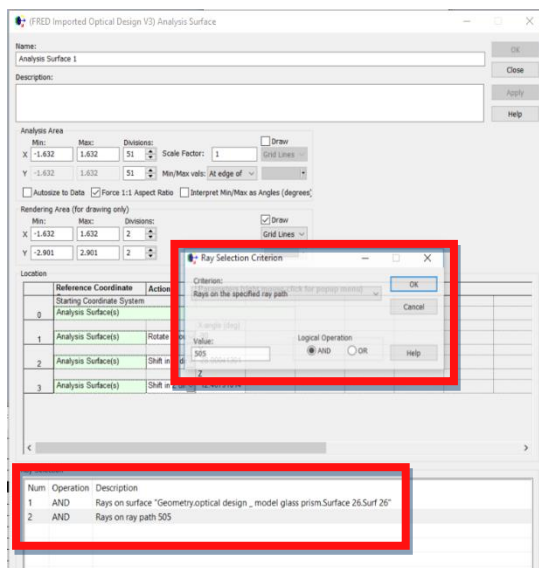


Figure 5.25. Analysis Surface defined to only include rays on path 505

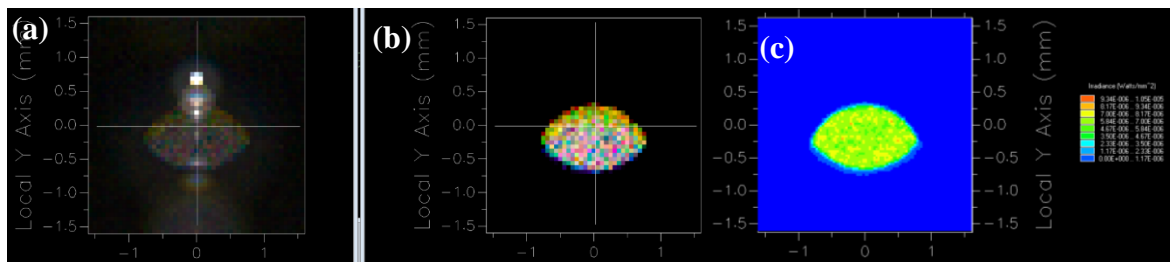


Figure 5.26. (a) Full color image plot for all rays, (b) Color image plot which only includes ray path 505, (c) Irradiance plot which only includes ray path 505

Right-clicking on ray path 505 in the Raytrace Path Summaries and selecting “Redraw every n'th ray” will redraw only that particular ray path in the 3D layout which helps to visualize how the ghost path propagates. Redrawing path 505 such that only one ray is traced, it can be seen that the football ghost comes from a reflection off of the sensor cover glass and the closest prism face [Fig. 5.27]. Both surfaces are set to have standard 4% reflection coatings, so it is not surprising that this path creates one of the ghosts with the highest power

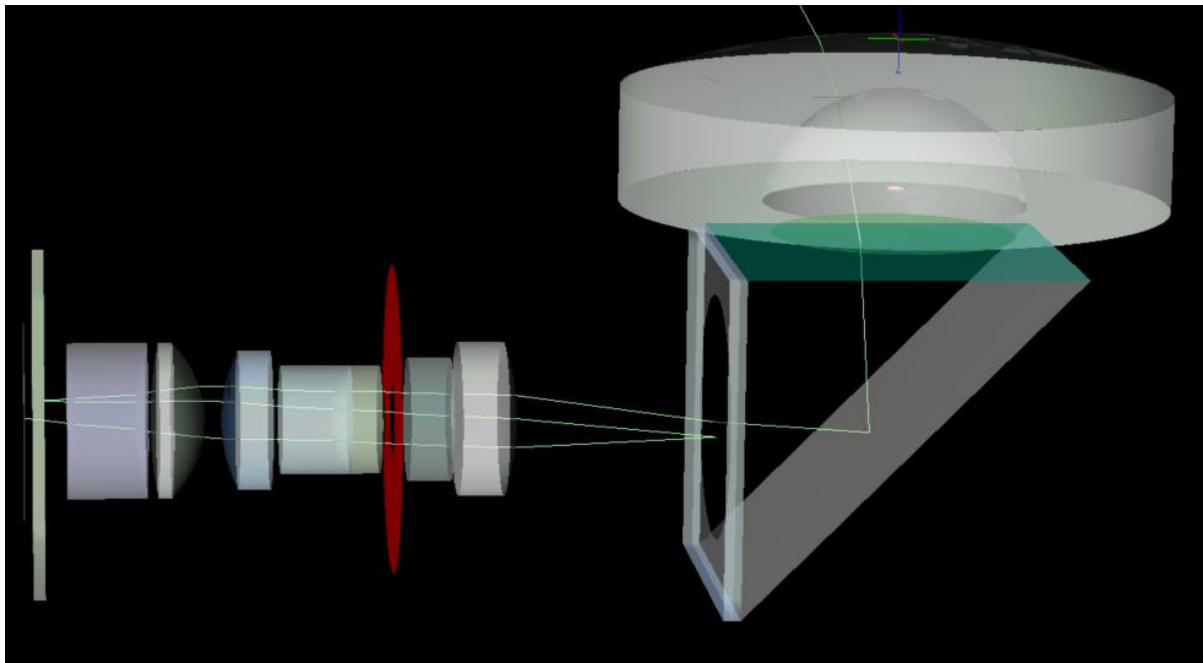


Figure 5.27. 3D view of ray path 505. This shows that the football shaped ghost comes from reflections off of the sensor cover glass and the prism.

Continuing with this method of analyzing the ray path history for the ghost paths which contain the most power allows the optical designer to analyze the origin and irradiance associated with each ghost. This information can be useful in not only understanding the stray light and ghost performance that can be expected in an imaging lens, but will also allow the optical designer to understand which surfaces are the most optimal locations to place optical coatings.

5.4 Initial Ghost Analysis (Color Image Plots)

Using the method described in Chapter 5.3, color image plots of the ghosts in the folded fisheye lens are presented from 0-degree to 100-degree field heights [Fig. 5.28], and a thorough ghost analysis is performed on the 30-degree field and 80-degree field heights sources to determine which surfaces contribute to the 10 ghosts that exhibit the highest irradiance in this lens. With the coating property assumptions listed in Table 5.2, the ghost performance of the folded fisheye lens suffers from a higher quantity of ghosts at the lower image height fields than at the higher image heights; in addition the ghosts present in low image heights tend to be much larger in size, where all of the ghosts present in the fields past 60 degrees are small in comparison.

Surfaces	Coating	Raytrace Control
Optical Elements	0.4% Reflectance 99.6% Transmission	Allow All
Prism and Sensor Cover Glass	4% Reflectance 96% Transmission	Allow All
Lens Edges and Aperture Stop	100% Absorption	Halt All
Prism TIR Surface	100% Reflectance	Reflect All

Table 5.2. Optical coating property assumptions used in generating the color image ghost analysis plots shown in Fig. 5.28

5.4.1 Color image plots from 0 degrees to 100 degrees

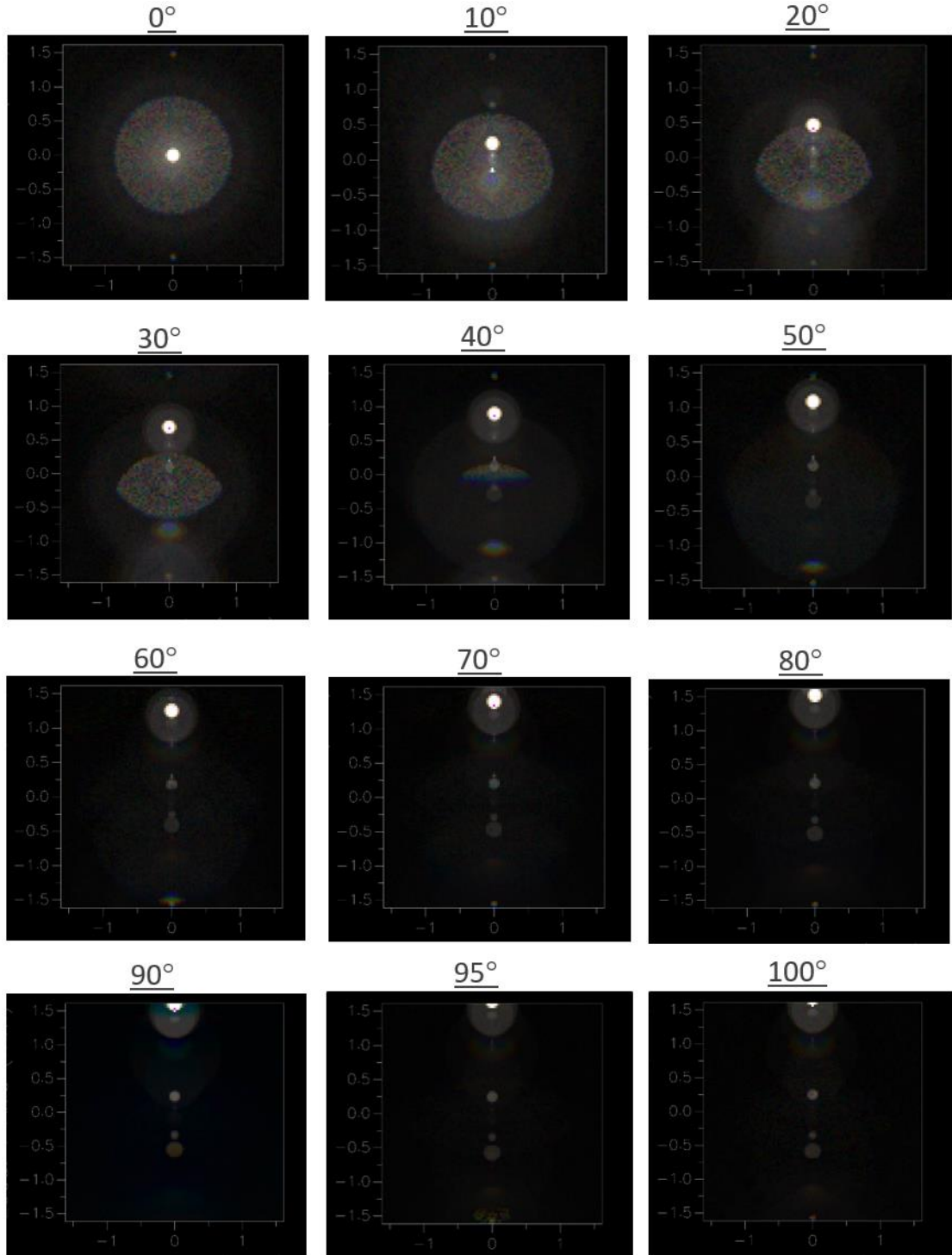


Figure 5.28. Ghost image color image plots for the folded fisheye lens before the highly reflective UV/IR-cut filter location is introduced to the optical assembly

5.4.2 Prominent ray path ghost analysis

In this chapter, the author determines which surfaces contribute to the most prominent ghost ray paths that are present in the folded fisheye lens, so that those surfaces can be avoided when choosing where to place the highly reflective UV/IR-cut filter. All ghosts which are present in the system can be seen in the 30-degree and 80-degree fields, thus, these two source angles have been chosen for more in-depth ghost analysis'. For simplicity, the ten ghosts which exhibit the highest irradiance across the field of view have been numbered 1 through 10, and are shown in Fig. 5.29.

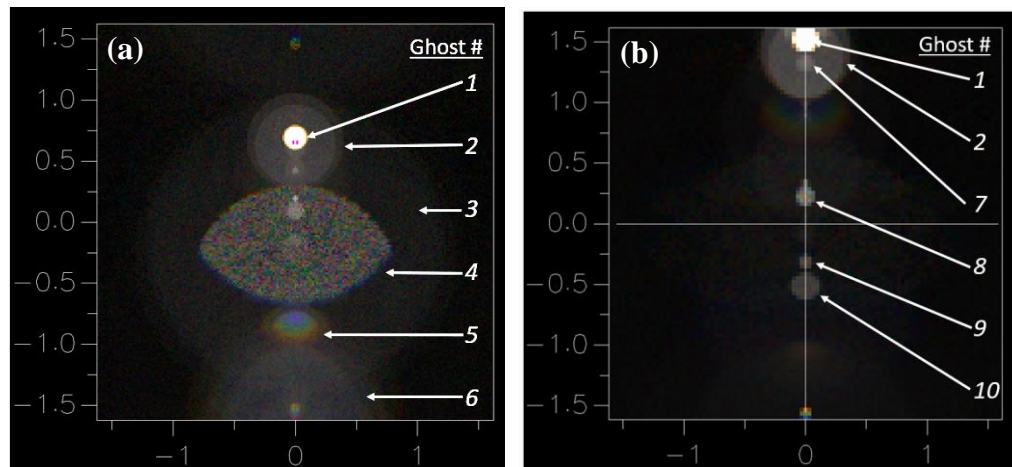


Figure 5.29. Ghost Images #1 through #10 in (a) 30-degree field and (b) 80-degree field

A handful of these ghosts appear as a double ghost image where there are two very similar ghosts which are on top of each other, such as ghost #2, #5, and #6. In the case of the folded fisheye lens, these ‘double’ ghosts originate from reflections off the sensor cover glass. The sensor cover glass is flat and very thin, which results in two ghosts which have almost identical ray paths; one ghost comes from a reflection off the top surface off the cover glass, and a second ghost which comes from the bottom surface of the cover glass. For simplicity, and because these double ghosts are always coincident, the author does not split these ghosts into two separate ghosts and refers to them as a single ghost which originates from the sensor cover glass.

From the six ghosts which are shown in the 30-degree field [Fig. 5.29], the ghost which has the highest irradiance in the image across all field heights is ghost #1. This ghost is always directly on top of the image of the source, and has a peak irradiance of $2.10 \cdot 10^{-5} \frac{\text{W}}{\text{mm}^2}$ relative to the sun. The surfaces which this ghost originates from are the bottom of the sensor cover glass and a reflection off the top of the sensor cover glass [Fig. 5.30]. Ghost #2 comes from a reflection off the sensor cover glass and L8R2 [Fig. 5.31]. This ghost is a double image ghost, where two ghost images form on top of each other from the two surfaces of the sensor cover glass. The irradiance of both ghost images stacked on top of each other is $3.04 \cdot 10^{-7} \frac{\text{W}}{\text{mm}^2}$ in relation to the sun.

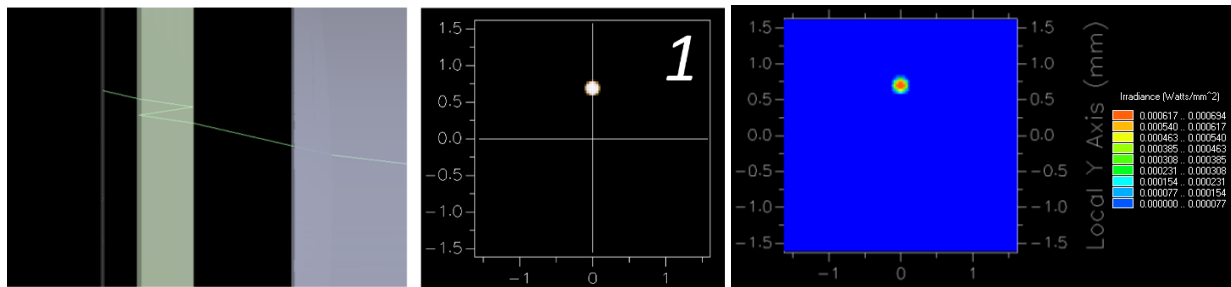


Figure 5.30. Ghost #1. (left) 3D Layout of ghost path, which originates from reflections off the sensor cover glass, (middle) color image plot, (right) irradiance spread

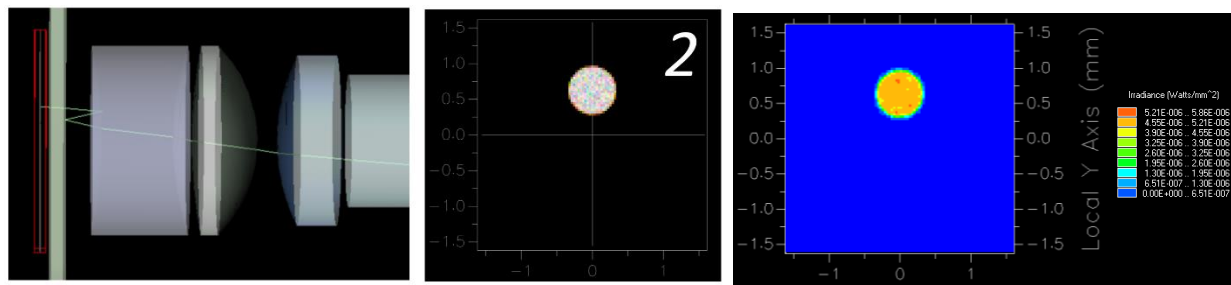


Figure 5.31. Ghost #2. (left) 3D Layout of ghost path, which originates from reflections off the sensor cover glass and L8R2, (middle) color image plot, (right) irradiance spread

Ghost #3 is an example of a ghost which shows up at the top of the stray light report due to the ghost path containing a lot of total power, but the size of the ghost is very large resulting in low irradiance. This ghost covers a significant portion of the image, which leads the author to believe that this ghost would cause a general reduction in contrast of the image as opposed to showing up as a bright ghost image. Ghost #3 has the lowest irradiance out of the ten brightest ghosts with a peak irradiance of $2.34 \cdot 10^{-8} \frac{W}{mm^2}$ in relation to the sun. The ray path which this ghost comes from is a reflection off L3R2 and the outermost spherical prism surface [Fig. 5.32]. Ghost #4, the large football shaped ghost which disappears around the 50-degree field height, also comes from a reflection off the same prism surface but with the first surface reflection coming from the sensor cover glass [Fig. 5.33]. The peak irradiance of this ghost is $6.03 \cdot 10^{-7} \frac{W}{mm^2}$ in relation to the sun.

The smaller football shaped ghost image, ghost #5, has the second highest irradiance in the system with a peak irradiance of $1.175 \cdot 10^{-6} \frac{W}{mm^2}$ while being a double ghost image [Fig. 5.34]; these ghosts comes from reflections off the sensor cover glass and L3R2. The final ghost seen in the 30-degree field is ghost #6 which appears at the bottom of the image with a peak irradiance of $1.48 \cdot 10^{-7} \frac{W}{mm^2}$. This ghost is also a double ghost image, with the ghosts coming from reflections off the sensor cover glass and L5R2 [Fig. 5.35].

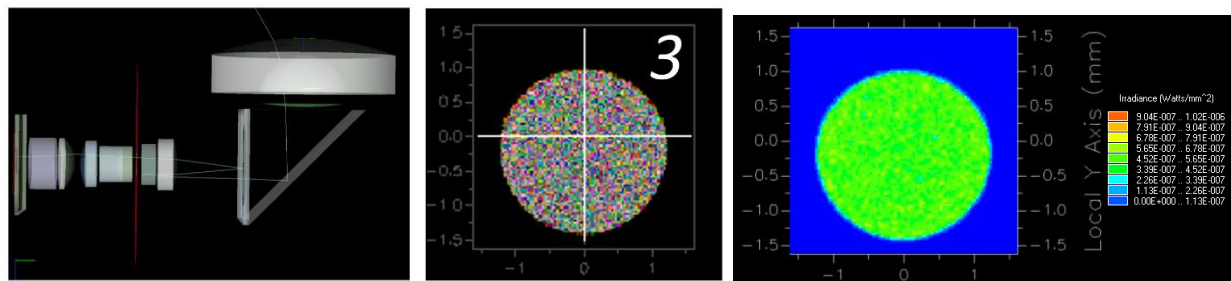


Figure 5.32. Ghost #3. (left) 3D Layout of ghost path, which originates from reflections off L3R2 and Prism R2, (middle) color image plot, (right) irradiance spread

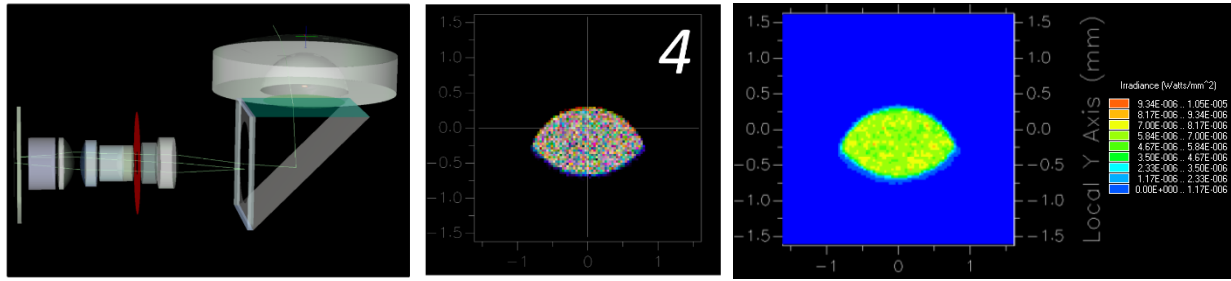


Figure 5.33. Ghost #4. (left) 3D Layout of ghost path, which originates from reflections off the sensor cover glass and Prism R2, (middle) color image plot, (right) irradiance spread

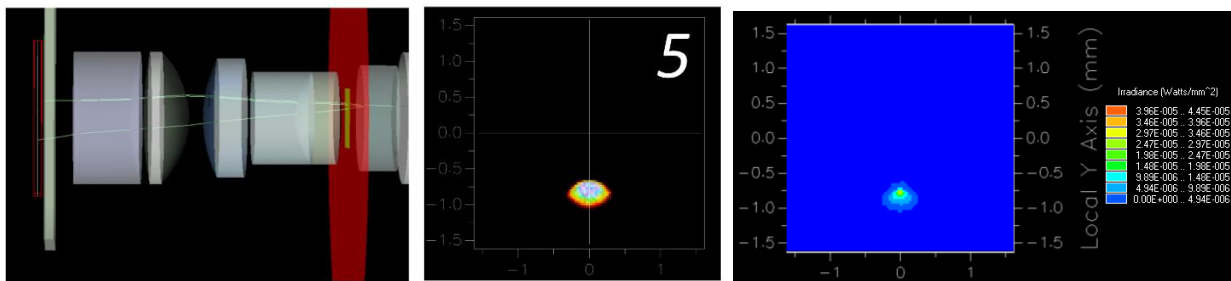


Figure 5.34. Ghost #5. (left) 3D Layout of ghost path, which originates from reflections off the sensor cover glass and L3R2, (middle) color image plot, (right) irradiance spread

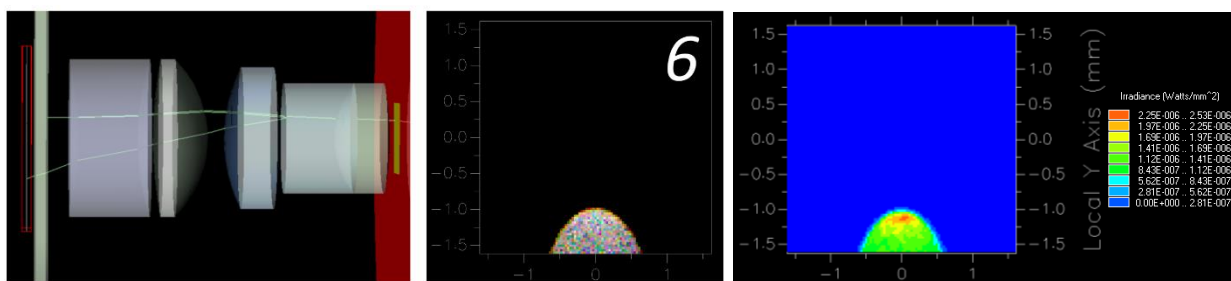


Figure 5.35. Ghost #6. (left) 3D Layout of ghost path, which originates from reflections off the sensor cover glass and L5R2, (middle) color image plot, (right) irradiance spread

Ghosts #1 and #2 are present in all field heights, including the 80-degree field height. The peak irradiance of Ghost #1 in relation to the sun in the 80-degree field height is $1.93 \cdot 10^{-5} \frac{W}{mm^2}$, which is very close to the peak irradiance of $2.10 \cdot 10^{-5} \frac{W}{mm^2}$ seen in the 30-degree field. The same holds for ghost #2, which has a peak irradiance of $2.99 \cdot 10^{-6} \frac{W}{mm^2}$ in the 80-degree field and

$3.04 \cdot 10^{-6} \frac{\text{W}}{\text{mm}^2}$ in the 30-degree field. The surfaces which contribute to these ghosts do not change [Fig. 5.36] [Fig. 5.37].

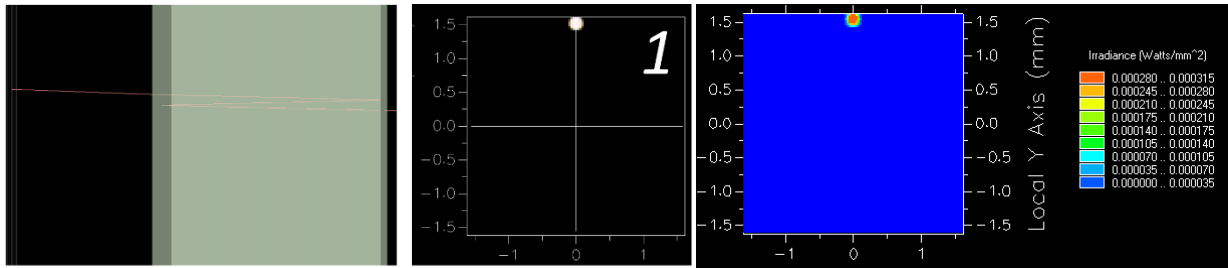


Figure 5.36. Ghost #1 (80-degree field). (left) 3D Layout of ghost path, which originates from reflections off the sensor cover glass, (middle) color image, (right) irradiance

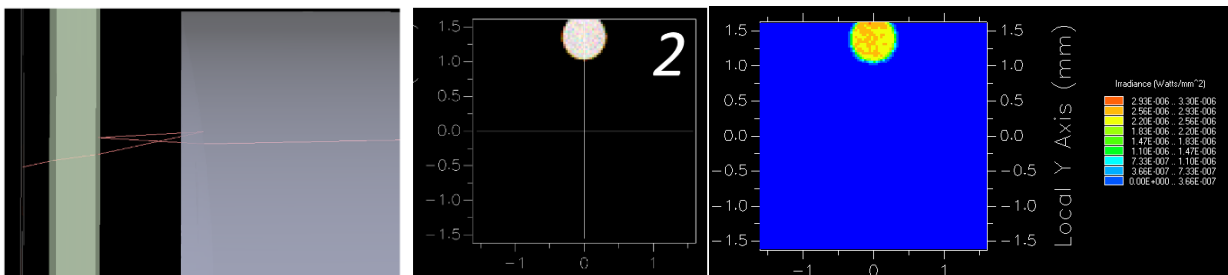


Figure 5.37. Ghost #2 (80-degree field). (left) 3D Layout of ghost path, which originates from the sensor cover glass and L8R2, (middle) color image, (right) irradiance

Near the top of the image in the 80-degree field, inside of ghost #2, is ghost #7 which is relatively small and has a peak irradiance of $3.68 \cdot 10^{-7} \frac{\text{W}}{\text{mm}^2}$ in relation to the sun. This ghost originates from reflections off L6R1 and L5R2 which are very close together. Ghost #8, which is the third brightest ghost in the system with a peak irradiance of $7.72 \cdot 10^{-7} \frac{\text{W}}{\text{mm}^2}$ in relation to the sun, has one of the more unexpected ghost ray paths in this lens. This ghost comes from reflections inside of the prism, where the rays reflect off the 2nd prism surface, back off of the TIR surface, then reflect from the 1st prism surface before propagating back through the lens. Ghosts #9 and #10 lie just beneath the center of the image for most field heights, and do not translate very far across the image with increasing field angle as many of the other ghosts seen in the folded fisheye

lens tend to do. Ghost #9 comes from a reflection off L2 and the 2nd prism surface with a peak irradiance of $2.72 \cdot 10^{-7} \frac{W}{mm^2}$ in relation to the sun. Ghost #10 is the only ghost which originates from the first lens element, and comes from reflections off the 1st prism surface and L1R2, with a peak irradiance of $1.79 \cdot 10^{-7} \frac{W}{mm^2}$ in relation to the sun.

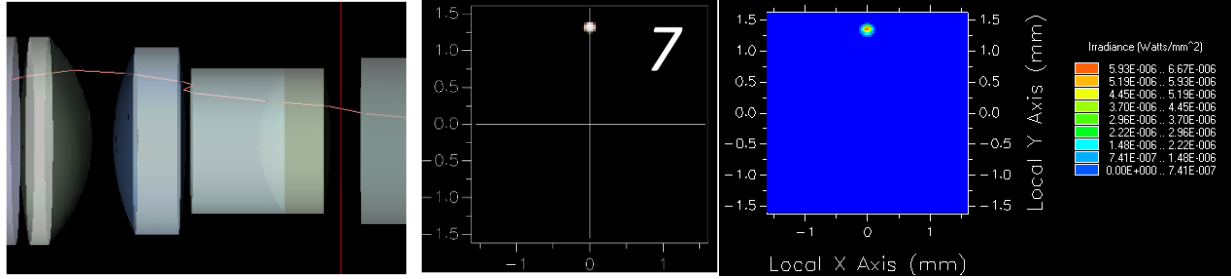


Figure 5.38. Ghost #7. (left) 3D Layout of ghost path, which originates from reflections off L6R1 and L5R2, (middle) color image plot, (right) irradiance spread

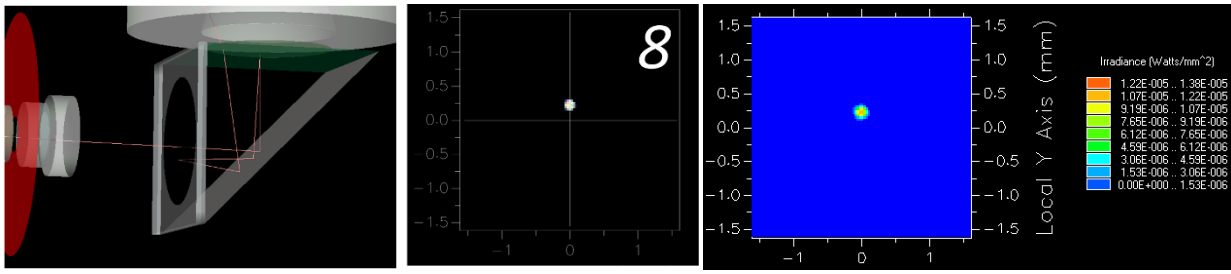


Figure 5.39. Ghost #8. (left) 3D Layout of ghost path, which originates from reflections off Prism R2 and Prism R1, (middle) color image plot, (right) irradiance spread

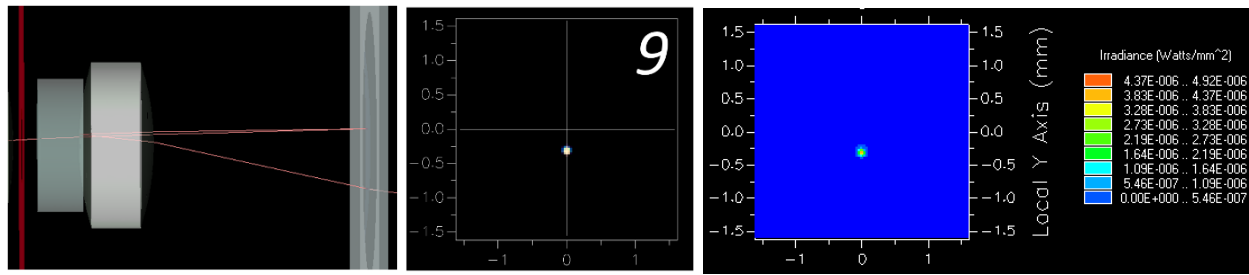


Figure 5.40. Ghost #9. (left) 3D Layout of ghost path, which originates from reflections off L2R1 and Prism R2, (middle) color image plot, (right) irradiance spread

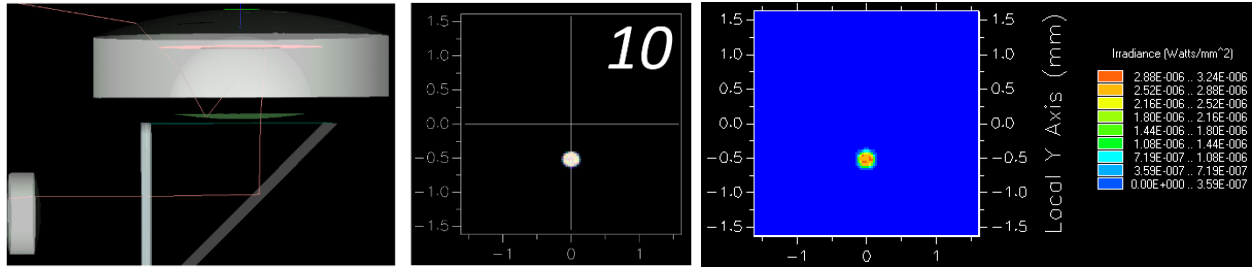


Figure 5.41. Ghost #10. (left) 3D Layout of ghost path, which originates from reflections off Prism R1 and L1R2, (middle) color image plot, (right) irradiance spread

These ten ghosts have the highest irradiance out of all the ghosts which were seen between the 30-degree field and 80-degree field heights. Through this analysis, the author now understands which surfaces contribute each of the brightest ghosts in the final image; Fig. 5.42 shows a 2D layout of the folded fisheye lens with notes on which surfaces contribute to each ghost. This shows that there are only five optical surfaces which do not contribute to the ghosts with high irradiance.

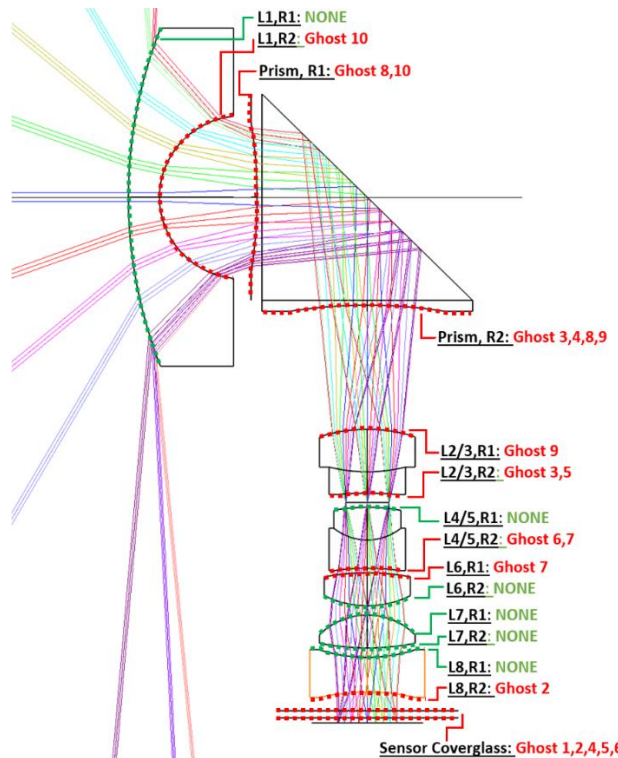


Figure 5.42. 2D Layout of the Folded Fisheye Lens design with notes on which surfaces contribute to the ghosts with highest irradiance.

Due to the complications of ensuring equal ray density in the image across all fields when dealing with pupil aberration, the irradiance of the full image is normalized to 1, and the irradiance of each ghost is then reported after that normalization. The irradiance of ghosts 1 through 10 are listed in Table 5.3, along with the 1st and 2nd reflection surfaces which contribute to the ghost. In this table, the sensor cover glass is referred to as ‘SCG.’

Ghost Path Number	Relative Irradiance to Source Image [W/mm²]	1st Reflection Surface		2nd Reflection Surface	
1 (30deg field)	2.10E-05	24	SCG	23	SCG
1 (80deg field)	1.93E-05	24	SCG	23	SCG
2 (30deg field)	3.04E-07	23 & 24	SCG	22	L8R2
2 (80deg field)	2.99E-07	23 & 24	SCG	22	L8R2
3	2.34E-08	12	L3R2	9	PrismR2
4	6.03E-07	23 & 24	SCG	9	PrismR2
5	1.75E-06	23 & 24	SCG	13	L3R2
6	1.48E-07	23 & 24	SCG	16	L5R2
7	3.68E-07	17	L6R1	16	L5R2
8	7.72E-07	9	PrismR2	3	PrismR1
9	2.72E-07	11	L2R1	9	PrismR2
10	1.79E-07	3	PrismR1	2	L1R2

Table 5.3. Summary of Ghost irradiance and contributing surfaces for the top 10 brightest

ghosts in the folded fisheye lens before the UV/IR-cut filter is placed in the system

5.5 Selecting UV/IR-cut Surface

In Chapter 5.2, the author chose to assume a 5% reflectance for the UV/IR-cut coating; by analyzing the ghost performance at various potential UV/IR-cut filter locations, the optimal location of this coating is chosen in this chapter.

Most coating specifications assume that the multilayer filters will be coated uniformly on a flat piece of glass, where the incident angle of the incoming light is zero; however, in practice, these coatings may be placed on curved surfaces where the incident angle of incoming rays are not zero. As the incident angle of the incoming light to the filter increases, the transmission range of a broadband pass filter will shift towards the shorter wavelengths [27] which is sometimes referred to as a blue shift [Fig. 5.43]. In the case of an imaging lens system where a UV/IR-cut filter is placed on a curved lens element, this blue shift can cause the filter to allow in more of the blue and UV wavelengths that would otherwise be assumed to be cut out, resulting in more chromatic aberration and blur in the final image; in addition, the IR-cut filter may shift into the visible part of the spectrum and cut out desired wavelengths. Because of this, it is important to place the UV/IR-cut filter onto a lens surface where the incident angle of the incoming rays are minimal.

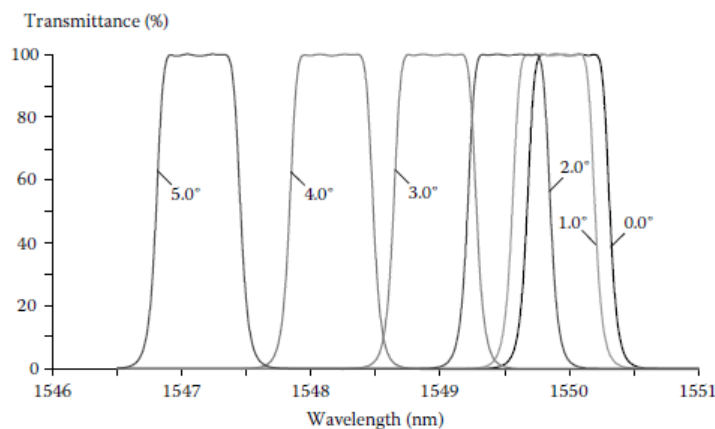


Figure 5.43. Example of a broadband-pass filter's transmission range shifting towards shorter wavelengths as the incident angle on the multilayer filter increases [27]

5.5.1 Contributing surfaces

While trying to determine an ideal UV/IR-cut filter location, the author has tried to find surfaces which have low ray incident angles while also not contributing to any of the primary ghost images. Looking at a 2D layout of the folded fisheye lens along with notes on which surfaces contribute to specific ghosts [Fig 5.44], the author has determined that there are only five practical surfaces to choose from. The available surfaces include lens 4/5 surface 1, lens 6 surface 2, lens 7 surfaces 1 and 2, and lens 8 surface 1. The incident angles on the first surface of the first lens are far too high for the coating to be placed on that surface; in addition, the incident angles on the first surface of lens 7 and the first surface of lens 8 appear much more extreme than the incident angles on lens 4/5 surface 1, lens 6 surface 2, or lens 7 surface 2. Because of this, the author has only evaluated the potential ghost performance when the UV/IR-cut filter is placed on lens 4/5 surface 1, lens 6 surface 2, and lens 7 surface 2.

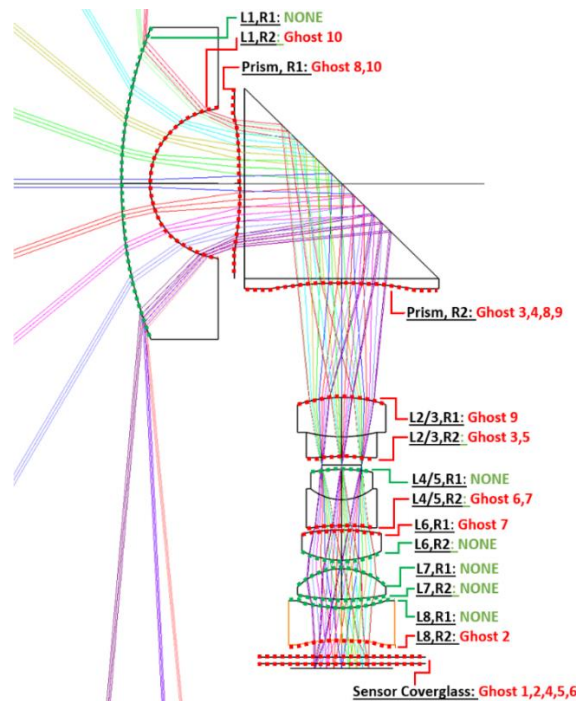


Figure 5.44. 2D Layout of the Folded Fisheye Lens design with notes on which surfaces contribute to the ghosts with highest irradiance.

5.5.2 Ghost comparison between UV/IR-cut located on surfaces L7R2, L4R1, and L6R2

It is expected that replacing the 0.4% reflectance antireflection coating with a 5% reflectance UV/IR-cut filter coating on any of the potential lens element surfaces will increase the irradiance of the ghosts which interact with that surface. Through this analysis, the author will analyze the color image plots of three potential UV/IR-cut locations and choose to place the UV/IR-cut on the surface which results in the ghosts with the lowest irradiance.

The first system was evaluated by replacing the 0.4% reflectance AR-coating on lens 7 surface 2 with a coating which has 5% reflectance. The system was sampled across three fields at 30 degrees, 60 degrees, and 95 degrees half fields of view [Fig. 5.46]. In comparison to the original system with no UV/IR-cut coating in the system [Fig. 5.45], it is apparent that the increased coating reflectance on lens 7 surface 2 creates many new ghosts with high irradiance. As seen in the 95 degrees field color image plot, a bright circular ghost has been introduced just below the image of the sun, in addition to a football shaped ghost in the center of the image and a handful of bright ghost images at the bottom of the image.

To evaluate the second system, the reflectance lens 4 surface 1 is replaced with the 5% reflectance UV/IR-cut coating filter and the ghost performance is evaluated [Fig. 5.47]. In the 60 degrees field and 95 degrees field color image plots, there has been the addition of ghosts with high irradiance near the bottom of the image, in addition to brighter ghosts around the source in the 0 degrees field image. Lastly, the third case is tested with the UV/IR-cut coating placed on lens 6 surface 2, and color image plots are obtained [Fig. 5.48]. When the filter is placed on this surface, there appears to be one large ghost which is introduced towards the bottom of the image for the 60 degrees and 95-degree color image plots and a higher level of background noise compared to the original system with no UV/IR-cut.

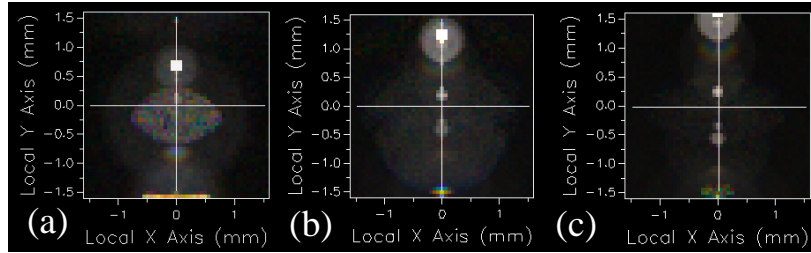


Figure 5.45. Ghost Images with no UV/IR-cut placed in the imaging system for (a) 30 degrees field, (b) 60 degrees field, and (c) 95 degrees field.

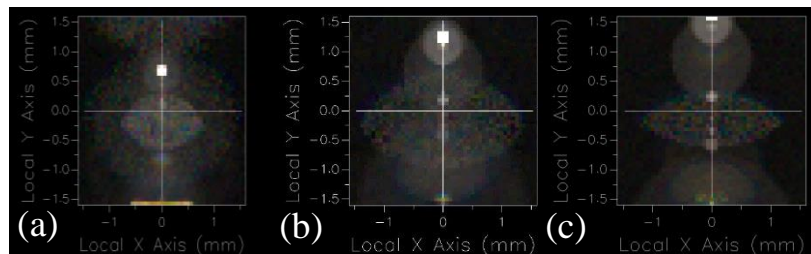


Figure 5.46. Ghost Images for UV/IR-cut placed on L7R2 for (a) 30 degrees field, (b) 60 degrees field, and (c) 95 degrees field.

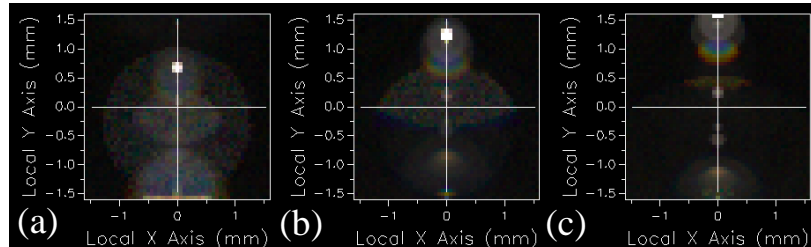


Figure 5.47. Ghost Images for UV/IR-cut placed on L4R1 for (a) 30 degrees field, (b) 60 degrees field, and (c) 95 degrees field.

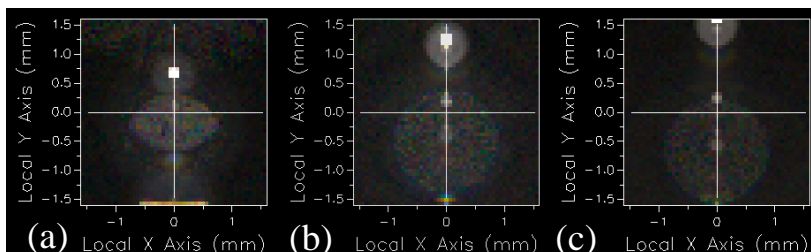


Figure 5.48. Ghost Images for UV/IR-cut placed on L6R2 for (a) 30 degrees field, (b) 60 degrees field, and (c) 95 degrees field.

Placing the UV/IR-cut coating on L6R2 introduces the fewest additional ghosts compared to when there is no UV/IR-cut in the system out of all three options. To mitigate the potential for bright ghost images at the stitch line (near the edge of the field of view on the opposite side of the source), the author has chosen to place the UV/IR-cut on lens 6 surface 2 for the folded fisheye lens design.

With this UV/IR-cut location, there are only two additional ghosts which are introduced by the higher reflectance on L6R2. The first ghost, which the author has named UV/IR ghost #1, appears as a large ghost at the top of the image at low field heights [Fig. 5.49] and has very low irradiance of $2.26 \cdot 10^{-7} \frac{W}{mm^2}$ in relation to the sun. The second ghost, UV/IR ghost #2, appears as a large circular ghost which stays near the bottom of the image larger field heights [Fig. 5.50]. This ghost also has a low irradiance of $8.35 \cdot 10^{-8} \frac{W}{mm^2}$ in relation to the sun.

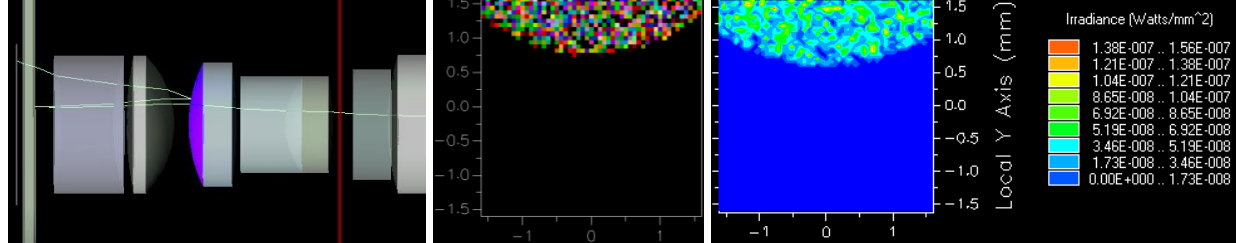


Figure 5.49. Ghost UV/IR #1. (left) 3D Layout of ghost path, which originates from the sensor cover glass and L6R2, (middle) color image plot, (right) irradiance spread

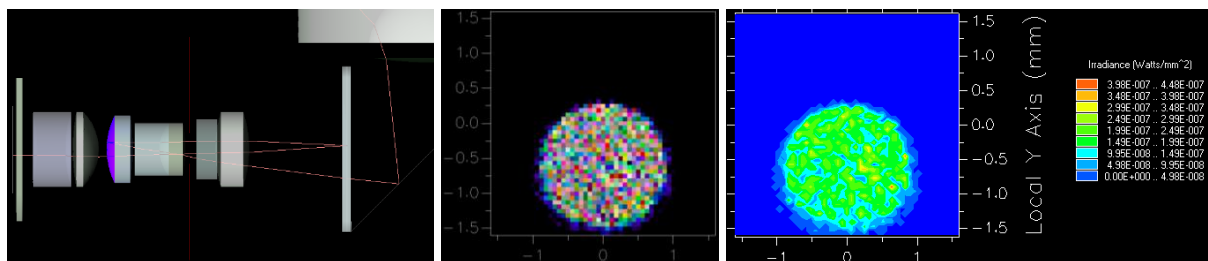


Figure 5.50. Ghost UV/IR #2. (left) 3D Layout of ghost path, which originates from L6R2 and Prism R2, (middle) color image plot, (right) irradiance spread

5.5 Final Ghost Performance of Folded Fisheye Lens

Through this ghost and stray light analysis in FRED, the author was able to determine which surfaces contribute to each ghost in the final image and the location of the 5% reflectance UV/IR-cut filter was optimized by placing it on the surface which introduced ghosts with the lowest irradiance. The author found that placing the coating on surface L6R2 resulted in the lowest irradiance and least distracting looking ghosts; thus, the UV/IR-cut filter has been chosen to be placed on this element [Fig. 5.51].

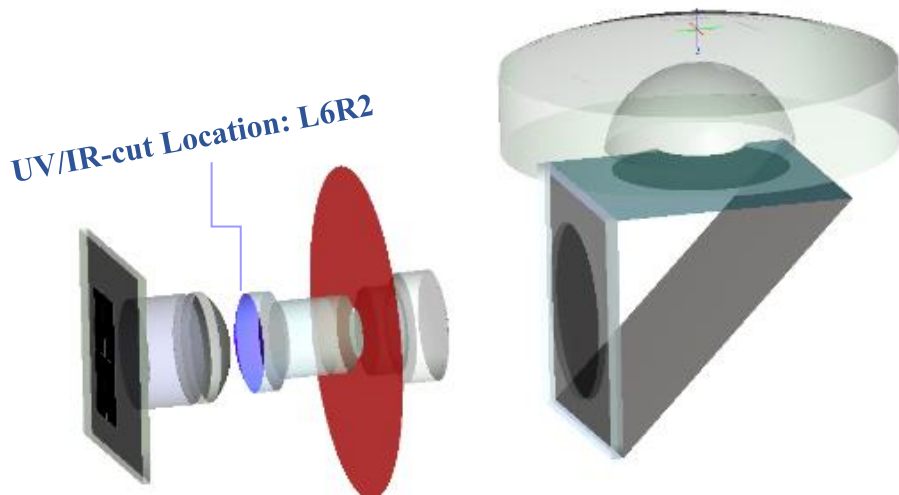


Figure 5.51. Demonstrating UV/IR-cut location on L6R2 in 3D view of folded fisheye lens

The ghosts seen with the UV/IR-cut on L6R2 are similar to the ghosts that were seen before the UV/IR-cut was added [Fig. 5.28], with only two new ghosts introduced which have relatively low-irradiance [Fig. 5.53]. After placing a 5% reflectance coating on the second surface of lens six, color image plots of the ghosts in the folded fisheye lens are presented from 0-degree to 100-degree field heights [Fig. 5.52]. A table illustrating the irradiance and contributing surfaces for ghosts 1 through 10 in addition to the two new ghosts, UV/IR #1 and UV/IR #2, is shown in Table 5.4 Out of the 12 ghosts which have been analyzed, UV/IR #1 has the 8th lowest irradiance ghost image, and UV/IR #2 has the 11th lowest irradiance ghost image.

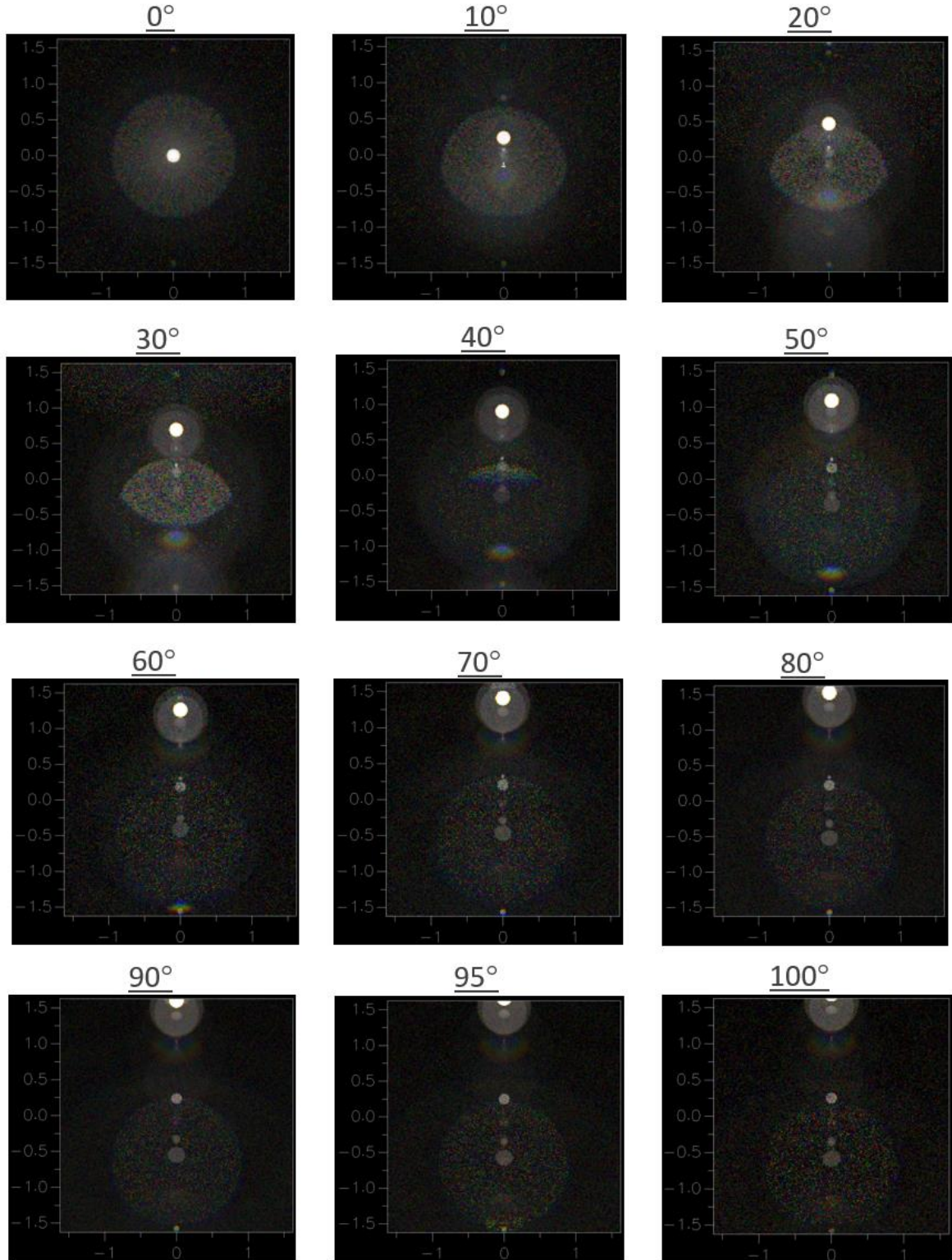


Figure 5.52. Ghost image color image plots for the folded fisheye lens with the highly reflective UV/IR-cut filter placed on lens 6 surface 2.

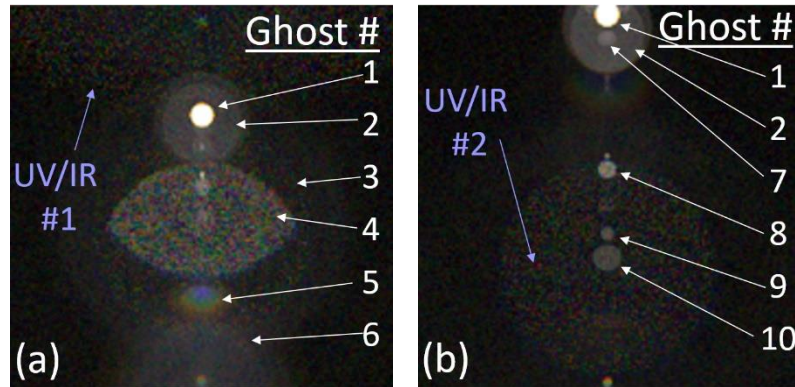


Figure 5.53. Ghost image color plots for (a) 30-degree field and (b) 80-degree field

<u>Ghost Path Number</u>	<u>Relative Irradiance to Source Image [W/mm^2]</u>	<u>1st Reflection Surface</u>		<u>2nd Reflection Surface</u>	
1	2.10E-05	24	SCG	23	SCG
2	3.04E-07	23 & 24	SCG	22	L8R2
3	2.34E-08	12	L3R2	9	PrismR2
4	6.03E-07	23 & 24	SCG	9	PrismR2
5	1.75E-06	23 & 24	SCG	13	L3R2
6	1.48E-07	23 & 24	SCG	16	L5R2
7	3.68E-07	17	L6R1	16	L5R2
8	7.72E-07	9	PrismR2	3	PrismR1
9	2.72E-07	11	L2R1	9	PrismR2
10	1.79E-07	3	PrismR1	2	L1R2
UV/IR #1	2.26E-07	23 & 24	SCG	18	L6R2
UV/IR #2	8.35E-08	18	L6R2	9	PrismR2

Table 5.4. Summary of ghost irradiance and contributing surfaces for the top 12 brightest ghosts when the UV/IR-cut filter is placed on L6R2 in the folded fisheye lens

To conclude, the author has superimposed the ghost images onto the circular fisheye lens image from Fig. 2.13; to obtain these images, the ghost images were overlaid on top of the circular fisheye image, and the ghost images were set to be 75% opaque via an additive process. Thus, if a pixel in the ghost image shows up as black, it simply adds 0 to the intensity of the circular fisheye lens image in that location, as opposed to removing intensity in that region if standard opaque processes. The ghost image is set to translate across the diagonal of the image, where it coincides with the real ghost image seen in the circular fisheye lens in Fig. 5.54 (d). While these images are a rough approximation, it provides a reference for what the ghosts may look like in a real camera use-case scenario. As expected, the ghosts with higher irradiance appear brighter in the final images.

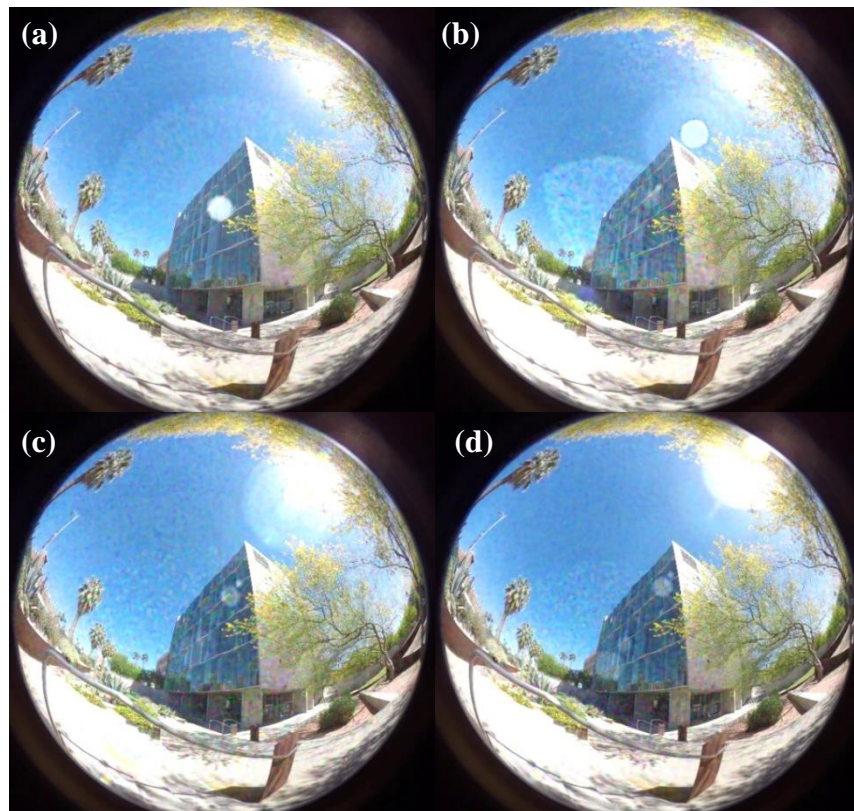


Figure 5.54. Ghost image plots superimposed on a real circular fisheye image. (a) 0-degree field (b) 30-degree field, (c) 60-degree field, (d) 90-degree field

6 CONCLUSION

In this thesis, the author has designed and analyzed a new folded fisheye lens which is intended to be used in a compact virtual reality camera. The compact fisheye lens has a focal length of 1.297mm with a maximum aperture of F/2.8 with the ability to capture a 190-degree full field of view in the 1/2.7" ON-Semiconductor CMOS image sensor which the lens is designed to be paired with. Eight spherical glass optical elements are used in conjunction with a molded glass prism which has powered entrance and exit faces to accomplish very high image quality and MTF performance across the entire field of view in a compact form factor. The optical design which is presented has been designed for manufacturing as it is intended to be used in a consumer electronics device which drive optical designs to be high performing and cheap while being manufactured in very large quantities. The design structure is simple and achieves very high manufacturing yield with common fabrication tolerances.

The two-lens system intended to be used as the imaging module in a virtual reality camera fits in a 25 x 56mm package and can reconstruct a photosphere of all objects which lie outside of a 270mm diameter sphere centered about the lenses; Most current consumer-focused virtual reality cameras which are on the market are significantly larger than the system which has been designed in this thesis report, giving the two-lens folded fisheye module a competitive advantage. The stray light performance of the whole system has been optimized by placing the highly reflective UV/IR-cut filter coatings on a surface which contributes to the lowest irradiance ghost images.

Along with the design and analysis of the folded fisheye lens, the author has provided an extensive background of fisheye lens history and their unique properties with hopes of this master's thesis report acting as a reliable resource on the topic of fisheye lens design. Fisheye lenses have been used for over a century for both photographic and scientific purposes, beginning

with R. W. Wood's water tank style fisheye lens device in 1906; Since then, fisheye lens development has continued to drive these fascinating imaging lenses to have increased speed and resolution while maintaining a compact form factor, which provides many unique challenges to an optical designer.

REFERENCES

- [1] R.W.Wood, "XXIII Fish-eye views, and vision under water," Philosophical Magazine Series 6, vol. 12, no. 68, pp. 159-162, 1906.
- [2] H. Robin, "A lens for whole sky photographs," Quarterly Journal of the Royal Meteorological Society, vol. 50, no. 211, pp. 227-235, 1924.
- [3] W.N.Bond, "A wide angle lens for cloud recording," Philosophical Magazine Series 6, vol. 44, no. 263, pp. 999-1001, 1922.
- [4] Yan, Y. (2016). Photographic Fisheye Lens Design for 35mm Format Cameras (master's thesis, University of Arizona, Tucson, Arizona). Retrieved from <http://arizona.openrepository.com/arizona/handle/10150/613395>.
- [5] GoPro, "Fusion Camera," GoPro.com, 01 April 2018, [Online]. Available: <https://shop.gopro.com/cameras/fusion/CHDHZ-103.html> .
- [6] GoPro, "Here is Odyssey," GoPro.com, 01 April 2018, [Online]. Available: <https://gopro.com/news/here-is-odyssey> .
- [7] R. Kingslake, A History of the Photographic Lens, Academic Press, 1989.
- [8] C. B. Martin, "Design issues of a hyperfield fisheye lens," in Novel Optical Systems Design and Optimization VII, Denver, CO, 2004.
- [9] German Patent 620,538.
- [10] K. Miyamoto, "Fish Eye Lens," Journal of the Optical Society of America, vol. 54, no. 8, pp. 1060-1061, 1964.
- [11] US Patent 3,524,697.
- [12] US Patent 8,456,751.

- [13] GoPro, “Hero6 Black,” GoPro.com, 01 April 2018, [Online].
Available: <https://shop.gopro.com/cameras/hero6-black/CHDHX-601-master.html>
- [14] Emerald Integrations, “Toyota Prius Backup Camera,” emeraldintegrations.com, 01 April 2018, [Online]. Available: <https://www.emeraldintegrations.com/car-safety/toyota-prius-oem-rear-view-backup-camera-system.html>
- [15] Ring, “Video Doorbells,” Ring.com, 01 April 2018, [Online]. Available: <https://ring.com/>
- [16] Garmin, “Garmin Virb,” Buy.Garmin.com, 01 April 2018, [Online].
Available: <https://buy.garmin.com/en-US/US/p/562010>
- [17] Google, “Google Street View,” Google.com, 01 April 2018, [Online].
Available: <https://www.google.com/streetview/understand/>
- [18] Facebook, “Surround 360,” Facebook360.fb.com, 01 April 2018, [Online].
Available: <https://facebook360.fb.com/facebook-surround-360/>
- [19] GoPro, “Omni,” GoPro.com, 01 April 2018, [Online].
Available: <https://shop.gopro.com/virtualreality/omni---rig-only/MHDHX-007.html>
- [20] Samsung, “Gear 360,” Samsung.com, 01 April 2018, [Online].
Available: <http://www.samsung.com/global/galaxy/gear-360/specs/>
- [21] Nikon, “Keymission 360,” Nikon.Keymission.com, 01 April 2018, [Online].
Available: <http://nikon.keymission.com/keymission360/#specifications>
- [22] Ricoh, “Theta V,” theta360.com, 01 April 2018, [Online].
Available: <https://theta360.com/en/about/theta/v.html>
- [23] ON-Semiconductor, “AR0237 Data Sheet,” OnSemi.com, 01 April 2018, [Online].
Available: [http://www.onsemi.com/PowerSolutions/product.do?id=AR0237>](http://www.onsemi.com/PowerSolutions/product.do?id=AR0237)

- [24] El-Maksoud, R. A. (2009). Ghost Image Analysis for Optical Systems (Doctoral dissertation, University of Arizona, Tucson, Arizona).
Retrieved from <http://arizona.openrepository.com/arizona/handle/10150/195492>.
- [25] H. Sun, Lens Design: A Practical Guide, CRC Press, 2017.
- [26] Edmund Optics, "AR-coating Properties," [edmundoptics.com](http://www.edmundoptics.com/resources/application-notes/optics/anti-reflection-coatings/), 01 April 2018, [Online].
Available: <https://www.edmundoptics.com/resources/application-notes/optics/anti-reflection-coatings/>
- [27] H. A. Macleod, Thin-Film Optical Filters, CRC Press, 2010.
- [28] Edmund Optics, "Long and Short Pass Filters," [edmundoptics.com](http://www.edmundoptics.com/optics/optical-filters/longpass-edge-filters), 01 April 2018, [Online].
Available: <https://www.edmundoptics.com/optics/optical-filters/longpass-edge-filters>
- [29] J. Sasian, Introduction to Aberrations in Optical Imaging Systems, Cambridge University Press, 2013.
- [30] Zemax, OpticStudio 16.2 SP2 Help Files, 2018.
- [31] J. J. Kumler and M. L. Bauer, "Fish-eye lens designs and their relative performance," in Current Developments in Lens Design and Optical Systems Engineering, San Diego, 2000.
- [32] J. Greivenkamp, Field Guide to Geometrical Optics, SPIE Press, 2004.
- [33] J. Bereau and P. P. Clark, "The Optics of Miniature Digital Camera Modules," in International Optical Design Conference 2006, Vancouver, 2006.
- [34] J. Bentley and C. Olson, Field Guide to Lens Design, SPIE Press, 2012.
- [35] G. Boreman, Modulation Transfer Function in Electro-Optical Systems, SPIE Press, 2013.
- [36] Edmund Optics, "Introduction to Modulation Transfer Function," [EdmundOptics.com](http://www.edmundoptics.com/resources/application-notes/optics/introduction-to-modulation-transfer-function/), 01 April 2018, [Online]. Available: <https://www.edmundoptics.com/resources/application-notes/optics/introduction-to-modulation-transfer-function/>

- [37] M. Laikin, "Wide angle lens systems," in 1980 International Lens Design Conference, 1980.
- [38] Trioptics, "MTF Pro Systems," Trioptics.com, 01 April 2018, [Online].
Available: <https://www.trioptics.com/products/mtf/pro/>
- [39] D. Reiley, "Folded Zoom Lenses – A Review of Patent Literature," in International Optical Design Conference 2014, 2014.
- [40] US Patent 7,023,628.
- [41] Ohara, "L-LAH86 Data Sheet," OharaCorp.com, 01 April 2018, [Online].
Available: <https://www.oharacorp.com/lows.html>
- [42] Ohara, "Low Softening Temperature Optical Glass," OharaCorp.com, 01 April 2018,
[Online]. Available: <https://www.oharacorp.com/lows.html>
- [43] Schott, "Mechanical and Thermal Properties of Optical Glass," Schott.com, 01 April 2018,
[Online]. Available: https://www.schott.com/d/advanced_optics/d08c2fb9-c2f2-4861-a57b-18495ef5a4fd/1.2/schott_tie-31_mechanical_and_thermal_properties_of_optical_eng.pdf
- [44] A. Symmons and M. Schaub, Field Guide to Molded Optics, SPIE Press, 2016.